Analytic theory of finite pulse effects involving spin-1 nucleus in rotating solids

Mohit Bansal

A thesis submitted for the partial fulfillment of
the degree of Doctor of Philosophy

Department of Chemical Sciences
Indian Institute of Science Education and Research Mohali
Knowledge city, Sector 81, SAS Nagar, Manauli PO, Mohali-140306, Punjab, India.

April 2024

Dedicated to my family

ਬੇਹਿੰਮਤੇ ਨੇ ਜਿਹੜੇ ਬਹਿ ਕੇ ਸ਼ਿਕਵਾ ਕਰਨ ਮੁਕੱਦਰਾਂ ਦਾ ,

ਉੱਗਣ ਵਾਲੇ ਉੱਗ ਪੈਂਦੇ ਨੇ ਪਾੜ ਕੇ ਸੀਨਾ ਪੱਥਰਾਂ ਦਾ |

Declaration

The work presented in this thesis entitled "**Analytic theory of finite pulse effects involving spin-1 nucleus in rotating solids**" has been carried out by me under the supervision of **Dr. Ramesh Ramachandran** in the Department of Chemical Sciences, Indian Institute of Science Education and Research (IISER) Mohali.

This work has not been submitted in part or in full for a degree, a diploma, or a fellowship to any other university or institute. Whenever contributions of others are involved, every effort is made to indicate this clearly, with due acknowledgement of collaborative research and discussions. This thesis is a bonafide record of original work done by me and all sources listed within have been detailed in the bibliography.

Date: **Mohit Bansal**

Place: Mohali (Candidate)

In my capacity as the supervisor of the candidate's thesis work, I certify that the above statements by the candidate are true to the best of my knowledge.

Date: **Dr. Ramesh Ramachandran**

Place: Mohali (Supervisor)

Contents

Acknowledgements

Many people have helped, motivated, inspired and supported me during my PhD journey. I am sincerely thankful to all of them.

First of all, I would like to express my sincere gratitude towards my guide, **Dr. Ramesh Ramachandran** for being helpful and cooperative. He is a good teacher and a passionate person from whom one can learn a lot of things. All the scientific and non-scientific discussions with him have helped me grow as a person as well as researcher and these discussions will always be memories to cherish on.

I am thankful to my doctoral committee members, **Prof. Sanjay Mandal** and **Dr. Shamasundar** for monitoring my progress at regular intervals and giving me their valuable feedbacks which helped me improve in my presentation skills.

IISER Mohali administration is duly acknowledged for providing the graduate assistantship, all the necessary facilities and infrastructure to carry out this research. **IISER Mohali Library** is duly acknowledged for providing the reference books and access to peer reviewed journals.

Next, I would like to thank all my lab members for providing a healthy working environment in the lab. I am thankful to **Dr. Vinay Ganapathy**, **Dr. Rajat Garg**, **Shreyan Ganguly, Kuntal Mukherjee, Nisha Bamola** and **Soumyadev Das**. They really helped me a lot during my stay in the lab. I want to thank you all for all the discussions during presentations as well as on board talks, reading the proof of articles and all those parties.

In every walk of life, a set of good friends is very essential. I would like to express my deepest gratitude to my friends who have been unwavering pillars of support during my Ph.D. journey. A special mention to **Mohit Sharma, Sumit Bansal, Prabhjot Singh, Snehal Waghmare, Priyanka Babbar, Dr. Anuj Gupta, Dr. Surinder Kaur, Mrs. Gagandeep Kaur, Arun Goyal** and my childhood friends from school **Vishal Arora and Karan Tanwar**. Their encouragement, understanding and companionship have been invaluable throughout this endeavour. I am grateful to my relatives **Mr. Rajeev Mittal**

and Mrs. Sarita Mittal, Mohit Garg, Rohit Garg and Karan Garg for their love and support through this journey. I am fortunate enough to find a set of good colleagues in IISER campus, **Aman Gupta, Vandana Sharma, Gaurav Kumar Bhati, Budha Ratnav, Dr. Prateek Ahuja, Dr. Akshi and Anshika**. There is a big list of persons from my batch, my seniors and juniors who have shared in both the triumphs and struggles of this journey. I am thankful to all of them.

I would like to dedicate this thesis to my parents, **Mrs. Madhu Bansal** and **Mr. Jagdeep Bansal**, whose unwavering support, love and encouragement have been the driving force behind my academic pursuits. Your sacrifices, both seen and unseen, have laid the foundation for my success. Your values, guidance and unconditional love have shaped not only my academic pursuits but also the person I am today. I would also like to express my heartfelt gratitude to my sibling **Jyoti** who has been a source of strength and motivation throughout my Ph.D. journey. Her patience, empathy and support doing all the household things alone (that was supposed to be done by me), share in both the joys and challenges have made this achievement possible.

Above all, I thank the **Almighty** for making this happen and including the chapter of Doctoral studies in my life.

List of Publications

The work in this thesis is, in part, based on the following publications.

- **Chapter 2.** Reproduced from [Theory of finite pulse effects beyond perturbation limit: Challenges and Perspectives, **Mohit Bansal** and Ramesh Ramachandran, ***J. Magn. Reson. Open***, 2022, **10**, 100042], with permission from ELSEVIER.
- **Chapter 2.** Reproduced from [Theory of radio-frequency pulses on periodically driven three-level systems: challenges and perspectives, **Mohit Bansal** and Ramesh Ramachandran, ***Phys. Chem. Chem. Phys.***, 2022, **24**, 29092], with permission from the PCCP Owner Societies.
- **Chapter 3.** Reproduced from [Quantifying quadrupole effects in NMR spectra of spin-1/2 nuclei in rotating solids, Nisha Bamola, **Mohit Bansal** and Ramesh Ramachandran, ***Phys. Chem. Chem. Phys.***, 2023, **25**, 17877], with permission from the PCCP Owner Societies.

List of Figures

List of Tables

Abstract

Understanding the response of nuclear spins subjected to oscillating fields has remained an active pursuit in methodology development in NMR spectroscopy. While methods to study the dynamics of spin-1/2 nuclei exist, such studies involving quadrupolar spins (spins with I>1/2) have always been fraught with difficulty. In particular, the evolution of nuclear spins subjected to radio-frequency (RF) pulses in periodically driven multi-level systems has remained a challenging problem owing to the domineering presence of the quadrupolar interactions. Although, development of analytic methods in static solids have enhanced our basic understanding of the experiments, straightforward extensions to rotating solids remain less trivial. In particular, a uniform analytic framework that explicates the interplay between the sample spinning frequency, amplitude of the RF pulse and the quadrupolar coupling constant remains an open problem in rotating solids. Consequently, optimizations based on numerical methods have gained prominence in the development of NMR methods in quadrupolar nuclei. While investigations based on numerical methods are easier to implement and provide results, they do not necessarily afford insights into the physical phenomena under study. As an alternative, analytic methods based on Floquet theory are explored in the thesis for studying the excitation process in multilevel systems. Specifically, effective time-propagators derived from analytic methods are proposed to describe the effects of RF pulses in rotating solids in three-level (S=1) systems. Through comparisons with simulations emerging from exact numerical methods, the suitability and exactness of the analytic methods is examined over wide-range of experimental parameters. Additionally, the interference effects observed in spin-1/2 nuclei coupled to quadrupolar spins (say S=1) are also discussed.

Chapter 1

Introduction

1.1 Background

Determination of molecular structure at atomic resolution through spectroscopic methods has remained an active pursuit for understanding both the functioning of materials (of both chemical and biological relevance) as well as their role in the dynamics of chemical/biological reactions. While characterization techniques such as X-ray diffraction, neutron scattering and vibrational spectroscopy etc. have been quite successful in addressing several important problems, the emergence of solid-state NMR (ssNMR) as a structural tool has been quite promising in the last two to three decades. In contrast to analytic techniques that are limited by molecular weights, nature of the sample etc., ssNMR has emerged as a unique, reliable tool for characterizing variety of systems, ranging from membrane proteins and amyloid fibrils in biochemistry to polymers, battery materials, photovoltaic pervoskites, semiconductors, glasses and catalysts [1–7]. In contrast to other spectroscopic methods, the manipulation of the nuclear spin interactions at the atomic level enhances the repertoire of NMR spectroscopy as a versatile tool for providing variety of structural constraints such as torsion angles, interatomic distances etc. both in the solution as well as in the solid-state. While studying the effects of magnetic fields and radio-frequency pulses (RF) on nuclear spins (spin interactions) have remained central in NMR spectroscopy, the orientation dependence of the spin interactions in the solid-state makes it unique and important in contrast to similar studies in the solution state.

From an operational aspect, the genesis of solid-state NMR spectroscopy began only in 1958 through the discovery of Magic Angle Spinning (MAS) experiment [8,9]. In contrast to solution NMR spectroscopy, the spin interactions in the solid state remain anisotropic due to

restricted mobility, resulting in broadened spectra. To overcome the undesirable broadening effects, Andrew et al. and Lowe, independently demonstrated the idea of physical rotation of the sample along an axis inclined at an angle θ_m=54.7° with respect to the static magnetic field. Such an approach resulted in spectra comprising a centre band (often determined by the isotropic part of the spin interactions) and series of spinning sidebands (due to the anisotropic part of the spin interaction) distributed symmetrically about the center-band at integer multiples of the spinning frequency [2,10]. With increase in the spinning frequency, the anisotropic part of the interactions get partially/completely averaged out resulting in isotropic liquid like spectrum. In particular, spin interactions in spin-1/2 nuclei such as chemical shift anisotropy (CSA), dipole-dipole interaction and indirect spin-spin interaction (J-coupling) have magnitudes ranging from Hz to few kHz and are mostly or partially averaged out under MAS resulting in well-resolved spectra in the solid state. In combination with MAS, development of techniques such as cross-polarization [11,12], homonuclear and heteronuclear decoupling methods [13–15], homonuclear recoupling [16–20] and heteronuclear recoupling methods [21–23] have facilitated structure determination of materials containing spin-1/2 nuclei in the solid state.

While these advancements have largely benefited the study of spin I=1/2 nuclei (e.g. ^{1}H, ^{13}C, ^{31}P etc.), the improvements seem only marginal in the experimental studies of quadrupolar nuclei (nuclei with I>1/2). Since more than 70% of nuclei in the periodic table are quadrupolar (I>1/2), the NMR study of such nuclei become essential. According to nuclear shell model, nuclear spins with I>1/2 (quadrupolar nuclei) have non-spherical distribution of charge around the nucleus. This charge distribution interacts with the surrounding electric field gradient resulting in the "Quadrupolar interaction" [5,24,25] and is characterized in terms of the quadrupolar coupling constant (C_Q). In contrast to other internal interactions, the quadrupolar interaction is magnitude wise very strong (C_Q is of the order of several MHz) and is primarily responsible for the line broadening observed in the NMR spectra of quadrupolar nuclei. Consequently, the effects of spinning have only been marginal in the experimental studies of quadrupolar nuclei (I>1/2) [26,27].

To this end, alternative strategies such as Variable Angle Spinning (VAS) [28,29], Dynamic angle spinning (DAS) [30] and Double rotation (DOR) [31,32] techniques were introduced to improve the resolution of the NMR spectra of quadrupolar nuclei in the solid state. Due to technical limitations and the degree of sophistication required, such techniques could never be integrated with routinely available NMR hardware. In 1995, Frydman and co-workers [33,34]

proposed the Multi-Quantum MAS experiment (MQMAS) for acquiring isotropic spectra of quadrupolar nuclei with the use of traditional NMR hardware without special modifications. The MQMAS technique is a two-dimensional experiment that provides correlation between second-order quadrupolar shifted isotropic chemical shifts in the indirect dimension and has been used to measure chemical and second-order isotropic shifts in a wide range of quadrupolar nuclei [35–40]. The local structural information contained in the electric field gradients (EFG's) of the individual sites is deduced from the resolution obtained in MQ dimension. Although, such an approach seems very viable, the poor excitation efficiency of MQ coherences and its reconversion to detectable SQ coherence seems to be the major limiting factor. To this end, several variants of MQMAS [41–45] and sensitivity enhancement techniques such as fast amplitude-modulated pulses [46–50], double-frequency sweeps [51–53], rotational resonance effects [54–59], CPMG pulse train [60–62] etc. have been developed in the past two decades. Since structural parameters such as electronic arrangement, distance between nuclei, torsion angle are manifested in the anisotropic internal interactions such as chemical shift anisotropy, dipolar interactions, quadrupolar interactions etc., suites of recoupling experiments analogous to those in spin I=1/2 systems have also been developed in systems comprising quadrupolar spins. To this end, several heteronuclear dipolar recoupling experiments [63–68] have emerged to re-introduce dipolar interaction in systems containing quadrupolar nuclei. In particular, MQMAS experiments have been integrated with cross-polarization techniques to enhance polarization on quadrupolar nuclei [69–75]. Additionally, CSA tensors of spin-1/2 system (such as ^{1}H) coupled with quadrupolar nuclei have been extracted through multidimensional experiments [76–83].

Although, the availability of sophisticated hardware such as high magnetic field strengths, ultrafast MAS probes have benefited studies involving quadrupolar spins, quantifying experiments involving quadrupolar nuclei have always been fraught with difficulty owing to the domineering presence of the quadrupolar interactions. Consequently, simulations of NMR experiments based on numerical methods [84,85] have become indispensable in the solid state. Employing numerical simulations, optimal parameters for a given experiment are deduced by trial and error, resulting in the development of sophisticated experiments both in the solution and solid state. Nevertheless, understanding the nuances of the underlying spin physics is quintessential to the design of new pulse sequences besides extending the range of applications of NMR spectroscopy. Since extraction of molecular constraints in NMR experiments involves iterative fitting of the experimental data, simple analytic expressions that are

computationally efficient are essential.

1.2 Objectives and scope of the thesis

From an operational point of view, the main complexity in analytic treatments arises during the description of the evolution of spins under an RF pulse. In the description of spin I=1/2 systems, the amplitude of the RF pulse often exceeds the magnitude of the internal spin interactions. Hence, the time-evolution of the spin system during an RF pulse is approximately governed by the RF interaction and is conveniently described through rotation operators. By contrast, in the case of quadrupolar spins, the magnitude of the quadrupolar interaction (described in terms of the quadrupolar coupling constant) often exceeds both (i) the available RF amplitude (ii) internal spin interactions. Consequently, during an RF pulse, the quadrupolar nucleus evolves under both the RF and the quadrupolar interaction Hamiltonians. Although, theoretical formulations employing descriptions in the state space built on "adiabatic approximations" have emerged in the past for describing the underlying spin dynamics, their utility has always remained limited to static samples with minor extensions in rotating samples [65,86–89]. In particular, their utility in describing the spin dynamics in powder spinning samples is limited due to the orientational dependence of the quadrupolar interactions. In such systems, the magnitude of the quadrupolar coupling constant varies with individual crystallite orientations and the state-space descriptions become less insightful.

Although, analytic methods based on Average Hamiltonian Theory (AHT) and Floquet theory have been used extensively in the literature [10,90–98] to describe the underlying spin dynamics in spin I=1/2 systems, the exactness and utility of these methods in the description of MAS experiments involving quadrupolar spins remains less explored. This forms the main motivation behind this thesis. Employing the density operator formalism [99] and the time-propagators derived from the analytic methods, the spin dynamics involving quadrupolar spins is studied. Below, we outline the problems addressed in this thesis:

1. To begin with, analytic theory of finite pulse effects in rotating solids is described in spin I=1/2 systems employing the density operator formalism. Employing this model system, the role of interaction frames is discussed. Employing time-propagators derived from AHT and Floquet methods, the excitation of double-quantum (DQ) transitions in spin-1 system is discussed employing the density operator formalism. The interplay between the RF amplitude, quadrupolar coupling constant and the spinning frequency in the convergence of the

expansion coefficients in the time-propagators is discussed through analytic expressions.
2. In the second part of the thesis, the interference effects in coupled systems emanating from RF irradiation on the quadrupolar spin is discussed. For demonstrative purposes, examples from experiments that involve simultaneous recoupling and decoupling of spin interactions is examined in coupled systems comprising spin-1 system.

In what follows, the basic theory and methodology required for describing the underlying spin dynamics in NMR experiments is summarised for the sake of continuity.

1.3 Theory and Methodology

1.3.1 Spin interactions in NMR

Unlike other spectroscopic methods, NMR spectroscopy provides a unique platform for manipulating the nuclear spin interactions at the atomic level without destroying the information content inherent in them. To explicate the role of various spin interactions in NMR experiments, the spin Hamiltonian is expressed as a sum comprising the external and internal interactions. The external Hamiltonian comprises the interaction between the nuclear spin magnetic moment and the magnetic fields (inclusive of both static and oscillating magnetic fields). The internal interactions comprise the nuclear spin interactions with the chemical shift interaction, scalar interaction, dipolar and quadrupolar interactions being the prominent ones.

(A) External interactions

The Zeeman interaction represents the interaction between the nuclear spin magnetic moment and the static magnetic field and is represented through the Zeeman Hamiltonian, H_Z.

$$H_Z = -\mu_z B_0 = -\gamma B_0 I_z = \omega_0 I_z \; ; \; \hbar = 1 \tag{1.1}$$

where μ is the magnetic moment, γ is the gyromagnetic ratio (in units of rad/sec/T), B_0 is the strength of the static magnetic field (in units of Tesla, T) and $\frac{\omega_0}{2\pi}$ is the Larmor frequency (of MHz order). In a similar vein, the interaction of the nuclear spin with the oscillating magnetic field (applied along the x-direction) is represented through the RF Hamiltonian given below,

$$H_{RF}\left(t\right) = -2\gamma B_1 \cos\left(\omega_{ref} t + \phi\right) I_x = 2\omega_1 \cos\left(\omega_{ref} t + \phi\right) I_x \tag{1.2}$$

where $\omega_1 = -\gamma B_1$ is the nutation frequency of the RF field and ϕ is the phase. In comparison to the internal interactions (barring the quadrupolar interaction in some cases) present in

the system, the Zeeman interaction is dominant. Since the evolution of the system under the internal spin interactions in the presence of oscillating fields (usually employed to probe the spin system) is desired, theoretical description of NMR experiments is often carried out in the rotating frame, wherein the dominant contributions from Zeeman interactions is absent. Accordingly, the time-dependent contributions of the spin interactions in the rotating frame are ignored under "Secular Approximation", [1–3] while, the RF Hamiltonian (Eq. 1.2) reduces to a much simpler form given below.

$$\widetilde{H}_{RF} = \omega_1 I_x \tag{1.3}$$

(B) Internal interactions

In contrast to liquids, the spin interactions in the solid state are represented through 'tensors', a mathematical quantity that transforms in certain prescribed ways. The anisotropic nature of the spin interactions in the solid-state (such as chemical shift, dipolar, scalar interactions and quadrupolar interactions) are represented through second rank tensors. A detailed description of these interactions is well-documented in the literature [25, 100–103] and is consciously omitted to avoid repetition. Below, we present a brief summary of the important equations that would be required to follow the thesis.

Due to physical rotation of the sample, the internal spin interactions become time-dependent in MAS experiments [8, 9, 100, 101]. Here in this thesis, we restrict ourselves to three internal interactions namely chemical shift interaction, quadrupolar interaction (present in I>1/2 system) and dipolar interactions.

(i) Chemical shift interaction

The chemical shift interaction depicts the interaction between the nuclear spin magnetic moment with static magnetic field mediated through surrounding electronic cloud. In case of solids, the chemical shift interaction is characterized by both the isotropic as well as the anisotropic part chemical shift anisotropy (CSA). The isotropic chemical shifts provide the electronic and co-ordination environment of nuclei, while the chemical shift anisotropy provides insights into orientation and conformation. In the rotating frame, the chemical shift interaction under MAS is represented by the following equation,

$$H_{CS}(t) = \underbrace{\Delta\omega I_z}_{H_{iso}} + \underbrace{\sum_{m=-2,\neq 0}^{2} \omega_I^{(m)} e^{im\omega_r t} I_z}_{H_{CSA}(t)} \tag{1.4}$$

where $\Delta\omega = \omega_0 - \omega$ represents the offset or isotropic chemical shift.

In MAS experiments, the anisotropic components of the internal interactions (CSA, dipolar

and quadrupolar interaction) are represented through the following standard expression.

$$\omega_{\lambda}^{(m)} = \sum_{m_1=-2}^{2} R_{P,\lambda}^{(2)m_1} \sum_{m_2=-2}^{2} D_{m_1 m_2}\left(\Omega_{PM}\right) D_{m_2 m}\left(\Omega_{MR}\right) d_{m0}\left(\beta_{RL}\right) \tag{1.5}$$

Here, $R_{P,\lambda}^{(2)m_1}$ represents the component of the spatial tensor (λ= CSA, dipolar or quadrupolar interaction) defined in the principal axis system (PAS), while $D_{m_1 m_2}\left(\Omega_{AB}\right)$ denotes the Wigner Rotation matrix with rank 2 and $\Omega_{AB} = \{\alpha, \beta, \gamma\}$, the set of Euler angles used in the transformation from PAS to Lab frame [102,103]. In the PAS, the spatial components ($R_{P,\lambda}^{(2)m_1}$) associated with the CSA interactions are represented below.

$$R_{P,CSA}^{(2)0} = \delta_{aniso}\ ,\ R_{P,CSA}^{(2)\pm 2} = -\frac{1}{\sqrt{6}}\delta_{aniso}\eta\ ,\ R_{P,CSA}^{(2)\pm 1} = 0 \tag{1.6}$$

with δ_{aniso} representing the magnitude of the CSA and η, the asymmetry parameter.

(ii) Quadrupolar interaction

Nuclei with I>1/2 possess a non-zero quadrupole moment due to non-spherical charge distribution in the nucleus (according to nuclear shell model). This quadrupole moment interacts with electric field gradient generated by their surroundings resulting in quadrupolar interaction (H_Q) [5,25]. The magnitude of the quadrupolar interaction often exceeds the amplitude of the RF excitation pulse. Often the quadrupolar Hamiltonian is expressed as a product of irreducible tensor operators (comprising spatial tensor, $R^{(2)q}$ and spin tensor, $T^{(2)q}$ operators) [25,102,103].

$$H_Q\left(t\right) = \sum_{q=-2}^{2} R_{Q,L}^{(2)-q}\left(t\right) T^{(2)q} \tag{1.7}$$

where,

$$R_{P,Quad}^{(2)0} = \omega_Q\ ,\ R_{P,Quad}^{(2)\pm 1} = 0\ ,\ R_{P,Quad}^{(2)\pm 2} = -\frac{\omega_Q \eta}{\sqrt{6}} \quad \left(\omega_Q = 2\pi \frac{3C_Q}{2I\left(2I-1\right)}, C_Q = e^2 qQ\right)$$

$$T^{(2)0} = \frac{1}{\sqrt{6}}\left[3I_Z^2 - I^2\right]\ ,\ T^{(2)\pm 1} = \mp\frac{1}{2}\left[I_Z I_{\pm} + I_{\pm} I_Z\right]\ ,\ T^{(2)\pm 2} = \frac{1}{2}I_{\pm}^2$$

In the rotating frame, the quadrupolar interaction acquires additional time-dependence due to 'ω' and is expressed in the compact form as given below.

$$H_Q(t) = \frac{1}{\sqrt{6}} \sum_{q=-2}^{2} \sum_{m=-2,\neq 0}^{2} \omega_{Q,m}^{(2)-q} T^{(2)q} e^{iq\omega t} e^{im\omega_r t} \tag{1.8}$$

where

$$\omega_{Q,m}^{(2)q} = \sum_{m_1} R_{Q,PAS}^{(2)m_1} \sum_{m_2} D_{m_1 m_2}\left(\Omega_{PM}\right) D_{m_2 m}\left(\Omega_{MR}\right) d_{m,q}\left(\beta_{RL}\right)$$

To first-order, the quadrupolar Hamiltonian in the rotating frame is represented by ignoring the time-dependent terms (retaining terms that commute with Zeeman interaction only, $\left[I_z, T^{(2)0}\right] = 0$).

$$H_Q^{(1)}(t) = \frac{1}{\sqrt{6}} \sum_{m=-2,\neq 0}^{2} \omega_{Q,m}^{(2)0} T^{(2)0} e^{im\omega_r t} \tag{1.9}$$

Employing averaging methods, the second-order contributions (from time-dependent terms) to the quadrupolar interaction is derived and summarized by the following equation.

$$H_Q^{(2)} = -\frac{1}{12} \sum_{q=\pm 1,\pm 2} \sum_{m=\pm 1,\pm 2} \frac{\omega_{Q,m}^{(2)q} \omega_{Q,-m}^{(2)-q}}{q\omega - m\omega_r} \left[T^{(2)q}, T^{(2)-q}\right] \tag{1.10}$$

Retaining contributions to second-order, the quadrupolar Hamiltonian is represented by the following equation.

$$H_Q(t) = H_Q^{(1)}(t) + H_Q^{(2)}(t) \tag{1.11}$$

(ii) Dipolar interaction

The interaction between two nuclei take place either through bond (J-coupling) or through space (dipolar coupling). Owing to the smaller magnitude of the scalar interaction (or J-coupling), it is often ignored in solid state NMR. By contrast, due to restricted mobility, the through space interactions (or dipolar interactions) remain unaveraged and are anisotropic in nature. Accordingly, the Hamiltonian depicting the dipolar interaction between a heteronuclear spin pair is represented by the following equation.

$$H_{IS}(t) = \sum_{m=-2,\neq 0}^{2} 2\omega_{IS}^{(m)} e^{im\omega_r t} I_z S_z \tag{1.12}$$

The spatial components of the dipolar interactions in the PAS are represented by the following equation.

$$R_{P,dipolar}^{(2)0} = \sqrt{6} b \left(b = -\frac{\mu_0 \gamma_I \gamma_S}{4\pi r_{IS}^3} \right) \ , \ R_{P,dipolar}^{(2)\pm 2} = R_{P,dipolar}^{(2)\pm 1} = 0 \tag{1.13}$$

1.3.2 Time evolution of spins in NMR experiments

As measurements in NMR spectroscopy are made on bulk samples, the density matrix formalism [99] has remained the preferred approach for studying the dynamics of such systems. Accordingly, the state of system is described in terms of the density operator, $\rho(t)$ and the time-evolution of the system is studied using Quantum-Liouville equation.

$$i\frac{d\rho(t)}{dt} = [H(t), \rho(t)] \ \ , \ \ \hbar = 1 \tag{1.14}$$

When the Hamiltonian is time-independent, the formal solution to the above equation is straightforward and reduces to the following form.

$$\rho(t) = U(t,0)\,\rho(0)\,U^{-1}(t,0) = e^{-iHt}\rho(0)\,e^{iHt} \tag{1.15}$$

In the above equation, '$\rho(0)$' represents the initial state of the system at time t=0 and $\rho(t)$ is the state of the system at time 't'. Interestingly, in NMR experiments, the spin Hamiltonians are time-dependent. In such cases, the formal solution to the above equation has a complicated form.

$$\rho(t) = U(t,0)\,\rho(0)\,U^{-1}(t,0) = e^{-i\int_0^t H(t')dt'}\rho(0)\,e^{i\int_0^t H(t')dt'} \tag{1.16}$$

From an experimental perspective, analytic expressions are desirable for deducing optimal conditions and for quantifying the NMR experimental data. To address this issue, Waugh and Haeberlen in 1968 proposed the Average Hamiltonian Theory (AHT) [10,90] for describing MAS experiments in the solid state. In the average Hamiltonian framework, a time-averaged effective Hamiltonian is derived from the Magnus Expansion formula [104]. While descriptions based on Average Hamiltonian Theory (AHT) have been the preferred approach, methods based on Floquet theory [91–95,105,106] have also emerged to describe MAS experiments. Nevertheless, the utility and exactness of such methods requires a careful comparison between simulations emerging from analytical and numerical methods. A brief summary of the analytic methods is discussed in the Appendices.

1.4 Organization of the thesis

In chapter 2, the exactness of analytic methods for describing finite pulse effects in MAS experiments is discussed. Specifically, the finite pulse effects for three-level system is discussed and compared with those obtained from two-level systems. Depending on the relative magnitudes of the internal spin interactions with respect to the amplitude of the excitation pulse, the role of interaction frames in the derivation of time-propagators is discussed. For illustrative purposes, the exactness of time-propagators derived from analytic methods such as (a) AHT (b) Floquet theory (c) Floquet Magnus Expansion (FME) are also explored and discussed in detail through comparisons with simulations emerging from exact numerical methods.

In chapter 3, analytic theory of interference effects under MAS conditions is discussed within the density matrix formalism. Employing the time-propagators obtained from chapter-

2, analytic models are built for quantifying the interference effects between a spin-1/2 nucleus coupled to a quadrupolar spin (S=1). The exactness of the analytic models are verified rigorously through comparisons with simulations emerging from numerical methods.

In chapter 4, the results obtained in this thesis are summarized along with future perspectives.

Appendix A

Average Hamiltonian Theory (AHT)

The evolution of system in quantum mechanics is studied using the Quantum-Liouville equation given below.

$$i\frac{d\rho\left(t\right)}{dt}=\left[H\left(t\right),\rho\left(t\right)\right] \tag{A.1}$$

In the above equation, $\rho(t)$ represents the state of the system at time 't' and is evaluated using the standard solution.

$$\rho\left(t\right)=U\left(t,0\right)\rho\left(0\right)U^{-1}\left(t,0\right) \tag{A.2}$$

where $\rho(0)$ represents the initial state of the system at time t=0. The term U(t,0) denotes the evolution operator and has a complicated form.

$$U\left(t,0\right)=\hat{T}\exp\left(-i\int_{0}^{t}\left(H_{\text{int}}\left(t'\right)+H_{ext}\left(t'\right)\right)dt'\right) \tag{A.3}$$

where $\hat{T}$ represents the time ordering operator. The term $H_{int}(t)$ and $H_{ext}(t)$ denotes the internal and external Hamiltonian of the system respectively.

To reduce the complexities involved for describing the time-evolution of systems, Waugh and co-workers proposed an interaction frame [10,90] wherein, the evolution operator, $U\left(t,0\right)$, is expressed as a product of two exponential operators, representative of the internal and external Hamiltonians.

$$\begin{aligned}U\left(t,0\right)&=\hat{T}\exp\left(-i\int_{0}^{t}\left(H_{\text{int}}\left(t'\right)+H_{ext}\left(t'\right)\right)dt'\right)\\&=U_{RF}\left(t,0\right)U_{\text{int}}\left(t,0\right)\end{aligned} \tag{A.4}$$

where,

$$U_{RF}\left(t,0\right)=\hat{T}\exp\left(-i\int_{0}^{t}H_{ext}\left(t'\right)dt'\right) \tag{A.5}$$

$$U_{\text{int}}(t,0) = \hat{T}\exp\left(-i\int_0^t \widetilde{H}_{\text{int}}(t')\,dt'\right) \tag{A.6}$$

The internal Hamiltonian in the RF interaction frame ($\widetilde{H}_{int}(t)$) is derived through the following relation.

$$\widetilde{H}_{\text{int}}(t) = U_{RF}^{-1}(t,0)\,H_{\text{int}}(t)\,U_{RF}(t,0) \tag{A.7}$$

Utilizing the periodic properties of the Hamiltonians (both internal and external) and imposing the 'cyclic condition' (i.e. $U_{RF}(\tau_c,0)$=1), the evolution of spins in the interaction frame is described by an evolution operator comprising only the transformed internal Hamiltonian.

$$U(N\tau_c,0) = [U(\tau_c,0)]^N = [U_{\text{int}}(\tau_c,0)]^N = \left[\hat{T}\exp\left(-i\int_0^t \widetilde{H}_{\text{int}}(t')\,dt'\right)\right]^N \tag{A.8}$$

When the modulation frequencies of sample rotation $\left(\omega_r = \frac{2\pi}{\tau_r}\right)$ and pulse sequence $\left(\omega_c = \frac{2\pi}{\tau_c}\right)$ are commensurate ($\omega_c = N\omega_r$), the Magnus formula [104] presents an attractive option for deriving a time averaged Hamiltonian (internal) over a cycle (τ_c) in the RF interaction frame.

$$U(\tau_c,0) = U_{\text{int}}(\tau_c,0) = \exp\left(-i\overline{H}_{\text{int}}(\tau_c)\,\tau_c\right) \tag{A.9}$$

The time averaged Hamiltonian ($\overline{H}_{int}$) is valid only over the cycle time (τ_c) and is expressed through a series of corrections derived from Magnus expansion.

$$\overline{H}_{\text{int}}(\tau_c) = H^{(0)}(\tau_c) + H^{(1)}(\tau_c) + H^{(2)}(\tau_c) + H^{(3)}(\tau_c) + ... \tag{A.10}$$

$$H^{(0)}(\tau_c) = \frac{1}{\tau_c}\int_0^{\tau_c} \widetilde{H}_{\text{int}}(t')\,dt' \tag{A.11}$$

$$H^{(1)}(\tau_c) = -\frac{i}{2\tau_c}\int_0^{\tau_c} dt' \int_0^{t'} \left[\widetilde{H}_{\text{int}}(t'), \widetilde{H}_{\text{int}}(t'')\right] dt'' \tag{A.12}$$

.....

This forms the basis of stroboscopic detection (i.e. detection only at cycle times) in magnetic resonance. Employing the AHT framework, suites of multiple-pulse experiments have been designed in solids under both static and spinning conditions.

Appendix B

Effective Hamiltonians in Floquet theory

B.1 Floquet theory

In this section, a brief description of Floquet theory is presented. A more detailed discussion on Floquet theory along with its various formulations could be found in the literature [91–95, 105, 106]. We begin with the time-dependent Schrondinger equation with periodically time dependent Hamiltonians as given below.

$$i\hbar\frac{\partial\left|\psi\left(t\right)\right\rangle}{\partial t}=H\left(t\right)\left|\psi\left(t\right)\right\rangle \tag{B.1}$$

Following the procedure outlined by Shirley, both the wave function $\psi(t)$ and the Hamiltonian H(t) are expanded via Fourier series expansion.

$$H\left(t\right)=\sum_{n=-\infty}^{\infty}H^{(n)}e^{in\omega t}\ \ ;\ \ \left|\psi\left(t\right)\right\rangle=\sum_{n=-\infty}^{\infty}\sum_{\alpha}c_{\alpha}^{(n)}\left(t\right)e^{in\omega t}\left|\phi_{\alpha}\right\rangle \tag{B.2}$$

On substitution in Eq. B.2, the following equation is obtained.

$$\sum_{\gamma}\sum_{m=-\infty}^{\infty}\left[i\hbar\frac{\partial c_{\gamma}^{(m)}\left(t\right)}{\partial t}-m\hbar\omega c_{\gamma}^{(m)}\left(t\right)\right]e^{in\omega t}\left|\phi_{\gamma}\right\rangle=\sum_{\alpha,\beta}\sum_{n,n_{1}=-\infty}^{\infty}H_{\alpha\beta}^{(n_{1})}c_{\beta}^{(n)}\left(t\right)e^{i(n+n_{1})\omega t}\left|\phi_{\alpha}\right\rangle \tag{B.3}$$

In the above equation, the greek indices (α,β,γ) depict the spin state of the system, while, the indices (n, m, n1) denotes the Fourier index. Left multiplying Eq. B.3 by $\langle\phi_{\gamma}|$ and equating the like powers of exponentials on each side, the above equation reduces to a form originally obtained by Shirley.

$$i\hbar\frac{\partial c_{\gamma}^{(m)}\left(t\right)}{\partial t}=\sum_{\beta}\sum_{n=-\infty}^{\infty}\underbrace{\left(H_{\gamma\beta}^{(m-n)}+m\hbar\omega\delta_{\gamma,\beta}\delta_{m,n}\right)}_{H_{F}}c_{\beta}^{(n)}\left(t\right) \tag{B.4}$$

In the above equation, 'H_F' depicts the Floquet Hamiltonian defined in an infinite dimensional vector space. To describe the Floquet Hamiltonian in the infinite dimensional vector space, both the spin states and spin operators are dressed with Fourier indices.

$$\left|\phi_{\alpha}^{(n)}\right\rangle = |n\rangle \otimes |\phi_{\alpha}\rangle \tag{B.5}$$

$$\left\langle\phi_{\alpha}^{(m)}\right| H_F \left|\phi_{\beta}^{(n)}\right\rangle = H_{\alpha\beta}^{(m-n)} + m\hbar\omega\delta_{\alpha,\beta}\delta_{m,n} \tag{B.6}$$

To conveniently describe the spin dynamics in the Floquet space, a set of Fourier operators are defined.

$$F_m = \sum_{n=-\infty}^{\infty} |n\rangle \langle n+m| \quad , \quad I_F = n \sum_{n=-\infty}^{\infty} |n\rangle \langle n| \tag{B.7}$$

Here, I_F is defined as the Fourier number operator and F_m is the Fourier ladder operator. Consequently, the spin operators in the Floquet space are constructed by direct product of Fourier operators (F_m) and spin operators ($\hat{O}_p$).

$$\left[\hat{O}_p\right]_m = F_m \otimes \hat{O}_p \tag{B.8}$$

with the following commutator relations between them.

$$\left[I_F, \left[\hat{O}_p\right]_m\right] = m\left[\hat{O}_p\right]_m \quad , \quad \left[\left[\hat{O}_p\right]_m, \left[\hat{O}_q\right]_n\right] = \left[\hat{O}_p, \hat{O}_q\right]_{m+n} \tag{B.9}$$

B.2 Effective Floquet Hamiltonians- Floquet Contact Transformation

The contact transformation method is an operator equivalent of the Rayleigh Schrodinger perturbation theory [107–109] and has been extensively employed to derive effective Hamiltonians in magnetic resonance spectroscopy [95–98]. In this method, the Hamiltonian is rewritten as a sum of two terms comprising a zero order and perturbing Hamiltonian as depicted below.

$$H = H_0 + \lambda H_1 \tag{B.10}$$

In accord with the tenets of perturbation theory, the magnitude of perturbing Hamiltonian is less than that of the zero order Hamiltonian (i.e. $\|H_1\| \ll \|H_0\|$). Employing the perturbation parameter λ, the Hamiltonian in equation B.10 is transformed by a unitary transformation function, $U = exp\,(i\lambda S_1)$. The transformed Hamiltonian thus obtained is

expanded as a sum of various orders of corrections (ordered according to various powers of λ) as depicted below.

$$\begin{aligned}\widetilde{H} = UHU^{-1} &= e^{i\lambda S_1}\left(H_0 + \lambda H_1\right)e^{-i\lambda S_1} \\ &= H_0^{(1)} + \lambda H_1^{(1)} + \lambda^2 H_2^{(1)} + ... + \lambda^n H_n^{(1)}\end{aligned} \tag{B.11}$$

Employing Baker-Campbell-Hausdorff (BCH) formula [110], equation B.11 is expanded. Subsequently, various correction terms are derived by equating the powers of λ on both sides in the above equation.

$$H_0^{(1)} = H_0 \tag{B.12}$$

$$H_1^{(1)} = H_1 + i\left[S_1, H_0\right] \tag{B.13}$$

$$H_2^{(1)} = i\left[S_1, H_1\right] - \frac{1}{2}\left[S_1, \left[S_1, H_0\right]\right] \tag{B.14}$$

.....

$$H_n^{(1)} = \frac{i^n}{n!}\left[\underbrace{S_1, ...[S_1}_{n-1}, H_0]\right] + \frac{i^{n-1}}{n-1!}\left[\underbrace{S_1, ...[S_1}_{n-2}, H_1]\right] \tag{B.15}$$

The generator of the unitary transformation (S_1) is chosen to compensate the off-diagonality in H_1 and is obtained by solving the equation given below.

$$H_1^{(1)} = H_1 + i\left[S_1, H_0\right] = 0 \tag{B.16}$$

Subsequently, employing the transformation function (from Eq. B.16), the various orders of corrections in the Hamiltonian (Eq. B.13-B.15) are derived.

Appendix C

Floqet Magnus Expansion

The time-dependent Schrodinger equation in terms of the evolution operator is represented by the following equation.

$$i\frac{dU\left(t\right)}{dt}=H\left(t\right)U\left(t\right) \tag{C.1}$$

with $U(0)=I$ as initial condition and H(t), the periodic Hamiltonian (with period, T) i.e. H(t)=H(t+T). Employing Floquet theorem [91,92], the evolution operator is expressed as a product of terms given below.

$$U\left(t\right)=P\left(t\right)e^{-i\overline{H}t}\ ,\ P\left(t\right)=P\left(t+\tau\right) \tag{C.2}$$

Inserting the form of U(t) from Eq. C.2 into Eq. C.1.

$$i\frac{dP\left(t\right)}{dt}=H\left(t\right)P\left(t\right)-P\left(t\right)\overline{H} \tag{C.3}$$

where P(0)=I can be assumed but this is non-mandatory. Using the exponential ansatz from Magnus expansion [104], $P(t)=e^{-i\Lambda(t)}$ with $\Lambda(t+T)=\Lambda(t)$, the following form of the differential equation is obtained from Eq. C.3.

$$i\frac{d}{dt}\left\{e^{-i\Lambda(t)}\right\}=H\left(t\right)e^{-i\Lambda(t)}-e^{-i\Lambda(t)}\overline{H} \tag{C.4}$$

It may be noted that Eq. C.4 is independent of $\Lambda(0)$. The advantage of FME [111–113] approach lies in its ability to make a choice for $\Lambda(0)$. This allows further simplification of the perturbative calculations of $\Lambda(t)$ and $\overline{H}$. A choice of $\Lambda(0)\neq 0$ is equivalent to the use of more general representation of the evolution operator.

$$U\left(t\right)=P\left(t\right)e^{-i\overline{H}t}P^{\dagger}\left(0\right) \tag{C.5}$$

Substituting the perturbation expansions for $\Lambda(t)$ and $\overline{H}$ in Eq. C.4 provides the solution for $\Lambda_n(t)$ and $\overline{H}$.

$$\Lambda(t) = \sum_{n=1}^{\infty} \lambda^n \Lambda_n(t) \ , \ \overline{H} = \sum_{n=1}^{\infty} \lambda^n \overline{H}^{(n)} \tag{C.6}$$

$$\Lambda_n(t) = \Lambda_n(0) + \int_0^t G_n(t')\, dt' - t\overline{H}^{(n)} \tag{C.7}$$

$$\overline{H}^{(n)} = \frac{1}{T} \int_0^T G_n(t)\, dt \tag{C.8}$$

The terms $G_n(t)$ have the following forms at various orders:-

$$n = 1 \ ; \ G_1(t) = H(t) \tag{C.9}$$

$$n = 2 \ ; \ G_2(t) = -\frac{i}{2}\left[H(t) + \overline{H}^{(1)}, \Lambda_1(t)\right] \tag{C.10}$$

$$\begin{aligned} n = 3 \ ; \ G_3(t) = &-\frac{i}{2}\left[H(t) + \overline{H}^{(1)}, \Lambda_2(t)\right] - \frac{i}{2}\left[\overline{H}^{(2)}, \Lambda_1(t)\right] \\ &- \frac{1}{12}\left[\Lambda_1(t), \left[\Lambda_1(t), H(t) - \overline{H}^{(1)}\right]\right] \end{aligned} \tag{C.11}$$

Employing the time-dependent periodic Hamiltonian, H(t) ($H(t) = \sum_m H_m e^{im\omega t}$) with period T $\left(\omega = \frac{2\pi}{T}\right)$ in Eq. C.8-C.11, the expansion coefficients in $\Lambda(t)$ and $\bar{H}$ are derived and summarized below.

$$\Lambda_1(t) = \sum_{m \neq 0} \frac{H_m}{im\omega} \left\{e^{im\omega t} - 1\right\} + \Lambda_1(0) \tag{C.12}$$

$$\overline{H}^{(1)} = H_0 \tag{C.13}$$

$$\begin{aligned} \Lambda_2(t) = &-\frac{1}{2} \sum_{m \neq 0} \frac{[H_m, \Lambda_1(0)]}{m\omega} \left\{e^{im\omega t} - 1\right\} + i \sum_{m \neq 0} \frac{[H_0, H_m]}{m^2\omega^2} \left\{e^{im\omega t} - 1\right\} \\ &+ \frac{i}{2} \sum_{m \neq 0, n \neq 0} (1 - \delta_{m+n}) \frac{[H_m, H_n]}{m(m+n)\omega^2} \left\{e^{i(m+n)\omega t} - 1\right\} \\ &- \frac{i}{2} \sum_{m \neq 0, n \neq 0} \frac{[H_m, H_n]}{mn\omega^2} \left\{e^{im\omega t} - 1\right\} + \Lambda_2(0) \end{aligned} \tag{C.14}$$

$$\overline{H}^{(2)} = -i\left[H_0, \Lambda_1(0)\right] + \frac{1}{2} \sum_{m \neq 0} \frac{[H_m, H_{-m}]}{m\omega} + \sum_{m \neq 0} \frac{[H_0, H_m]}{m\omega} \tag{C.15}$$

The exact expressions for $\Lambda(t)$ and $\overline{H}$ depends on the choice of initial boundary condition (whether $\Lambda(0)$ is zero or non-zero) and is discussed below.

C.1 Normal Boundary Condition, $\Lambda(0) = 0$

In the normal boundary condition, $\Lambda(0)$ is set as zero and the expressions for $\Lambda(t)$ and $\overline{H}$ further simplified to form given below.

$$\Lambda_1(t) = \sum_{m\neq 0} \frac{H_m}{im\omega}\left\{e^{im\omega t} - 1\right\} \tag{C.16}$$

$$\overline{H}^{(1)} = H_0 \tag{C.17}$$

$$\begin{aligned}\Lambda_2(t) = i\sum_{m\neq 0}\frac{[H_0, H_m]}{m^2\omega^2}\left\{e^{im\omega t}-1\right\} + \frac{i}{2}\sum_{m\neq 0, n\neq 0}(1-\delta_{m+n})\frac{[H_m, H_n]}{m(m+n)\omega^2}\left\{e^{i(m+n)\omega t}-1\right\} \\ -\frac{i}{2}\sum_{m\neq 0, n\neq 0}\frac{[H_m, H_n]}{mn\omega^2}\left\{e^{im\omega t}-1\right\}\end{aligned} \tag{C.18}$$

$$\overline{H}^{(2)} = \frac{1}{2}\sum_{m\neq 0}\frac{[H_m, H_{-m}]}{m\omega} + \sum_{m\neq 0}\frac{[H_0, H_m]}{m\omega} \tag{C.19}$$

C.2 Alternate Boundary Condition, $\Lambda(0) \neq 0$

In the alternate boundary condition, $\Lambda(0)$ is set as non-zero. As $\Lambda_{n+1}(t)$ depends on $\Lambda_n(t)$, a suitable choice for $\Lambda_1(0)$ is made to avoid any increase in the number of terms.

$$\Lambda_1(0) = \sum_{m\neq 0}\frac{H_m}{im\omega} \tag{C.20}$$

$$\Lambda_1(t) = \sum_{m\neq 0}\frac{H_m}{im\omega}e^{im\omega t} \tag{C.21}$$

$$\overline{H}^{(1)} = H_0 \tag{C.22}$$

$$\Lambda_2(t) = i\sum_{m\neq 0}\frac{[H_0, H_m]}{m^2\omega^2}e^{im\omega t} + \frac{i}{2}\sum_{m\neq 0, n\neq 0}(1-\delta_{m+n})\frac{[H_m, H_n]}{n(m+n)\omega^2}e^{i(m+n)\omega t} \tag{C.23}$$

$$\overline{H}^{(2)} = \frac{1}{2}\sum_{m\neq 0}\frac{[H_m, H_{-m}]}{m\omega} \tag{C.24}$$

References

[1] A. Abragam, *The Principles of Nuclear Magnetism*, Oxford University Press, 1961.

[2] M. Mehring, *Principles of High Resolution NMR in Solids*, Springer-Verlag Berlin Heidelberg, 1983.

[3] C. P. Slichter, *Principles of Magnetic Resonance*, Springer, 1990.

[4] A. Ramamoorthy, *NMR Spectroscopy of Biological Solids*, CRC Press, 2005.

[5] R. E. Wasylishen, S. E. Ashbrook and S. Wimperis, *NMR of Quadrupolar Nuclei in Solid Materials*, John Wiley & Sons, 2012.

[6] J. V. Hanna and M. E. Smith, *Solid State Nuclear Magnetic Resonance*, 2010, **38**, 1–18.

[7] G. E. Maciel, *Science*, 1984, **226**, 282–288.

[8] E. R. Andrew, A. Bradbury and R. G. Eades, *Nature*, 1958, **182**, 1659–1659.

[9] I. J. Lowe, *Physical Review Letters*, 1959, **2**, 285–287.

[10] U. Haeberlen, *High Resolution NMR in Solids: Selective Averaging*, Academic Press, 1976.

[11] S. Hartmann and E. Hahn, *Physical Review*, 1962, **128**, 2042.

[12] A. Pines, M. G. Gibby and J. Waugh, *The Journal of Chemical Physics*, 1973, **59**, 569–590.

[13] A. L. Bloom and J. N. Shoolery, *Physical Review*, 1955, **97**, 1261.

[14] A. E. Bennett, C. M. Rienstra, M. Auger, K. Lakshmi and R. G. Griffin, *The Journal of Chemical Physics*, 1995, **103**, 6951–6958.

[15] B. Fung, A. Khitrin and K. Ermolaev, *Journal of Magnetic Resonance*, 2000, **142**, 97–101.

[16] E. Andrew, S. Clough, L. Farnell, T. Gledhill and I. Roberts, *Physics Letters*, 1966, **21**, 505–506.

[17] D. Raleigh, G. Harbison, T. Neiss, J. Roberts and R. Griffin, *Chemical Physics Letters*, 1987, **138**, 285–290.

[18] D. Raleigh, M. Levitt and R. G. Griffin, *Chemical Physics Letters*, 1988, **146**, 71–76.

[19] K. Takegoshi, K. Nomura and T. Terao, *Chemical Physics Letters*, 1995, **232**, 424–428.

[20] K. Takegoshi, K. Nomura and T. Terao, *Journal of Magnetic Resonance*, 1997, **127**, 206–216.

[21] T. Gullion and J. Schaefer, *Journal of Magnetic Resonance (1969)*, 1989, **81**, 196–200.

[22] T. Gullion and C. H. Pennington, *Chemical Physics Letters*, 1998, **290**, 88–93.

[23] C. P. Jaroniec, B. A. Tounge, C. M. Rienstra, J. Herzfeld and R. G. Griffin, *Journal of Magnetic Resonance*, 2000, **146**, 132–139.

[24] A. Jerschow, *Progress in Nuclear Magnetic Resonance Spectroscopy*, 2005, **46**, 63–78.

[25] P. P. Man, *Encyclopedia of Nuclear Magnetic Resonance*, 2007, **6**, 3838.

[26] E. Kundla, A. Samoson and E. Lippmaa, *Chemical Physics Letters*, 1981, **83**, 229–232.

[27] A. Samoson, E. Kundla and E. Lippmaa, *Journal of Magnetic Resonance (1969)*, 1982, **49**, 350–357.

[28] S. Ganapathy, S. Schramm and E. Oldfield, *The Journal of Chemical Physics*, 1982, **77**, 4360–4365.

[29] E. Oldfield and R. J. Kirkpatrick, *Science*, 1985, **227**, 1537–1544.

[30] A. Llor and J. Virlet, *Chemical Physics Letters*, 1988, **152**, 248–253.

[31] A. Samoson, E. Lippmaa and A. Pines, *Molecular Physics*, 1988, **65**, 1013–1018.

[32] B. Chmelka, K. T. Mueller, A. Pines, J. Stebbins, Y. Wu and J. Zwanziger, *Nature*, 1989, **339**, 42–43.

[33] L. Frydman and J. S. Harwood, *Journal of the American Chemical Society*, 1995, **117**, 5367–5368.

[34] A. Medek, J. S. Harwood and L. Frydman, *Journal of the American Chemical Society*, 1995, **117**, 12779–12787.

[35] C. Fernandez and J. Amoureux, *Chemical Physics Letters*, 1995, **242**, 449–454.

[36] C. Fernandez and J. Amoureux, *Solid State Nuclear Magnetic Resonance*, 1996, **5**, 315–321.

[37] D. Massiot, B. Touzo, D. Trumeau, J. Coutures, J. Virlet, P. Florian and P. Grandinetti, *Solid State Nuclear Magnetic Resonance*, 1996, **6**, 73–83.

[38] G. Wu, D. Rovnyank, B. Sun and R. G. Griffin, *Chemical Physics Letters*, 1996, **249**, 210–217.

[39] S. P. Brown, S. J. Heyes and S. Wimperis, *Journal of Magnetic Resonance, Series A*, 1996, **2**, 280–284.

[40] J.-P. Amoureux, C. Fernandez and L. Frydman, *Chemical Physics Letters*, 1996, **259**, 347–355.

[41] J.-P. Amoureux, C. Fernandez and S. Steuernagel, *Journal of Magnetic Resonance*, 1996, **123**, 116–118.

[42] S. P. Brown and S. Wimperis, *Journal of Magnetic Resonance*, 1997, **128**, 42–61.

[43] Z. Gan and H.-T. Kwak, *Journal of Magnetic Resonance*, 2004, **168**, 346–351.

[44] A. Goldbourt and P. K. Madhu, *Multiple-quantum magic-angle spinning: High-resolution solid state NMR spectroscopy of half-integer quadrupolar nuclei*, Springer, 2002, pp. 17–54.

[45] J. Rocha, C. M. Morais and C. Fernandez, *New Techniques in Solid-State NMR*, 2005, 141–194.

[46] P. Madhu, A. Goldbourt, L. Frydman and S. Vega, *Chemical Physics Letters*, 1999, **307**, 41–47.

[47] P. Madhu, A. Goldbourt, L. Frydman and S. Vega, *The Journal of Chemical Physics*, 2000, **112**, 2377–2391.

[48] T. Vosegaard, D. Massiot and P. J. Grandinetti, *Chemical Physics Letters*, 2000, **326**, 454–460.

[49] A. Goldbourt, P. Madhu and S. Vega, *Chemical Physics Letters*, 2000, **320**, 448–456.

[50] P. Madhu and M. Levitt, *Journal of Magnetic Resonance*, 2002, **155**, 150–155.

[51] D. Iuga, H. Schäfer, R. Verhagen and A. P. Kentgens, *Journal of Magnetic Resonance*, 2000, **147**, 192–209.

[52] D. Iuga and A. P. Kentgens, *Chemical Physics Letters*, 2001, **343**, 556–562.

[53] D. Iuga and A. P. Kentgens, *Journal of Magnetic Resonance*, 2002, **158**, 65–72.

[54] G. Wu, D. Rovnyak and R. G. Griffin, *Journal of the American Chemical Society*, 1996, **118**, 9326–9332.

[55] K. H. Lim and C. P. Grey, *Solid State Nuclear Magnetic Resonance*, 1998, **13**, 101–112.

[56] T. Mildner, M. Smith and R. Dupree, *Chemical Physics Letters*, 1999, **306**, 297–302.

[57] T. Mildner, M. Smith and R. Dupree, *Chemical Physics Letters*, 1999, **301**, 389–394.

[58] J. D. Walls, K. H. Lim and A. Pines, *The Journal of Chemical Physics*, 2002, **116**, 79–90.

[59] J. D. Walls, K. H. Lim, J. W. Logan, J. T. Urban, A. Jerschow and A. Pines, *The Journal of Chemical Physics*, 2002, **117**, 518–532.

[60] F. H. Larsen, H. J. Jakobsen, P. D. Ellis and N. C. Nielsen, *The Journal of Physical Chemistry A*, 1997, **101**, 8597–8606.

[61] T. Vosegaard, F. H. Larsen, H. Jakobsen, P. D. Ellis and N. Nielsen, *Journal of the American Chemical Society*, 1997, **119**, 9055–9056.

[62] F. H. Larsen and N. C. Nielsen, *The Journal of Physical Chemistry A*, 1999, **103**, 10825–10832.

[63] A. W. Hing, S. Vega and J. Schaefer, *Journal of Magnetic Resonance (1969)*, 1992, **96**, 205–209.

[64] C. P. Grey and W. S. Veeman, *Chemical Physics Letters*, 1992, **192**, 379–385.

[65] C. P. Grey, W. S. Veeman and A. J. Vega, *The Journal of Chemical Physics*, 1993, **98**, 7711–7724.

[66] T. Gullion, *Chemical Physics Letters*, 1995, **246**, 325–330.

[67] T. Gullion, *Journal of Magnetic Resonance*, 1995, **117**, 326–329.

[68] A. Goldbourt, *Israel Journal of Chemistry*, 2014, **54**, 125–135.

[69] M. Pruski, D. Lang, C. Fernandez and J. Amoureux, *Solid State Nuclear Magnetic Resonance*, 1997, **7**, 327–331.

[70] C. Fernandez, L. Delevoye, J.-P. Amoureux, D. Lang and M. Pruski, *Journal of the American Chemical Society*, 1997, **119**, 6858–6862.

[71] S. E. Ashbrook, S. P. Brown and S. Wimperis, *Chemical Physics Letters*, 1998, **288**, 509–517.

[72] S. E. Ashbrook and S. Wimperis, *Journal of Magnetic Resonance*, 2000, **147**, 238–249.

[73] S. E. Ashbrook and S. Wimperis, *Chemical Physics Letters*, 2001, **340**, 500–508.

[74] K. H. Lim and C. P. Grey, *The Journal of Chemical Physics*, 2000, **112**, 7490–7504.

[75] D. Rovnyak, M. Baldus and R. G. Griffin, *Journal of Magnetic Resonance*, 2000, **142**, 145–152.

[76] D. H. Brouwer and J. A. Ripmeester, *Journal of Magnetic Resonance*, 2007, **185**, 173–178.

[77] L. Duma, D. Abergel, P. Tekely and G. Bodenhausen, *Chemical Communications*, 2008, 2361–2363.

[78] R. S. Stein, B. Elena and L. Emsley, *Chemical Physics Letters*, 2008, **458**, 391–395.

[79] H. K. Miah, D. A. Bennett, D. Iuga and J. J. Titman, *Journal of Magnetic Resonance*, 2013, **235**, 1–5.

[80] G. Hou, S. Paramasivam, S. Yan, T. Polenova and A. J. Vega, *Journal of the American Chemical Society*, 2013, **135**, 1358–1368.

[81] G. Hou, R. Gupta, T. Polenova and A. J. Vega, *Israel Journal of Chemistry*, 2014, **54**, 171–183.

[82] M. K. Pandey, M. Malon, A. Ramamoorthy and Y. Nishiyama, *Journal of Magnetic Resonance*, 2015, **250**, 45–54.

[83] M. K. Pandey and Y. Nishiyama, *Solid State Nuclear Magnetic Resonance*, 2015, **70**, 15–20.

[84] M. Bak, J. T. Rasmussen and N. C. Nielsen, *Journal of Magnetic Resonance*, 2000, **147**, 296–330.

[85] M. Veshtort and R. G. Griffin, *Journal of Magnetic Resonance*, 2006, **178**, 248–282.

[86] S. Vega and A. Pines, *The Journal of Chemical Physics*, 1977, **66**, 5624–5644.

[87] S. Vega, *The Journal of Chemical Physics*, 1978, **68**, 5518–5527.

[88] S. Vega and Y. Naor, *The Journal of Chemical Physics*, 1981, **75**, 75–86.

[89] A. J. Vega, *Journal of Magnetic Resonance (1969)*, 1992, **96**, 50–68.

[90] U. Haeberlen and J. S. Waugh, *Physical Review*, 1968, **175**, 453.

[91] G. Floquet, *Annales scientifiques de l'École normale supérieure*, 1883, **12**, 47–89.

[92] J. H. Shirley, *Physical Review*, 1965, **138**, 979–987.

[93] T. Levante, M. Baldus, B. Meier and R. Ernst, *Molecular Physics*, 1995, **86**, 1195–1212.

[94] B. C. Filip, X. Filip, Demco and D. E. Siegfried Hafner, *Molecular Physics*, 1997, **92**, 757–772.

[95] R. Ramesh and M. S. Krishnan, *The Journal of Chemical Physics*, 2001, **114**, 5967.

[96] R. Garg and R. Ramachandran, *The Journal of Chemical Physics*, 2017, **146**, 184201.

[97] S. Ganguly, R. Garg and R. Ramachandran, *The Journal of Chemical Physics*, 2020, **153**, 094103.

[98] M. Bansal and R. Ramachandran, *Journal of Magnetic Resonance Open*, 2022, **10**, 100042.

[99] K. Blum, *Density matrix theory and applications*, Springer Science & Business Media, 2012, vol. 64.

[100] S. A. Smith, W. E. Palke and J. Gerig, *Concepts in Magnetic Resonance*, 1992, **4**, 107–144.

[101] S. A. Smith, W. E. Palke and J. Gerig, *Concepts in Magnetic Resonance*, 1992, **4**, 181–204.

[102] P. P. Man, *Concepts in Magnetic Resonance Part A*, 2013, **42**, 197–244.

[103] P. P. Man, *Concepts in Magnetic Resonance Part A*, 2016, **45**, e21385.

[104] W. Magnus, *Communications on Pure and Applied Mathematics*, 1954, **7**, 649–673.

[105] M. Leskes, P. Madhu and S. Vega, *Progress in Nuclear Magnetic Resonance Spectroscopy*, 2010, **57**, 345 – 380.

[106] I. Scholz, J. D. van Beek and M. Ernst, *Solid State Nuclear Magnetic Resonance*, 2010, **37**, 39 – 59.

[107] J. Van Vleck, *Physical Review*, 1929, **33**, 467.

[108] M. R. Aliev and V. T. Aleksanyan, *Optica Spectroscopia*, 1968, **24**, 520.

[109] M. R. Aliev and V. T. Aleksanyan, *Optica Spectroscopia*, 1968, **24**, 695.

[110] J. Campbell, *Proceedings of the London Mathematical Society*, 1896, **1**, 381–390.

[111] F. Casas, J. Oteo and J. Ros, *Journal of Physics A: Mathematical and General*, 2001, **34**, 3379.

[112] S. Blanes, F. Casas, J.-A. Oteo and J. Ros, *Physics Reports*, 2009, **470**, 151–238.

[113] E. S. Mananga and T. Charpentier, *The Journal of Chemical Physics*, 2011, **135**, 044109.

Chapter 2

Analytic theory of finite pulse effects in rotating solids

2.1 Background

The versatility of nuclear magnetic resonance (NMR) spectroscopy as a preferred analytic tool results from its inherent ability to manipulate spin interactions at the atomic level [1–3]. From an operational perspective, the development of sophisticated theoretical methods (both numerical and analytical) for quantifying the response of nuclear spins subjected to RF pulses [4–9] has been instrumental in enhancing the repertoire of NMR spectroscopy as a reliable tool for probing molecular structure in systems of varying complexities [10,11]. Through controlled manipulation of the spin interactions [2,5,12,13], the molecular constraints desired for structure determination are estimated systematically through multi-dimensional experiments [14–19]. Here in this chapter, we focus on the form of the spin Hamiltonians [2,5,20,21] governing the evolution of spins during a pulse. From an experimental perspective, the anisotropic nature of the spin interactions (such as chemical shift anisotropy (CSA), dipolar interactions, quadrupolar interactions etc.) results in a distribution of resonance frequencies. Consequently, the overall excitation efficiency depends on both the internal (magnitude of anisotropic interactions) and external parameters (such as the amplitude and duration of the pulse) in addition to the sample rotation frequency employed in magic angle spinning (MAS) experiments [22,23].

When the amplitude of the radio frequency (RF) pulse largely exceeds the magnitude of the internal spin interactions, it is customary to ignore the effects of the internal Hamiltonians during the pulse (commonly referred to as the strong pulse/ ideal pulse limit). The more

challenging case arises when the magnitude of the internal interaction exceeds (or is on par with) both the RF amplitude of the pulse and the sample rotation frequency. Such conditions are often encountered in the description of transitions in multi-level systems [2,8,24] (e.g. quadrupolar spins, I>1/2). In particular, analytic description of excitation in quadrupolar nuclei under spinning conditions is less straightforward [25–29] owing to the domineering presence of the quadrupolar interaction and has remained a challenging problem.

From an operational standpoint, the complexities encountered in theoretical studies involving quadrupolar nuclei could be attributed to (i) the larger magnitude of the quadrupolar interaction with respect to the amplitude of the excitation pulse (ii) the presence of multiple spin states (iii) the time-dependence of the spin interactions due to physical rotation of the sample. Although, development of analytical methods in static solids [8,25–34] have enhanced our basic understanding of the experiments, straightforward extensions to rotating solids remain less trivial [29,35–38]. In particular, a uniform analytical framework that analyses the role of the sample spinning frequency, amplitude of the RF pulse and the quadrupolar coupling constant in MAS experiments remains an open problem [39,40]. Consequently, optimizations based on numerical methods [6,7] have gained prominence in the development of NMR methods in quadrupolar nuclei. While investigations based on numerical methods are easier to implement and provide results, they do not necessarily afford insights into the physical phenomena under study.

Although, excitation in both static and spinning samples (predominantly in spin I=1/2 systems) is understood within certain approximations, a careful review of the available analytic methods is desirable to address the challenges encountered in the description of transitions in multi-level systems. With this objective, the validity of the approximations employed in the analytic methods are verified over wide range of parameters through comparisons with simulations emerging from analytic and exact numerical methods. To pedagogically describe the relevance of the methods, the excitation in static and spinning samples is discussed separately using theoretical methods based on perturbation theory [41–43].

2.2 Statement of Problem

To illustrate the relevance of analytic methods, we begin with numerical simulations depicting the excitation of double-quantum (DQ) transitions in spin I=1 system (as illustrated in Figure 2.1).

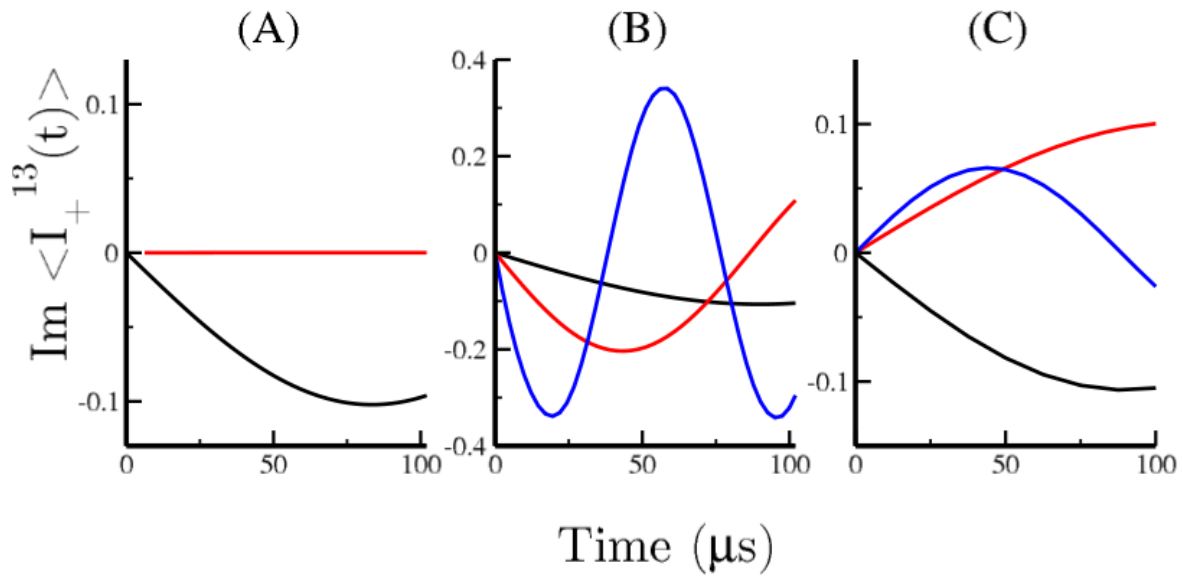

Figure 2.1: In the MAS simulations depicted, excitation of DQ transition in spin I=1 system is presented. (A) The black line represent numerical simulations [7] at even multiples of $\frac{\tau_r}{4}$ while the red line represent numerical simulations at odd multiples of $\frac{\tau_r}{4}$. The following parameters were employed in the simulations: $C_Q = 1$ MHz, $\nu_r = 40$ kHz ($\tau_r = 25\mu$s) and RF amplitude, $\nu_1 = 10$ kHz (B) Variation of RF amplitude (Black line- $\nu_1 = 10$ kHz, Red line- $\nu_1 = 20$ kHz, Blue line- $\nu_1 = 40$ kHz) (C) Variation of spinning frequency (Black line- $\nu_r = 40$ kHz, Red line- $\nu_r = 60$ kHz, Blue line- $\nu_r = 80$ kHz).

In the simulations depicted in panel A (Fig. 2.1), the excitation of DQ transitions at integral multiples of $\frac{\tau_r}{4}$ (where τ_r denotes the rotor period, $\tau_r = \frac{2\pi}{\omega_r}$ with ω_r depicting the sample rotation frequency) is illustrated. As depicted (panel A, Fig. 2.1), the excitation efficiency tends to zero at odd multiples of $\frac{\tau_r}{4}$ (indicated in red color) while it remains oscillatory at even multiples of $\frac{\tau_r}{4}$ (indicated in black color). In a similar vein, the DQ excitation efficiency increases with an increase in the RF amplitude (refer to panel B, Fig. 2.1) and decreases with an increase in the spinning frequency (refer to panel C, Fig. 2.1). Such observations are intriguing and have remained unexplained (using both numerical as well as analytical methods). This forms the motivation behind this chapter.

To address the above issues, the suitability of analytical methods routinely employed for describing the time-evolution of quantum mechanical systems governed by time-dependent Hamiltonians is examined. Specifically, the suitability of analytical methods based on Average Hamiltonian theory (AHT) [5,44] and Floquet theory [45–51] for studying the excitation of double-quantum (DQ) transitions in spin-1 system under MAS conditions is investigated. While

the applicability of these methods is well established in time-evolution studies involving spin I=1/2 systems, their suitability in the description of periodically driven multi-level systems remains less explored. For pedagogical reasons, the approximations employed in the description of excitation in two-level systems (both static and spinning samples) is reviewed briefly to explicate the nuances of excitation in multi-level systems.

2.3 Results and Discussion

2.3.1 Finite pulse effects in spin I=1/2 system

To describe the interplay between the internal and external interactions, we begin with the Hamiltonian of an isolated spin-1/2 system in a rotating solid.

$$H(t) = \underbrace{\omega_0 I_z}_{H_Z} + \underbrace{2\omega_1 \cos(\omega t)\, I_x}_{H_{RF}} + \underbrace{\sum_{m=-2,\neq 0}^{2} \omega^{(m)} e^{im\omega_r t} I_z}_{H_{CSA}} \; ; \; \hbar = 1 \tag{2.1}$$

In the above equation, H_Z depicts the interaction between the nuclear spin magnetic moment and the static magnetic field, while, the interaction between the magnetic moment with the oscillating magnetic field is represented by, H_{RF}. The angular frequency 'ω_0' denotes the precessional frequency (that includes chemical shielding effects) of the nucleus, while, 'ω_1' and 'ω' represent the amplitude and frequency of the oscillating field, respectively. To study the time-evolution under the internal Hamiltonians, the above Hamiltonian is transformed into the rotating frame ($U = e^{i\omega t I_z}$) such that the RF Hamiltonian is reduced to a simpler form (under secular approximation) as given below.

$$H_R(t) = UH(t)U^{-1} = \Delta\omega I_z + \omega_1 I_x + \sum_{m=-2,\neq 0}^{2} \omega^{(m)} e^{im\omega_r t} I_z \tag{2.2}$$

The term $\Delta\omega = \omega_0 - \omega$ represents the offset in the rotating frame.

2.3.1.1 Time-Evolution in static case

To begin with, let us consider the simplest case of on-resonance irradiation ($\Delta\omega$=0) in static samples (ω_r=0). To facilitate analytic description, the Hamiltonian in the rotating frame is transformed through the rotation operator ($U_1 = e^{i\pi/2 I_y}$) such that the RF field is quantized along the z-direction.

$$H_T = \omega_1 I_z + \omega' I_x \tag{2.3}$$

where

$$\omega' = \sum_{m=\pm 2,0} R_{PAS}^{(2)m} D_{m,0}\left(\Omega_{PL}\right)$$

When the amplitude of the driving field (ω_1) largely exceeds the off-diagonal terms (comprising offset and CSA terms), the effective Hamiltonian reduces to a simpler form.

$$H_{eff} = \omega_1 I_z \tag{2.4}$$

Subsequently, the evolution of the system during a pulse is evaluated using the standard procedure given below.

$$\langle I_y(t)\rangle = Tr\left[\rho(t) I_y\right] = Tr\left[e^{-iH_{eff}t}\tilde{\rho}(0)e^{iH_{eff}t}.\tilde{I}_y\right] = -\sin\left(\omega_1 t\right) \tag{2.5}$$

In the above eq., $\tilde{\rho}(0)$ represents the initial density operator in the tilted-rotating frame ($\tilde{\rho}(0) = U_1\rho(0)\ U_1^{-1} = -I_x\ \ ;\ \ \rho(0) = I_z$) while, the detection operator, I_y remains invariant in the tilted rotating frame ($\tilde{I_y} = I_y$).

When the amplitude of the pulse is greater than the off-diagonal terms, the ideal pulse approximation commonly employed in magnetic resonance remains valid ($\omega_1 > 8\omega'$, $\Delta\omega = 0$). As depicted in Figure 2.2, the ideal pulse approximation (indicated in red broken line) breaks down with increase in the magnitude of the off-diagonal terms. To improve the exactness of the analytic simulations, operator based perturbation theory [41–43] is employed in the present study. In contrast to the traditional Rayleigh-Schrödinger perturbation theory, the perturbation corrections are described in terms of effective Hamiltonians leading to better insights into the excitation process. Accordingly, depending on the relative magnitudes of the internal and external parameters, we outline the strategies employed in the derivation of effective Hamiltonians.

For operational purpose, the Hamiltonian in perturbative methods is split and re-expressed in terms of a zero-order and perturbing Hamiltonian. Depending on the relative magnitudes of ω_1 and ω', the following two regimes are identified and discussed.

Case-I: $\omega_1 > \omega'$ **(Regime-I)**

When the amplitude of the excitation pulse exceeds the magnitude of the internal interactions (denoted by ω'), the dominant term is identified with H_0 as given below.

$$H = \underbrace{\omega_1 I_z}_{H_0} + \lambda \underbrace{\omega' I_x}_{H_1} \tag{2.6}$$

Employing the method of contact transformation, the Hamiltonian 'H' is transformed into an effective Hamiltonian.

$$H_{eff} = e^{i\lambda S_1} H e^{-i\lambda S_1} \tag{2.7}$$

In the above equation, 'λ' denotes the perturbation parameter and is employed for ordering purposes only. Employing the BCH formula [52] and equating like powers of 'λ', the perturbation corrections (to different orders) are derived in terms of operators.

$$H_0^{(1)} = H_0$$

$$H_1^{(1)} = H_1 + i\left[S_1, H_0\right]$$

$$H_2^{(1)} = -\frac{1}{2!}\left[S_1, \left[S_1, H_0\right]\right] + i\left[S_1, H_1\right]$$

$$H_n^{(1)} = H_n + \sum_{m=0}^{n-1} \frac{i^{n-m}}{(n-m)!} \left[\underbrace{S_1, \left[S_1 ..... \right.}_{n-m} \left[S_1, H_m\right] ....\right] \tag{2.8}$$

In the above representation of the corrections ($H_n^{(k)}$), the subscript 'n' denotes the order of correction, while, 'k' denotes the number of transformations employed in the derivation of the effective Hamiltonian. The transformation function 'S_1' is chosen to compensate the off-diagonal contributions to order λ (i.e. S_1=i$C_y I_y$) and is derived employing the equation given below.

$$H_1^{(1)} = H_1 + i\left[S_1, H_0\right] = 0 \Rightarrow C_y = \frac{\omega'}{i\omega_1} \tag{2.9}$$

Subsequently, employing the above form of S_1, the second order correction to the effective Hamiltonian is derived as given below.

$$H_2^{(1)} = \frac{i}{2}\left[S_1, H_1\right] = \frac{\left(\omega'\right)^2}{2\omega_1} I_z \tag{2.10}$$

To second order, the effective Hamiltonian reduces to the following form.

$$H_{eff} = \omega_1 \left(1 + \frac{1}{2}\left(\frac{\omega'}{\omega_1}\right)^2\right) I_z = \omega_{eff} I_z \tag{2.11}$$

To have a consistent description, both the initial density operator ($\tilde{\rho}(0) = e^{i\pi/2I_y} I_z e^{-i\pi/2I_y} = -I_x$) and detection operator (I_y) is transformed using the transformation function, S_1.

$$\rho_{eff}(0) = e^{i\lambda S_1} \tilde{\rho}(0) e^{-i\lambda S_1} \;\; ; \;\; I_{y,eff} = I_y \tag{2.12}$$

Subsequently, employing the effective Hamiltonian, the state of the system during a pulse is determined.

$$\rho_{eff}(t) = e^{-iH_{eff}t} \rho_{eff}(0) e^{iH_{eff}t} = -\cos\left(\frac{\omega'}{\omega_1}\right)\left[I_x \cos\left(\omega_{eff} t\right) + I_y \sin\left(\omega_{eff} t\right)\right] - \sin\left(\frac{\omega'}{\omega_1}\right) I_z \tag{2.13}$$

Accordingly, the observable during excitation is evaluated by calculating the expectation value associated with the 'I_y' operator.

$$\langle I_y(t)\rangle = Tr\left[\rho_{eff}(t)I_{y,eff}\right] = -\cos\left(\frac{\omega'}{\omega_1}\right)\sin\left(\omega_{eff}t\right) \tag{2.14}$$

Case-II: $\omega' > \omega_1$ (Regime-II)

When the magnitude of the internal interaction, ω' exceeds the RF amplitude, ω_1, the definition of the zero-order and perturbing Hamiltonian is altered accordingly.

$$H = \underbrace{\omega' I_x}_{H_0} + \lambda \underbrace{\omega_1 I_z}_{H_1} \tag{2.15}$$

Employing the transformation function, S_1 ($S_1 = i(\frac{i\omega_1}{\omega'})I_y$) and following the procedure described in the previous section, the effective Hamiltonian to second order is derived.

$$H_{eff} = \omega'\left(1 + \frac{1}{2}\left(\frac{\omega_1}{\omega'}\right)^2\right)I_x = \omega_{eff}I_x \tag{2.16}$$

Subsequently, the final form of the signal is calculated and given by the following expression.

$$\langle I_y(t)\rangle = -\sin\left(\frac{\omega_1}{\omega'}\right)\sin\left(\omega_{eff}t\right) \tag{2.17}$$

As depicted in Figure 2.2, the analytic simulations are valid only in their respective domains (Regime-I, blue dots for $\omega_1 > \omega'$ and Regime-II, green dots for $\omega_1 < \omega'$). In the following subsection, a more general framework suited for describing the excitation in all regimes is explored.

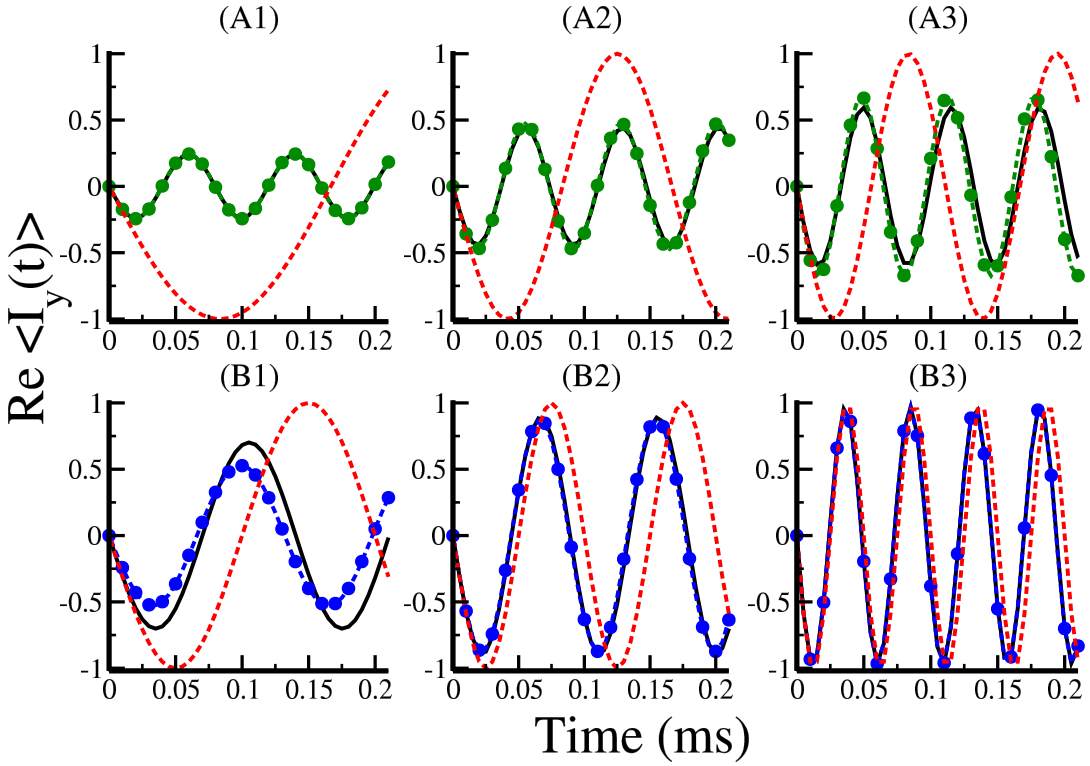

Figure 2.2: In the simulations (static case) depicted, the validity of the ideal pulse limit is probed by varying the amplitude of the RF pulse. The analytic simulations based on the ideal pulse approximation (indicated by red broken lines) and perturbative methods (Regime-I, blue dots ; Regime-II, green dots are compared with those obtained from exact numerical methods based on SPINEVOLUTION [7] (indicated by black lines). The following parameters were used in the simulations: (A1) $\omega_1 = (1/4)\omega'$ (A2) $\omega_1 = (1/2)\omega'$ (A3) $\omega_1 = (3/4)\omega'$ (B1) $\omega_1 = \omega'$ (B2) $\omega_1 = 2\omega'$ (B3) $\omega_1 = 4\omega'$

Case-III: Effective Field approach

To extend the perturbative approach across all regimes, an alternate method based on the concept of effective fields is explored in this section. Since the Hamiltonian for a two-level system (Eq. 2.3) has components along orthogonal axis (say z and x), the Hamiltonian is rotated through an angle 'θ' such that the effective field is quantized along one of the axis (say z or x). Depending on the choice of the quantization axis, the form of the rotation operator differs. When the quantization axis is along z-direction, the rotation operator, $U_2 = e^{i\theta I_y}$ is employed (for quantization along x-axis, $U_2 = e^{i(\pi/2-\theta)I_y}$ is employed). Employing the above rotation operator, the Hamiltonian in the tilted rotating frame ($H_T = \omega_1 I_z + \omega' I_x$) is

transformed such that the effective field is quantized along the z-axis.

$$H_{eff} = e^{i\theta I_y} H_T e^{-i\theta I_y} = \underbrace{\sqrt{\omega_1^2 + \omega'^2}}_{\omega_{eff}} I_z \;\; ; \;\; \theta = \tan^{-1}\left(\frac{\omega'}{\omega_1}\right) \tag{2.18}$$

In accord with the procedure described in the previous section, both the operators (initial density operator and detection operator) are transformed.

$$\rho_{eff}(0) = e^{i\theta I_y}\,(-I_x)\,e^{-i\theta I_y} = -I_x\cos\theta - I_z\sin\theta \tag{2.19}$$

$$I_{y,eff} = I_y$$

Accordingly, in the effective field formulation, the state of the system during a pulse is evaluated and the excitation is described using the following equations.

$$\rho_{eff}(t) = -\cos\theta\left[I_x\cos\left(\omega_{eff}t\right) + I_y\sin\left(\omega_{eff}t\right)\right] - I_z\sin\theta \tag{2.20}$$

$$\langle I_y(t)\rangle = -\cos\theta\sin\left(\omega_{eff}t\right) \tag{2.21}$$

Alternatively, when the effective field is quantized along x-axis, the final form of the signal expression reduces to the following form.

$$\langle I_y(t)\rangle = -\cos\theta\sin\left(\omega_{eff}t\right) \;\; ; \;\; \theta = \tan^{-1}\left(-\frac{\omega'}{\omega_1}\right) \tag{2.22}$$

From an operational perspective, the effective Hamiltonian derived from the effective field approach (Eq. 2.18) is more general and could be employed to derive the effective Hamiltonians derived in previous examples (case-I and case-II).

$$\omega_{eff} = \sqrt{(\omega_1)^2 + (\omega')^2} = \omega_1\left(1 + \frac{1}{2}\left(\frac{\omega'}{\omega_1}\right)^2\right) \quad \text{or} \quad \omega_{eff} = \sqrt{(\omega_1)^2 + (\omega')^2} = \omega'\left(1 + \frac{1}{2}\left(\frac{\omega_1}{\omega'}\right)^2\right)$$

As depicted in Figure 2.3 (violet dots), the analytic simulations based on the effective field approach are in excellent agreement in all the regimes, irrespective of the relative magnitudes of ω' and ω_1.

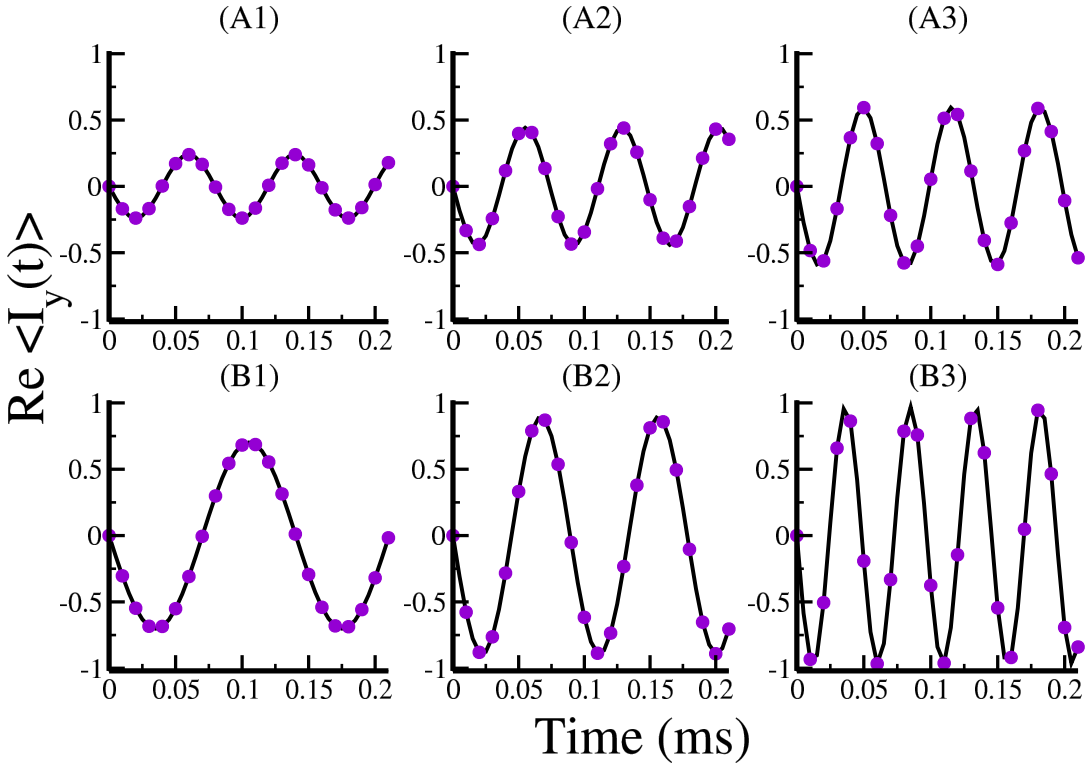

Figure 2.3: In the simulations (static case) depicted, the validity of the effective field approach is verified through a comparison between analytic simulations (indicated by violet dots) and those based on SPINEVOLUTION [7] (indicated by black solid lines). The following parameters were used in the simulations: (A1) $\omega_1 = (1/4)\omega'$ (A2) $\omega_1 = (1/2)\omega'$ (A3) $\omega_1 = (3/4)\omega'$ (B1) $\omega_1 = \omega'$ (B2) $\omega_1 = 2\omega'$ (B3) $\omega_1 = 4\omega'$

2.3.1.2 Time-Evolution in MAS case

To explain the nuances of the excitation in rotating solids, we begin with parameters that correspond to single crystal with specific orientations ($\Omega_{PM} = (0, 90, 0)$, η=1.0). Under on-resonance irradiation, based on the above choice of orientations, the Hamiltonian (Eq. 2.2) reduces to the following form ($\omega^{(2)} = \omega^{(-2)} = \omega'$ and $\omega^{(\pm 1)}$=0).

$$H_R(t) = 2\omega' \cos(2\omega_r t)\, I_z + \omega_1 I_x \tag{2.23}$$

It is important to note that the above choice of orientations is purely for demonstrative purposes and the discussion that follows is equally valid for any arbitrary orientation.

Depending on the relative magnitudes of the internal interactions (CSA interaction in this case) with respect to the external parameters (spinning frequency and rf amplitude), two

regimes (namely weak coupling regime and strong coupling regime) are identified. A detailed description of the excitation in the two regimes is presented in the following subsections.

1. Weak Coupling Regime

When the magnitude of the external parameters (spinning frequency or RF amplitude or both) exceeds the magnitude of the internal spin interactions (CSA interaction), the internal interaction acts as a perturbation, and is identified with the weak coupling regime. To facilitate analytic description in the weak coupling regime, the Hamiltonian in the rotating frame is tilted (through the rotation operator ($U_1 = e^{i\frac{\pi}{2}I_y}$)) such that the RF field is quantized along the z-direction.

$$H_{TR} = U_1 H_R(t) U_1^{-1} = \omega_1 I_z - 2\omega' \cos(2\omega_r t)\, I_x \tag{2.24}$$

1.1 Description based on Effective Floquet Hamiltonians

In the Floquet framework, the time-dependent Hamiltonian defined in a finite dimensional vector space is transformed into a time-independent Hamiltonian via Fourier expansion [45–51]. Employing an operator basis defined in an infinite dimensional vector space (extended Hilbert space or Floquet space), the Hamiltonian in the tilted rotating frame (for on-resonance case) is re-expressed as follows-

$$H_F = \omega_r I_F + \omega_1 [I_z]_0 - \sum_{m=\pm 2} \omega^{(m)} [I_x]_m \tag{2.25}$$

A schematic description of the Floquet Hamiltonian for a single spin system is defined in an extended (infinite dimensional) Hilbert space is given below.

$$H_F = \left[\begin{array}{c|cccccc|c}
 & |\alpha,2\rangle & |\beta,2\rangle & |\alpha,0\rangle & |\beta,0\rangle & |\alpha,-2\rangle & |\beta,-2\rangle & \\
\hline
 & \ddots & & & & & & \iddots \\
\langle\alpha,2| & 2\omega_r+\omega_1/2 & 0 & 0 & \omega^{(2)} & 0 & 0 & \\
\langle\beta,2| & 0 & \multicolumn{2}{c}{\multirow{2}{*}{$\begin{pmatrix} 2\omega_r-\omega_1/2 & \omega^{(2)} \\ \omega^{(-2)} & \omega_1/2 \end{pmatrix}$}} & 0 & 0 & 0 & \\
\langle\alpha,0| & 0 & & & 0 & 0 & \omega^{(2)} & \\
\langle\beta,0| & \omega^{(-2)} & 0 & 0 & \multicolumn{2}{c}{\multirow{2}{*}{$\begin{pmatrix} -\omega_1/2 & \omega^{(2)} \\ \omega^{(-2)} & -2\omega_r+\omega_1/2 \end{pmatrix}$}} & 0 & \\
\langle\alpha,-2| & 0 & 0 & 0 & & & 0 & \\
\langle\beta,-2| & 0 & 0 & \omega^{(-2)} & 0 & 0 & -2\omega_r-\omega_1/2 & \\
 & \iddots & & & & & & \ddots
\end{array}\right]$$

Figure 2.4: Matrix representation of the Floquet Hamiltonian for a spin-1/2 system defined in the Floquet space.

In the extended Hilbert space (or Floquet space), the spin states $|\alpha\rangle$ and $|\beta\rangle$ are dressed with Fourier index n ('n' ranges from $-\infty$ to ∞). In the present context, the off-diagonal terms $\omega^{(2)}, \omega^{(-2)}$ are real and equal to ω' ($\omega^{(2)} = \omega^{(-2)} = \omega'$). As depicted in Figure 2.4, in the Floquet description, the states $|\alpha 0\rangle$ and $|\beta 2\rangle$ (likewise the states $|\alpha - 2\rangle$ and $|\beta 0\rangle$) are connected by the element ω' ($\omega^{(2)} = \omega^{(-2)} = \omega'$). From an operational aspect, the relevance of the off-diagonal elements in perturbative methods depends on the difference between the energy eigenvalues of the two states involved in the description. In the present context, the energy difference corresponding to the pair of states ($|\alpha 0\rangle \rightarrow |\beta 2\rangle$, $|\alpha - 2\rangle \rightarrow |\beta 0\rangle$) is given by $\Delta E = |2\omega_r - \omega_1|$. When the energy difference ΔE is greater than or equal to $8\omega'$, the ideal pulse approximation (strong pulse limit) becomes operational in MAS experiments. In all other cases ($\Delta E < 8\omega'$), the contribution from the off-diagonal term becomes relevant in the time evolution of the system. To account for the off-diagonal contributions in the Floquet Hamiltonian, we employ operator based perturbation methods [41–43]. The derivation of effective Floquet Hamiltonians for variety of problems is well-documented [49,53–56] and would only be discussed briefly in the present context.

In the effective Floquet Hamiltonian approach, the Floquet Hamiltonian (Eq. 2.25) is split into a zero-order (H_0) and perturbing Hamiltonian (H_1).

$$H_0 = \omega_r I_F + \omega_1 [I_z]_0 \tag{2.26}$$

$$H_1 = \sum_m G_x^{(m)} [I_x]_m \;\; ; \;\; G_x^{(m)} = -\omega^{(m)} \tag{2.27}$$

From an operational perspective, the choice of the zero-order Hamiltonian plays an important role in the convergence of the effective Hamiltonian and has been discussed extensively in the literature [49,53–56]. Employing the transformation function, S_1, the Floquet Hamiltonian is transformed as given below.

$$H_F^{eff} = e^{i\lambda S_1} H_F e^{-i\lambda S_1} \;\; ; \;\; S_1 = i\left(\sum_m C_x^{(m)} [I_x]_m + \sum_m C_y^{(m)} [I_y]_m\right) \tag{2.28}$$

The coefficients $C_x^{(m)}$ and $C_y^{(m)}$ employed in 'S_1' are chosen to compensate the off-diagonal terms in H_1 and are derived through the relation,

$$-H_1 = i\,[S_1, H_0] \tag{2.29}$$

To second order, the effective Hamiltonian describing the excitation is given by the following equation.

$$H_{F,eff} = H_0 + H_2^{(1)} = \omega_r I_F + \omega_e [I_z]_0 = \omega_r I_F + \omega_1 \left(1 - \frac{1}{2}\sum_m \frac{G_x^{(m)} G_x^{(-m)}}{(m\omega_r)^2 - \omega_1^2}\right) [I_z]_0 \tag{2.30}$$

operators	Initial Density Operator, $A_\alpha^{(m)}$	Detection Operator, $D_\alpha^{(m)}$	Density Operator, $R_\alpha^{(m)}(t)$
$[I_x]_0$	$\cos x$	0	$-\cos x \cos(\omega_e t)$
$[I_y]_0$	0	$\cos y$	$-\cos x \sin(\omega_e t)$
$[I_z]_0$	0	0	0
$[I_z]_2$	$-iC_y^{(2)}$	$-iC_x^{(2)}$	$-iC_y^{(2)}e^{-2i\omega_r t}$
$[I_z]_{-2}$	$-iC_y^{(-2)}$	$-iC_x^{(-2)}$	$-iC_y^{(-2)}e^{2i\omega_r t}$
x	$\sqrt{\sum_p \frac{\omega_1^2\omega^{(p)}\omega^{(-p)}}{(p^2\omega_r^2-\omega_1^2)^2}}$	y	$\sqrt{\sum_p \frac{p^2\omega_r^2\omega^{(p)}\omega^{(-p)}}{(p^2\omega_r^2-\omega_1^2)^2}}$
$C_x^{(m)}$	$\frac{-m\omega_r G_x^{(m)}}{(m\omega_r)^2-\omega_1^2}$	$C_y^{(m)}$	$\frac{i\omega_1 G_x^{(m)}}{(m\omega_r)^2-\omega_1^2}$

Table 2.1: Definition of constants employed in the description of the density operator and detection operator (Eq. 2.31-2.33) based on the contact transformation method.

To have a consistent description, the operators (initial density operator ($\rho_F(0)$) and detection operator (D_F)) are transformed by the same unitary transformation (i.e. $e^{i\lambda S_1}$). In the present calculation, the initial density operator, $\rho_F(0) = [I_z]_0$ and detection operator, $D_F = [I_y]_0$ is employed.

$$\rho'_F(0) = e^{i\lambda S_1} U_1 \rho_F(0) U_1^{-1} e^{-i\lambda S_1} = \sum_m A_\alpha^{(m)} [I_\alpha]_m \quad ; \quad \alpha \in (x, y, z) \tag{2.31}$$

$$D'_F = e^{i\lambda S_1} U_1 D_F U_1^{-1} e^{-i\lambda S_1} = \sum_m D_\alpha^{(m)} [I_\alpha]_m \quad ; \quad \alpha \in (x, y, z) \tag{2.32}$$

Subsequently, employing the effective Floquet Hamiltonian (Eq. 2.30), the density operator at time 't' is evaluated as given below.

$$\rho'_F(t) = e^{-iH_{eff}t} \rho'_F(0) e^{iH_{eff}t} = \sum_m R_\alpha^{(m)}(t) [I_\alpha]_m \tag{2.33}$$

Accordingly, the excitation during a RF pulse in the Floquet space is calculated by the following equation.

$$S(t) = Tr\left[{\rho'}_F(t) D'_F\right] = \sum_m R_\alpha^{(m)}(t) D_\alpha^{(-m)} \tag{2.34}$$

A detailed description of the coefficients employed in the derivation of ${\rho'}_F(0)$, D'_F and ${\rho'}_F(t)$ are tabulated in Table 2.1.

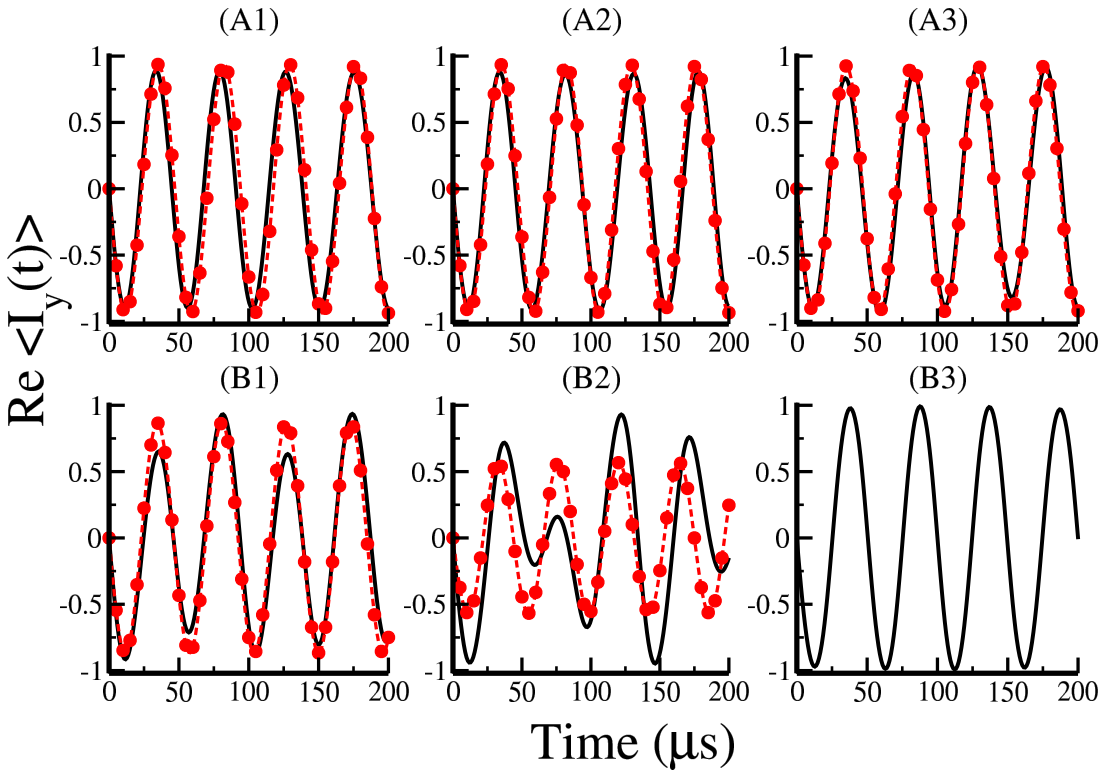

Figure 2.5: In the simulations depicted, the validity of the effective Floquet Hamiltonians is probed for a given pulse amplitude by varying the sample spinning frequency. The analytic simulations based on effective Floquet Hamiltonians (Eq. 2.34) are indicated by red dotted lines, while, those based on SPINEVOLUTION [7] are indicated by black solid lines. The following parameters were used in the simulations: (A1) $\omega_r = (1/8)\omega'$ [0.266] (A2) $\omega_r = (1/4)\omega'$ [0.286] (A3) $\omega_r = (1/2)\omega'$ [0.333] (B1) $\omega_r = \omega'$ [0.5] (B2) $\omega_r = (3/2)\omega'$ [1.0] (B3) $\omega_r = 2\omega'$ [∞]. In the simulations depicted, the RF amplitude is greater than the magnitude of the internal interaction (i.e. $\omega_1 = 4\omega'$). Due to the resonance condition ($\omega_1 - 2\omega_r = 0$), the analytic simulations corresponding to the parameters depicted in the panel B3 could not be performed ($\omega_1 = 4\omega', \omega_r = 2\omega'$). The numbers given in the square brackets in the panels correspond to the ratio $[\omega'/(|2\omega_r - \omega_1|)]$.

To verify the validity of the above analytic framework, the analytic simulations depicted

in Figures 2.5 and 2.6 are examined with numerical simulations. As depicted in Figure 2.5, the analytic simulations match well with numerical simulations except for the simulations in panels B2 and B3. From an operational perspective, this discrepancy results from the larger magnitude of the off-diagonal term with respect to the energy difference, ΔE ($2\omega_r - \omega_1$ is approximately equal to $\omega^{(2)}$). Under such conditions (the concept of perturbation remains invalid), the corrections derived from perturbation theory are insufficient to describe the spin dynamics. Interestingly, the discrepancies get magnified near the resonance conditions (i.e. when $\omega_1 = 2\omega_r$ (refer to Figure 2.5, panel B3) the corrections tend to infinity), necessitating descriptions based on degenerate perturbation theory. Such resonance conditions are also observed in the simulations depicted in Figure 2.6 (Panel A1).

Based on the simulations depicted in Figures 2.5 and 2.6, the perturbation corrections converge only in cases where the ratio $|\frac{\omega'}{2\omega_r - \omega_1}|$ is less than or equal to 0.5. Additionally, as illustrated in Figure 2.5 (Panel B3) and Figure 2.6 (Panel A1), the present method is of lesser utility near resonance conditions (as the C-coefficients employed in the transformation function tend to infinity). To improve the exactness of the method beyond the predicted perturbation limit and near resonance conditions as well, an alternate method is proposed in the following subsection.

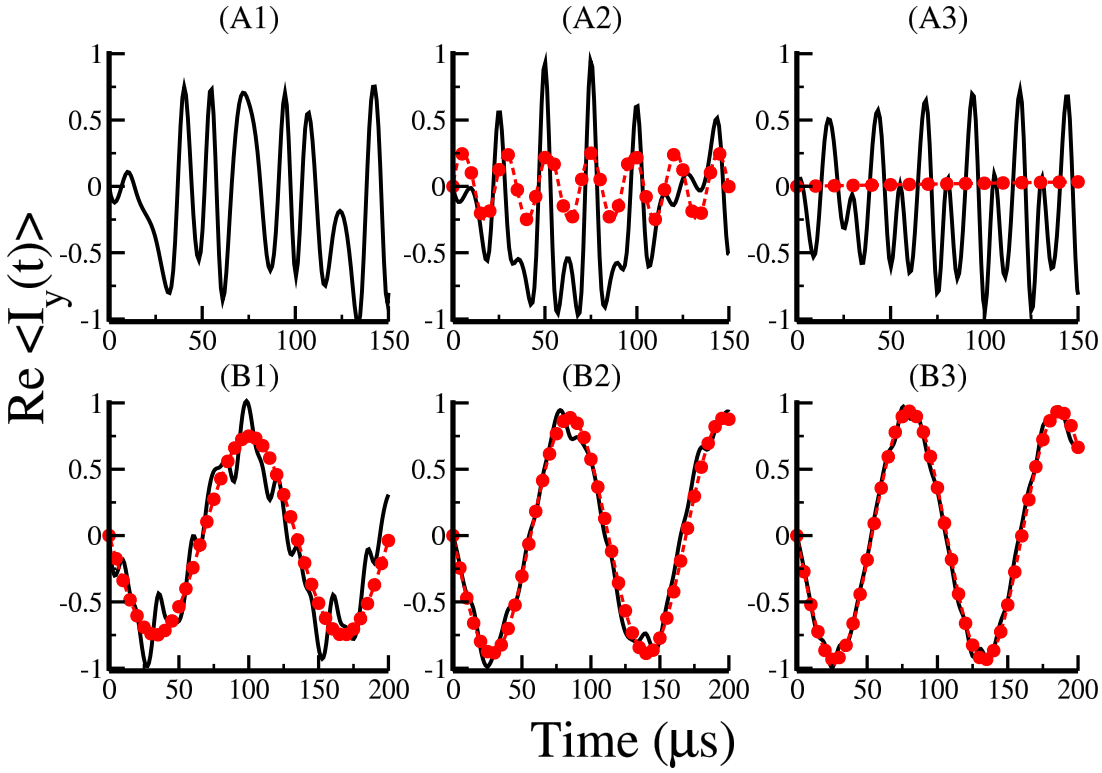

Figure 2.6: In the simulations depicted, the validity of the effective Floquet Hamiltonians is probed for a given pulse amplitude by varying the sample spinning frequency. The analytic simulations based on effective Floquet Hamiltonians (Eq. 2.34) are indicated by red dotted lines, while, those based on SPINEVOLUTION [7] are indicated by black solid lines. The following parameters were used in the simulations: (A1) $\omega_r = (1/8)\omega'$ [∞] (A2) $\omega_r = (1/4)\omega'$ [4.0] (A3) $\omega_r = (1/2)\omega'$ [1.3] (B1) $\omega_r = \omega'$ [0.57] (B2) $\omega_r = (3/2)\omega'$ [0.36] (B3) $\omega_r = 2\omega'$ [0.266]. In the simulations depicted, the RF amplitude is lower than the magnitude of the internal interaction (i.e. $\omega_1 = (1/4)\omega'$). Due to the resonance condition ($\omega_1 - 2\omega_r = 0$), the analytic simulations corresponding to the parameters depicted in the panel A1 could not be performed ($\omega_1 = (1/4)\omega', \omega_r = (1/8)\omega'$). The numbers given in the square brackets in the panels correspond to the ratio $[\omega'/(|2\omega_r - \omega_1|)]$.

2. Description of finite pulse effects in Fictitious frame

To tackle the convergence problem discussed in the previous section (encountered in the intermediate regimes), the Hamiltonian in the tilted rotating frame is further transformed into a frame defined by the modulation frequency ($2\omega_r$ in this case). Employing the transformation function, U_2 ($U_2 = e^{2i\omega_r t I_z}$), the Hamiltonian in the tilted rotating frame (Eq. 2.24) is

transformed as given below.

$$\widetilde{H}_{TR}(t) = U_2 H_{TR}(t) U_2^{-1} = (\omega_1 - 2\omega_r)\, I_z - \sum_m \omega^{(m)} e^{im\omega_r t} \left(I_x \cos(2\omega_r t) - I_y \sin(2\omega_r t)\right) \tag{2.35}$$

To simplify the description, the static part of the Hamiltonian in the fictitious frame is quantized along the z-direction through the rotation operator, U_3 ($U_3 = e^{i\theta I_y}$, $\theta = \tan^{-1}(\frac{-\omega^{(2)}}{\omega_1 - 2\omega_r})$). Accordingly, the final form of the Hamiltonian in the fictitious frame is derived and represented below.

$$\widetilde{\widetilde{H}}_{TR}(t) = \omega_{eff} I_z + \omega^{(2)} \sin(4\omega_r t)\, I_y - \omega^{(2)} \cos\theta \cos(4\omega_r t)\, I_x - \omega^{(2)} \sin\theta \cos(4\omega_r t)\, I_z \tag{2.36}$$

In the above equation, ω_{eff} ($\omega_{eff} = (\omega_1 - 2\omega_r)\cos\theta - \omega^{(2)} \sin\theta$) represents the effective field along the z-direction.

From an operational standpoint, the dominant contributions from the time-dependent part get minimized in the fictitious frame and are essential to facilitate faster convergence of the perturbations corrections. Subsequently, the above time-dependent Hamiltonian is transformed into a time-independent Floquet Hamiltonian as described in the previous subsection.

$$H_F = \omega_r I_F + \omega_{eff}[I_z]_0 + \sum_{p=\pm 4} G_\alpha^{(p)} [I_\alpha]_p \quad ; \quad \alpha \in (x, y, z) \tag{2.37}$$

In contrast to the description in the preceding subsection, the Floquet Hamiltonian (in the fictitious frame) has terms (off-diagonal) along all the three-directions. Following the procedure described in the previous subsection, the Floquet Hamiltonian is transformed using the contact transformation procedure.

$$H_F^{eff} = e^{i\lambda S_1} H_F e^{-i\lambda S_1}$$

where,

$$H_0 = \omega_r I_F + \omega_{eff}[I_z]_0 \;\; ; \;\; H_1 = \sum_{p=\pm 4} G_\alpha^{(p)} [I_\alpha]_p$$

To compensate the off-diagonal contributions, the transformation function, $S_1 = i \sum C_\alpha^{(p)} [I_\alpha]_p$; $\alpha \in (x, y, z)$ is expressed as a linear combination of the three operators (along x, y and z) whose coefficients are obtained by solving linear equations derived from $H_1^{(1)}$ (i.e. $H_1^{(1)} = H_1 + i[S_1, H_0] = 0$).

To second order, the effective Hamiltonian in the present case is derived and represented as given below.

$$H_{F,eff} = H_0 + H_{2,diagonal}^{(1)} = \omega_r I_F + \omega_e [I_z]_0 \tag{2.38}$$

where

$$\omega_e = \omega_{eff} + \frac{i}{2}\left[\sum_{p=-4,p\neq 0}^{4} C_y^{(p)} G_x^{(-p)} - C_x^{(p)} G_y^{(-p)}\right]$$

To maintain consistency, both the initial density operator ($\rho_F(0) = [I_z]_0$) and the detection operator ($D_F = [I_y]_2 + [I_y]_{-2}$ (this is due to the fictitious frame)) are transformed.

$$\rho'_F(0) = e^{i\lambda S_1} U_1 \rho_F(0) U_1^{-1} e^{-i\lambda S_1} = \sum_m A_\alpha^{(m)} [I_\alpha]_m \;\; ; \;\; \alpha \in (x, y, z) \tag{2.39}$$

$$D'_F = e^{i\lambda S_1} U_1^{-1} I_y U_1^{-1} e^{-i\lambda S_1} = \sum_m D_\alpha^{(m)} [I_\alpha]_m \;\; ; \;\; \alpha \in (x, y, z) \tag{2.40}$$

The density operator during the pulse is calculated using the effective Hamiltonian given in Eq. 2.38.

$$\rho'_F(t) = e^{-iH_{eff}t} \rho'_F(0) e^{iH_{eff}t} = \sum_m R_\alpha^{(m)}(t) [I_\alpha]_m \tag{2.41}$$

A detailed description of the coefficients is given in Table 2.2. Following the procedure given in the previous section, the excitation during the pulse is evaluated.

$$S(t) = Tr\left[\rho'_F(t) D'_F\right] = \sum_m R_\alpha^{(m)}(t) D_\alpha^{(-m)} \tag{2.42}$$

To test the validity of the proposed framework, the discrepancies observed in the simulations based on the contact transformation method are re-examined using the description in the fictitious frame. In the simulations depicted in Figure 2.7, the perturbation limit is explored over wide range of parameters, $0 < |\frac{\omega'}{2\omega_r - \omega_1}| < 1$. In the first row (panels A1-A4), analytic simulations based on the fictitious frame (Eq. 2.42) is depicted, while, the simulations in the second row correspond to those based on the contact transformation (Eq. 2.34).

operators	Initial Density Operator, $A_\alpha^{(m)}$	Detection Operator, $D_\alpha^{(m)}$	Density Operator, $R_\alpha^{(m)}(t)$
$[I_x]_2$	$-\frac{\cos\theta\cos a}{2}$	$-\frac{i\cos\theta\cos a}{2}$	$\frac{e^{-2i\omega_r t}}{2}(-\cos\theta\cos a\cos(\omega_e t)\ +i\cos b\sin(\omega_e t))$
$[I_x]_{-2}$	$-\frac{\cos\theta\cos a}{2}$	$\frac{i\cos\theta\cos a}{2}$	$\frac{e^{2i\omega_r t}}{2}(-\cos\theta\cos a\cos(\omega_e t)\ -i\cos b\sin(\omega_e t))$
$[I_y]_2$	$-\frac{i\cos b}{2}$	$\frac{\cos b}{2}$	$\frac{e^{-2i\omega_r t}}{2}(-\cos\theta\cos a\sin(\omega_e t)\ -i\cos b\cos(\omega_e t))$
$[I_y]_{-2}$	$\frac{i\cos b}{2}$	$\frac{\cos b}{2}$	$\frac{e^{2i\omega_r t}}{2}(-\cos\theta\cos a\sin(\omega_e t)\ +i\cos b\cos(\omega_e t))$
$[I_z]_2$	$-\frac{\sin\theta\cos c}{2}$	$-\frac{i\sin\theta\cos c}{2}$	$-\frac{\sin\theta\cos c}{2}e^{-2i\omega_r t}$
$[I_z]_{-2}$	$-\frac{\sin\theta\cos c}{2}$	$\frac{i\sin\theta\cos c}{2}$	$-\frac{\sin\theta\cos c}{2}e^{2i\omega_r t}$
a^2	$-(\sum_m C_y^{(m)}C_y^{(-m)} + C_z^{(m)}C_z^{(-m)})$	b^2	$-(\sum_m C_x^{(m)}C_x^{(-m)} + C_z^{(m)}C_z^{(-m)})$
c^2	$-(\sum_m C_x^{(m)}C_x^{(-m)} + C_y^{(m)}C_y^{(-m)})$	$C_z^{(p)}$	$-\frac{G_z^{(p)}}{p\omega_r}$
$C_x^{(p)}$	$-\frac{p\omega_r G_x^{(p)} + i\omega_{eff}G_y^{(p)}}{(p\omega_r)^2-\omega_{eff}^2}$	$C_y^{(p)}$	$\frac{-p\omega_r G_y^{(p)} + i\omega_{eff}G_x^{(p)}}{(p\omega_r)^2-\omega_{eff}^2}$

Table 2.2: Definition of constants employed in the description of the density operator and detection operator (Eq. 2.39-2.41) based on the fictitious frame method.

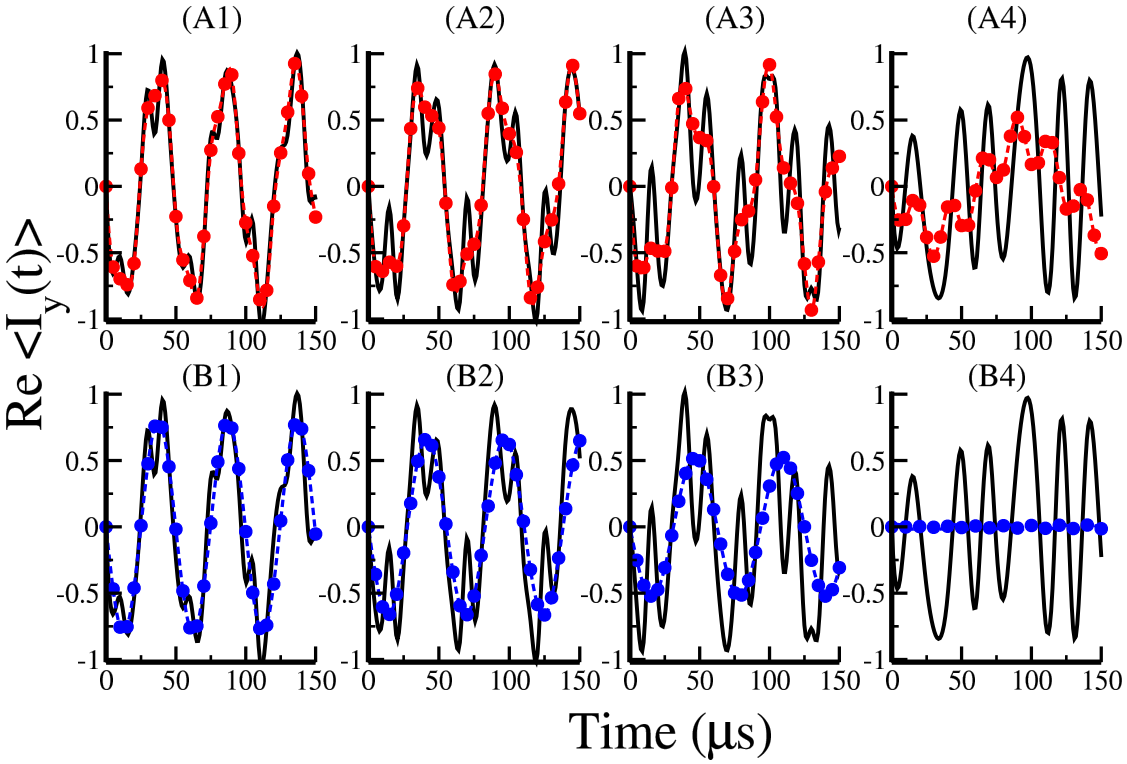

Figure 2.7: In the simulations depicted, the validity of the calculations based on the fictitious frame is probed for a given pulse amplitude by varying the sample spinning frequency. For illustrative purposes, the analytic simulations based on the fictitious frame (first row, panels A1-A4, indicated by red dots based on Eq. 2.42) and effective Floquet Hamiltonians (second row, panels B1-B4, indicated by blue dots based on Eq. 2.34) are compared with those based on SPINEVOLUTION [7] (indicated by black solid lines). The following parameters were used in the simulations: (A1,B1) $\omega_r = (4/3)\omega'$ [0.6] (A2,B2) $\omega_r = (9/8)\omega'$ [0.8] (A3,B3) $\omega_r = \omega'$ [1.0] (A4,B4) $\omega_r = (1/6)\omega'$ [1.5]. In the simulations depicted, the RF amplitude is equal to the magnitude of the internal interaction (i.e. $\omega_1 = \omega'$). The numbers given in the square brackets in the panels correspond to the ratio $[\omega'/(|2\omega_r - \omega_1|)]$.

As depicted, the analytic simulations based on the fictitious frame approach (indicated in red) are in better agreement (for cases where, $0 < |\frac{\omega'}{2\omega_r - \omega_1}| < 1$) to those obtained from the contact transformation approach (indicated in blue). In cases where the ratio ($|\frac{\omega'}{2\omega_r - \omega_1}|$) exceeds 1, significant deviations are observed in the analytic simulations based on the fictitious frame approach. To improve the exactness of the analytic simulations, an alternate approach is explored in the following subsection.

2. Strong Coupling Regime

When the magnitude of the CSA interactions exceeds both the amplitude of the pulse and the spinning frequency employed, the Hamiltonian in the rotating frame (Eq. 2.23) is transformed into a time-dependent interaction frame defined by the CSA interaction (or CSA interaction frame). In the initial treatment proposed by Ernst and co-workers, this time-dependent transformation was referred to as the jolting frame transformation [36,37,57,58].

$$\begin{aligned}\widetilde{H} &= e^{i\Phi(t)I_z} H_R(t)\, e^{-i\Phi(t)I_z} \\ &= \omega_1 \left[e^{i\Phi(t)I_z} I_x e^{-i\Phi(t)I_z}\right], \quad \Phi(t) = 2\omega' \int_0^t \cos(2\omega_r t')dt'\end{aligned} \tag{2.43}$$

In the interaction frame, the RF Hamiltonian is time-dependent and has a complicated form.

$$\widetilde{H} = \frac{\omega_1}{2}\left[e^{i\Phi(t)} I_+ + e^{-i\Phi(t)} I_-\right] \tag{2.44}$$

Employing Bessel functions (of first kind) [59], the coefficients in the above Hamiltonian is evaluated and expressed in a compact form.

$$\widetilde{H}(t) = \omega_1 J_0\left(\frac{\omega'}{\omega_r}\right) I_x + \omega_1 \sum_{k=\pm4,\pm8,..} J_{k/2}\left(\frac{\omega'}{\omega_r}\right) e^{ik\omega_r t} I_x + i\omega_1 \sum_{m=\pm2,\pm6,..} J_{m/2}\left(\frac{\omega'}{\omega_r}\right) e^{im\omega_r t} I_y \tag{2.45}$$

Ignoring the time-dependent terms, the effective Hamiltonian is approximated by the following equation.

$$H_{eff} = \omega_1 J_0\left(\frac{\omega'}{\omega_r}\right) I_x \tag{2.46}$$

To maintain consistency, both the initial density operator and detection operator are transformed as given below.

$$\tilde{\rho}(0) = \rho(0) = I_z \tag{2.47}$$

$$\begin{aligned}\tilde{I}_y &= e^{i\Phi(t)I_z} I_y e^{-i\Phi(t)I_z} \\ &= \left[J_0\left(\tfrac{\omega'}{\omega_r}\right) + \sum_{n=2p} 2J_n\left(\tfrac{\omega'}{\omega_r}\right)\cos(2n\omega_r t)\right] I_y + \left[\sum_{n=2p-1} 2J_n\left(\tfrac{\omega'}{\omega_r}\right)\sin(2n\omega_r t)\right] I_x\end{aligned} \tag{2.48}$$

Subsequently, the excitation during the pulse is described by the following equation.

$$\begin{aligned}\langle I_y(t)\rangle &= Tr\left[\tilde{\rho}(t)\tilde{I}_y\right] = Tr\left[e^{-iH_{eff}t}\tilde{\rho}(0)e^{iH_{eff}t}\tilde{I}_y\right] \\ &= -\left[J_0\left(\tfrac{\omega'}{\omega_r}\right) + \sum_{n=2p} 2J_n\left(\tfrac{\omega'}{\omega_r}\right)\cos(2n\omega_r t)\right]\sin\left(\omega_1 t J_0\left(\tfrac{\omega'}{\omega_r}\right)\right)\end{aligned} \tag{2.49}$$

where $p \in \mathbb{N}$ (Natural numbers, e.g. 1,2,3,....).

To verify the exactness of the above calculations, analytic simulations based on the Bessel functions are compared with those obtained from SPINEVOLUTION [7]. In the simulations

depicted in Figure 2.8, the role of the order (indicated by 'n') employed in the Bessel functions ($J_n(x)$) is investigated for a given set of parameters ($\omega' = 6\omega_r$, $\omega_1 = \omega_r$).

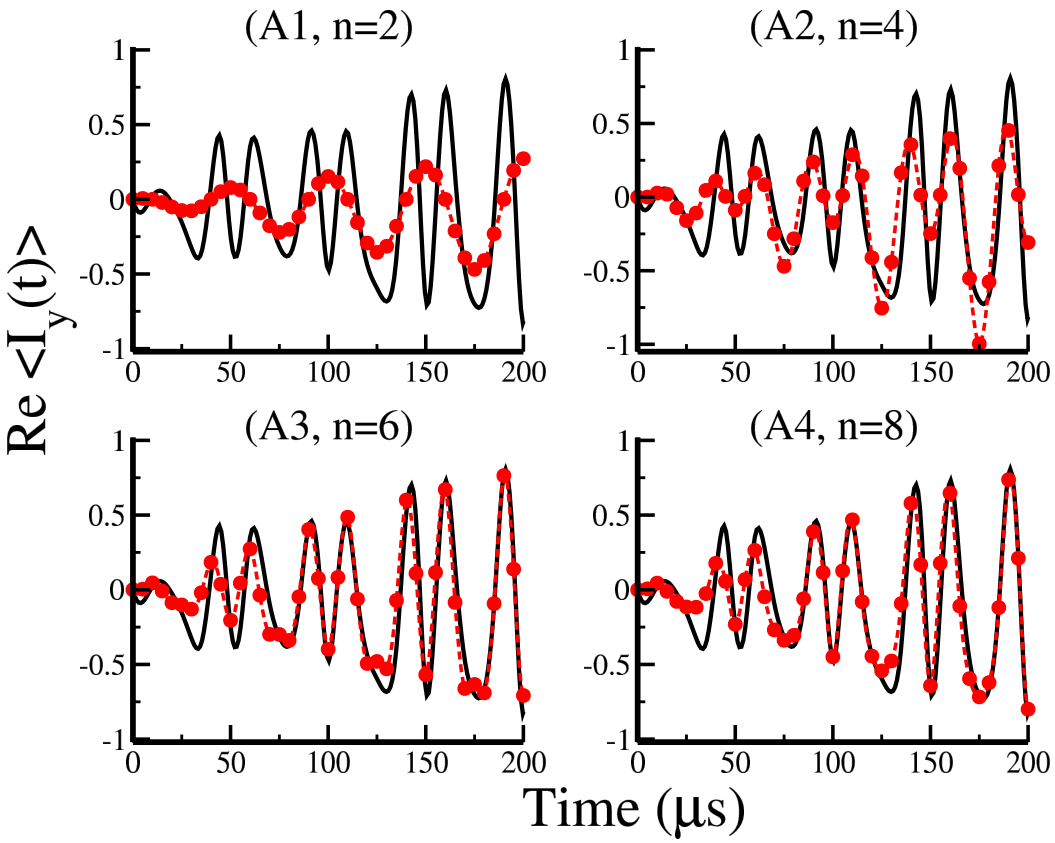

Figure 2.8: In the simulations depicted, the relevance of the order 'n' employed in Bessel functions ($J_n(x)$) is examined for a given set of parameters (i.e. $\omega'/\omega_r = 6, \omega_1 = \omega_r$). The order 'n' is varied in the panels: (A1) n=2 (A2) n=4 (A3) n=6 (A4) n=8. The numerical simulations based on SPINEVOLUTION [7] are indicated by solid black lines.

As depicted in the simulations, the choice of the order 'n' employed in the Bessel functions plays an important role in the analytic simulations and is dependent on the ratio of the magnitude of the CSA interaction to the spinning frequency (i.e. $\omega'/\omega_r = n$). The exactness of the analytic simulations improves when the order 'n' is chosen according to the above ratio (in the present context, n=6). To explicate the role (if any) of the amplitude of the pulse in the above calculations, analytic simulations with differing amplitudes were compared for a given ω' and ω_r (i.e. $\omega'/\omega_r = 6$). As illustrated in the simulations depicted in Figure 2.9, when the amplitude of the pulse exceeds the modulation frequency (i.e. $\omega_{mod}/\omega_1 < 1.0$, where $\omega_{mod} = 2\omega_r$) employed, significant deviations are observed (refer to panels A3, A4 in

Figure 2.9) in the analytic simulations. While the above scenario is less prevalent in the study of spin I=1/2 systems (as the RF amplitude often exceeds the magnitude of the CSA interactions, $\omega_1 > \omega'$), such cases are frequently encountered in the description of finite pulse effects in the study of quadrupolar spins.

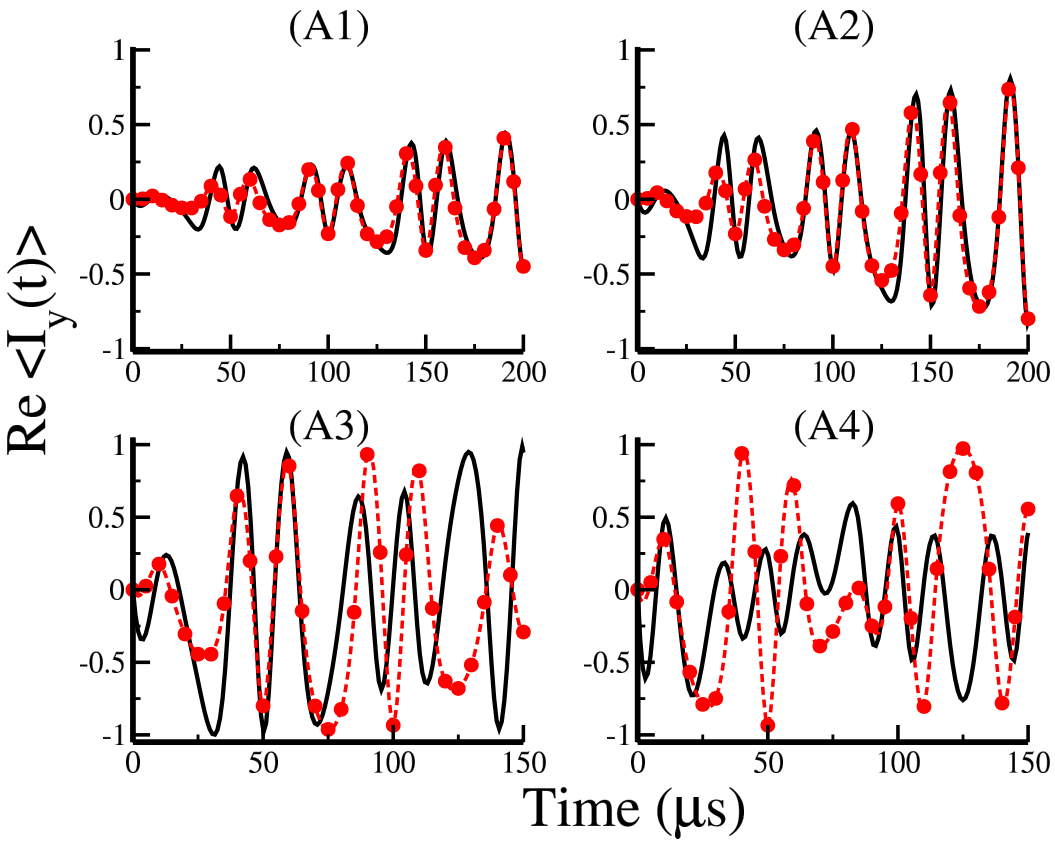

Figure 2.9: In the simulations depicted, the role of RF amplitude in the analytic simulations is examined for a given set of parameters ($\omega' = 6\omega_r$). The ratio of ω_{mod}/ω_1 is varied as- (A1) 4.0 (A2) 2.0 (A3) 0.5 (A4) 0.25. The numerical simulations based on SPINEVOLUTION [7] are indicated by solid black lines.

To understand the combined role of the various parameters in the excitation process, additional simulations were carried out in the present study. In the simulations illustrated in Figure 2.10, the variation of the RF amplitude with respect to the magnitude of the CSA interaction is depicted along the rows (first row, $\omega_1 = (1/4)\omega'$, second row, $\omega_1 = \omega'$, third row, $\omega_1 = 4\omega'$), while, the effect of the sample spinning frequency (ω_r) with respect to the magnitude of the CSA interactions (ω') is depicted along the columns.

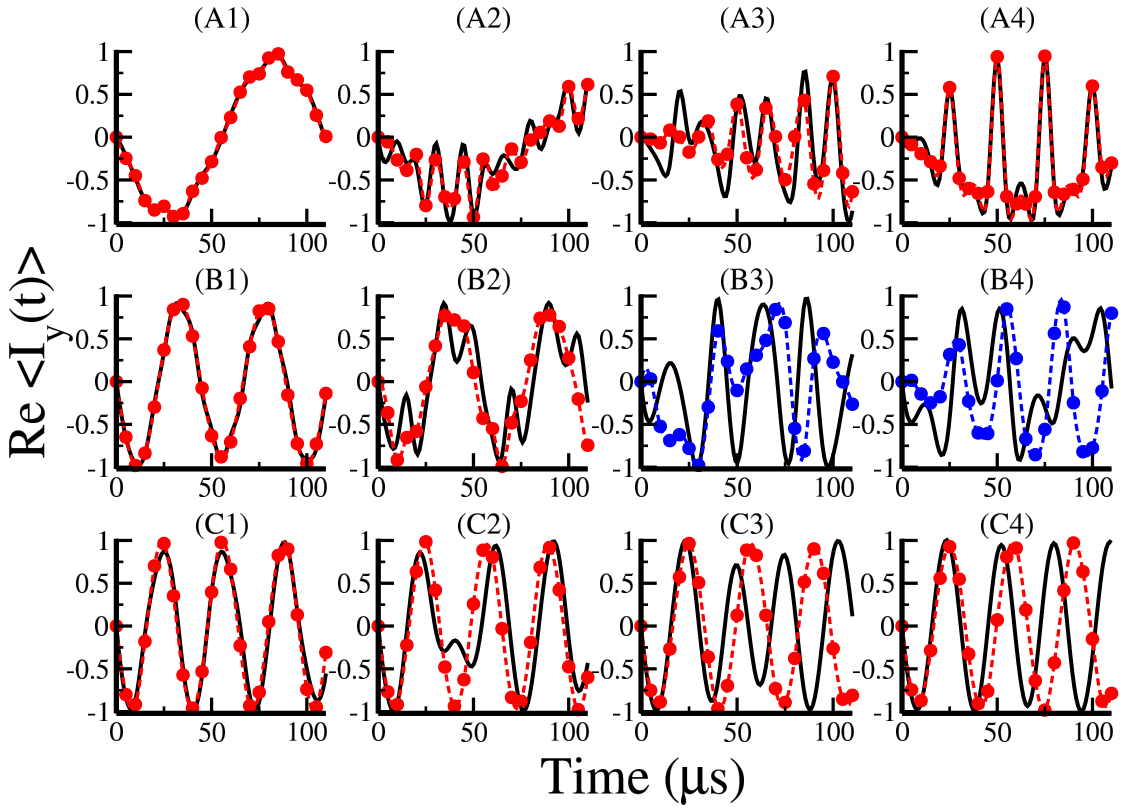

Figure 2.10: In the simulations depicted, the validity of Bessel function calculations is verified. The following parameters were used in the simulations: (A1) $\omega_r = (13/8)\omega'$ [0.33] (A2) $\omega_r = (6/8)\omega'$ [0.8] (A3) $\omega_r = (3/8)\omega'$ [2.0] (A4) $\omega_r = (1/4)\omega'$ [4.0] (B1) $\omega_r = 2\omega'$ [0.33] (B2) $\omega_r = (9/8)\omega'$ [0.8] (B3) $\omega_r = (1/4)\omega'$ [2.0] (B4) $\omega_r = (3/8)\omega'$ [4.0] (C1) $\omega_r = (7/2)\omega'$ [0.33] (C2) $\omega_r = (21/8)\omega'$ [0.8] (C3) $\omega_r = (18/8)\omega'$ [2.0] (C4) $\omega_r = (17/8)\omega'$ [4.0]. In the simulations depicted, the RF amplitude is varied as $\omega_1 = (1/4)\omega'$ for panels A1-A4, $\omega_1 = \omega'$ for panels B1-B4 and $\omega_1 = 4\omega'$ for panels C1-C4. The numbers given in the square brackets in the panels correspond to $[\omega'/(|2\omega_r - \omega_1|)]$. The numerical simulations based on SPINEVOLUTION [7] are indicated by solid black lines.

As illustrated, the Bessel function approach works well only when the amplitude of the pulse is lower than both the magnitude of the CSA interactions as well as the modulation frequency ($2\omega_r$) (first row). When the RF amplitude exceeds the magnitude of the CSA interaction ($\omega_1 > \omega'$, third row), the transformation into the CSA interaction frame yields inexact results. Hence, the suitability of analytic methods depends on the magnitudes of both the internal and external parameters in addition to the transformations employed in the derivation of effective Hamiltonians.

3. Description of finite pulse effects near resonance conditions

As described in the weak coupling regime, the analytic simulations based on the concept of effective Hamiltonians become invalid near the resonance conditions ($\omega_1 = 2\omega_r$). This is primarily due to the divergence of the 'C' coefficients ($C_x^{(2)}=\frac{-2\omega_r G_x^{(2)}}{(2\omega_r)^2-\omega_1^2}$, $C_y^{(2)}=\frac{i\omega_1 G_x^{(2)}}{(2\omega_r)^2-\omega_1^2}$) employed in the transformation function, S_1. Below, we present a comparative study of the simulations emerging from the two methods (fictitious frame and Bessel frame calculations in strong coupling regime) near the resonance conditions. In the simulations depicted in Figure 2.11, the exactness of the derived effective Hamiltonians based on the transformation into the fictitious frame and the CSA interaction frame is examined near the resonance conditions ($\omega_1 = 2\omega_r$).

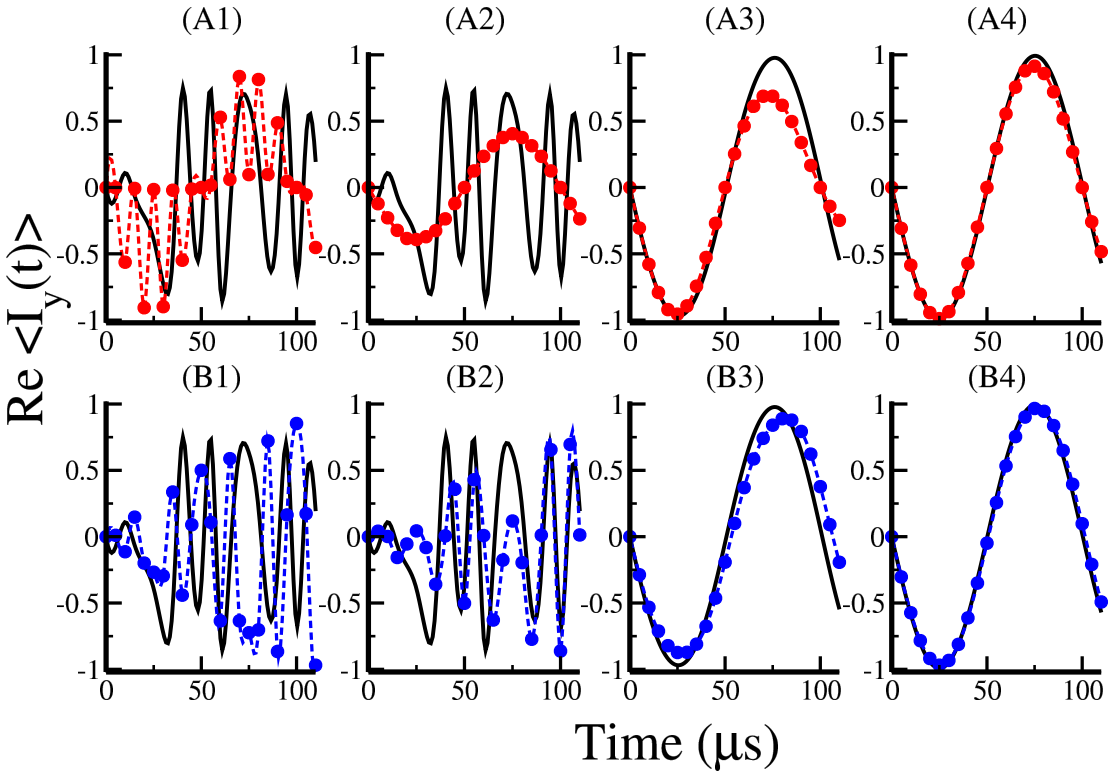

Figure 2.11: In the simulations depicted, the excitation is described at the resonance condition (i.e. $\omega_1 = 2\omega_r$) using analytic methods based on Fictitious frame (first row, panels A1-A4, indicated in red dots based on Eq. 2.42) and the Bessel function approach (second row, panels B1-B4, indicated in blue dots based on Eq. 2.49). The following parameters were used in the simulations: (A1,B1) $\omega_1 = (1/8)\omega'$ (A2,B2) $\omega_1 = (1/4)\omega'$ (A3,B3) $\omega_1 = 4\omega'$ (A4,B4) $\omega_1 = 8\omega'$. The numerical simulations based on SPINEVOLUTION [7] are indicated in solid black lines.

When the amplitude of the pulse is greater than the magnitude of the CSA interaction, analytic simulations based on the transformation into the fictitious frame (refer to first row in Figure 2.11) still yield results in better agreement. However, with increasing magnitude of the CSA interactions, the transformation into the fictitious frame is of lesser utility when compared to the transformation into the CSA interaction frame (refer to second row in Figure 2.11). Hence, the transformations into the time-dependent CSA interaction frame seems to be an attractive option for describing the excitation near the resonance conditions. In the following section, the utility of the analytic methods in the description of excitation in three-level systems is explored.

2.3.2 Finite pulse effects in spin I=1 system

To describe the excitation in a spin-1 system, we consider the Hamiltonian of an isolated system in a rotating solid.

$$H(t) = \underbrace{\omega_0 I_Z}_{H_Z} + \underbrace{2\omega_1 \cos(\omega t)\, I_X}_{H_{RF}} + \underbrace{\sum_{q=-2}^{2} R_{Q,L}^{(2)-q}(t) T^{(2)q}}_{H_Q} \quad ; \quad \hbar = 1 \tag{2.50}$$

In addition to the interactions described in Eq. 2.1, nuclei with I>1/2 possess a non-zero quadrupolar moment that results in the quadrupolar interaction (represented by, H_Q). For the sake of simplicity, the CSA interactions are ignored in the present study. To study the effects of the internal interactions, the Hamiltonian (in Eq. 2.50) is transformed into the rotating frame ($U = e^{i\omega t I_Z}$) such that the RF Hamiltonian reduces to a simpler form as given below.

$$\widetilde{H}(t) = UH(t)U^{-1} = \Delta\omega I_Z + \omega_1 I_X + \sum_{q=-2}^{2} R_{Q,L}^{(2)-q}(t) T^{(2)q} e^{iq\omega t} \tag{2.51}$$

The term $\Delta\omega = \omega_0 - \omega$ represents the offset in the rotating frame.
In the rotating frame, the quadrupolar interaction has additional time-dependence due to 'ω' (frequency of the oscillating field) and is re-expressed in a compact form as given below.

$$H_Q(t) = \frac{1}{\sqrt{6}} \sum_{q=-2}^{2} \sum_{m=-2,\neq 0}^{2} \omega_{Q,m}^{(2)-q} T^{(2)q} e^{iq\omega t} e^{im\omega_r t} \tag{2.52}$$

where

$$\omega_{Q,m}^{(2)q} = \sum_{m_1} R_{Q,PAS}^{(2)m_1} \sum_{m_2} D_{m_1 m_2}(\Omega_{PM})\, D_{m_2 m}(\Omega_{MR})\, d_{m,q}(\beta_{RL})$$

To first-order, the quadrupolar Hamiltonian in the rotating frame is represented by ignoring the time-dependent terms.

$$H_Q^{(1)} = \frac{1}{\sqrt{6}} \sum_{m=-2,\neq 0}^{2} \omega_{Q,m}^{(2)0} T^{(2)0} e^{im\omega_r t} \tag{2.53}$$

Employing averaging methods, the second-order contributions (resulting from time-dependent terms) to the quadrupolar interaction is derived and summarized by the following equation.

$$H_Q^{(2)} = -\frac{1}{12} \sum_{q=\pm 1,\pm 2} \sum_{m=\pm 1,\pm 2} \frac{\omega_{Q,m}^{(2)q} \omega_{Q,-m}^{(2)-q}}{q\omega - m\omega_r} \left[T^{(2)q}, T^{(2)-q}\right] \tag{2.54}$$

In the present context (case of spin I=1), the second-order contributions reduce to a simpler form given below.

$$\begin{aligned} H_Q^{(2)} &= \omega' I_Z \, ; \\ \omega' &= \frac{1}{24} \left[\sum_{m=\pm 1,\pm 2} \frac{\omega_{Q,m}^{(2)1} \omega_{Q,-m}^{(2)-1}}{\omega - m\omega_r} + \frac{\omega_{Q,m}^{(2)-1} \omega_{Q,-m}^{(2)1}}{\omega + m\omega_r} \right] \\ &- \frac{1}{12} \left[\sum_{m=\pm 1,\pm 2} \frac{\omega_{Q,m}^{(2)2} \omega_{Q,-m}^{(2)-2}}{2\omega - m\omega_r} + \frac{\omega_{Q,m}^{(2)-2} \omega_{Q,-m}^{(2)2}}{2\omega + m\omega_r} \right] \end{aligned} \tag{2.55}$$

Subsequently, incorporating the above contributions, the Hamiltonian of the system in the rotating frame is represented by the following equation.

$$\widetilde{H}(t) = (\Delta\omega + \omega') I_Z + \omega_1 I_X + \sum_{m=-2,\neq 0}^{2} \frac{\omega_{Q,m}^{(2)0}}{6} \left[3I_Z^2 - I^2\right] e^{im\omega_r t} \tag{2.56}$$

For operational convenience, the above Hamiltonian is represented in terms of fictitious spin-operators [30,8]. Although, methods based on spherical tensor formalism [60–65] are more general and have been used to describe quadrupolar spins, the fictitious spin-operator formalism affords a simpler (a) description of operators (b) framework for deriving the commutator relations between operators.

$$\widetilde{H}(t) = \sum_{m=-2,\neq 0}^{2} \frac{\omega_{Q,m}^{(2)0}}{3} \left[I_Z^{12} - I_Z^{23}\right] e^{im\omega_r t} + \sqrt{2}\omega_1 \left[I_X^{12} + I_X^{23}\right] + 2\left(\Delta\omega + \omega'\right) I_Z^{13} \tag{2.57}$$

In the above representation, the spin states are represented by $|1\rangle$, $|2\rangle$ and $|3\rangle$ ($|1\rangle$ refers to state with m=+1, $|2\rangle$ refers to state with m=0 and $|3\rangle$ refers to state with m=-1). The operators connecting the states $|i\rangle$ and $|j\rangle$ have the usual definitions ($I_X^{ij} = \frac{1}{2}\left[|i\rangle\langle j| + |j\rangle\langle i|\right]$, $I_Y^{ij} = \frac{1}{2i}\left[|i\rangle\langle j| - |j\rangle\langle i|\right]$, $I_Z^{ij} = \frac{1}{2}\left[|i\rangle\langle i| - |j\rangle\langle j|\right]$).

While the (faster) time dependent contributions from the RF interaction are often neglected in the rotating frame, the presence of the dominant (slow varying) quadrupolar interaction often complicates the description of the excitation process in analytic methods.

To this end, in line with the convergence criterion prescribed in perturbative treatments, the Hamiltonian in the rotating frame is further transformed into an interaction frame defined by the quadrupolar interaction (commonly referred to as quadrupolar interaction frame [60–62]). Such an approach is analogous to the jolting frame transformation employed in the study of spin I=1/2 nuclei in the presence of larger chemical shift anisotropic interactions [36,37,57]. Accordingly, employing the transformation function, $U_1 = e^{i\Phi(t)[I_Z^{12}-I_Z^{23}]}$, the Hamiltonian in the rotating frame (Eq. 2.57) is transformed as given below.

$$\widetilde{\widetilde{H}}(t) = U_1 \widetilde{H}(t) U_1^{-1} = \frac{\omega_1}{\sqrt{2}} \left\{ \left[I_+^{12} + I_-^{32} \right] e^{i\frac{3\Phi(t)}{2}} + \left[I_-^{21} + I_+^{23} \right] e^{-i\frac{3\Phi(t)}{2}} \right\} + 2\left(\Delta\omega + \omega'\right) I_Z^{13} \tag{2.58}$$

To facilitate analytic description, the ladder operators are re-expressed in terms of the corresponding X and Y operators.

$$\widetilde{\widetilde{H}}(t) = \sqrt{2}\omega_1 \cos\left(\frac{3\Phi(t)}{2}\right) \left[I_X^{12} + I_X^{23} \right] - \sqrt{2}\omega_1 \sin\left(\frac{3\Phi(t)}{2}\right) \left[I_Y^{12} - I_Y^{23} \right] + 2\left(\Delta\omega + \omega'\right) I_Z^{13} \tag{2.59}$$

where,

$$\Phi(t) = \sum_{m=-2,\neq 0}^{2} \frac{\omega_{Q,m}^{(2)0}}{3} \left[\frac{e^{im\omega_r t} - 1}{im\omega_r} \right]$$

To outline the methodology and explicate analytic insights, the simplest case of on-resonance irradiation is considered ignoring the contributions from second-order quadrupolar interaction. Further, parameters that correspond to single crystal with specific orientations ($\Omega_{PM} = (0°, 90°, 0°)$, η=1.0) is employed in the present study. Based on the above choice of parameters ($\omega_{Q,+2}^{(2)0} = \omega_{Q,-2}^{(2)0}$ and $\omega_{Q,\pm 1}^{(2)0} = 0$), the form of $\Phi(t)$ reduces to a simple expression $\left(\Phi(t) = \frac{\omega_{Q,2}^{(2)0}}{3\omega_r} \sin\left(2\omega_r t\right) \right)$. Such approximations are employed solely for demonstrative purposes and the description that follows is equally valid for any arbitrary orientation. Employing the properties of the Bessel functions [59] (of first kind), the Hamiltonian (Eq. 2.59) is re-expressed in a compact form as given below.

$$\begin{aligned} \widetilde{\widetilde{H}}(t) = {} & \sqrt{2}\omega_1 J_0\left(A\right) \left[I_X^{12} + I_X^{23} \right] \\ & + \sqrt{2}\omega_1 \left[\sum_{k=\pm 4,\pm 8,..} J_{k/2}\left(A\right) e^{ik\omega_r t} \left[I_X^{12} + I_X^{23} \right] + i \sum_{m=\pm 2,\pm 6,..} J_{m/2}\left(A\right) e^{im\omega_r t} \left[I_Y^{12} - I_Y^{23} \right] \right] \end{aligned} \tag{2.60}$$

where $A = \dfrac{\omega_{Q,2}^{(2)0}}{2\omega_r}$ represents the argument of the Bessel function.

Although, the Hamiltonian in the quadrupolar interaction frame still has time-dependent terms, from an operational perspective, the dominant contributions (from quadrupolar interactions) have completely been removed to facilitate analytic descriptions based on perturbation theory. To this end, methods based on Average Hamiltonian theory (AHT) [5,44] and Floquet theory [45–51] have been used extensively to study the spin dynamics of MAS experiments involving spin I=1/2 nuclei. Nevertheless, the operational aspects and exactness of the analytic methods in studying quadrupolar spins remains less explored. In what follows, the excitation of double-quantum (DQ) transitions in spin-1 system is examined through time-propagators derived from the above analytic methods.

2.3.2.1 Time evolution based on AHT

In the Average Hamiltonian framework proposed by Waugh and co-workers [5,44], the evolution operator is described in terms of a time-averaged Hamiltonian derived through an infinite series expansion involving time-integrals based on the Magnus formula [66], $U(t,0) = e^{-i\bar{H}t}$. When the time-integral in the Magnus formula is evaluated at the cycle time, τ_c, the correction terms to the time-averaged Hamiltonian reduce to a much simpler form given below.

$$\bar{H}^{(1)} = \frac{1}{\tau_c}\int_0^{\tau_c} H(t)\,dt = \sqrt{2}\omega_1 J_0(A)\left[I_X^{12} + I_X^{23}\right] \tag{2.61}$$

$$\bar{H}^{(2)} = \frac{-i}{2\tau_c}\int_0^{\tau_c} dt_2 \int_0^{t_2} \left[H(t_2), H(t_1)\right] dt_1 = -\frac{2\omega_1^2}{\omega_r} J_0(A)\left[\sum_{n=2p-1} \frac{J_n(A)}{n}\right]\left[I_Z^{12} - I_Z^{23} + I_X^{13}\right] \tag{2.62}$$

$$\bar{H} = \bar{H}^{(1)} + \bar{H}^{(2)} = \sqrt{2}\omega_1 J_0(A)\left[I_X^{12} + I_X^{23}\right] - \frac{2\omega_1^2}{\omega_r} J_0(A)\left[\sum_{n=2p-1} \frac{J_n(A)}{n}\right]\left[I_Z^{12} - I_Z^{23} + I_X^{13}\right] \tag{2.63}$$

where $p \in \mathbb{N}$ (Natural numbers, e.g. 1,2,3,....).

As represented above, the time-averaged Hamiltonian, $\bar{H}$, consists of non-commuting set of operators and in its present form is of lesser utility in further calculations. To simplify the description of the excitation process, the time-averaged Hamiltonian is transformed (us-

ing $U_2 = e^{\frac{i\theta[I_Y^{12} - I_Y^{23}]}{\sqrt{2}}}$, $\tan\theta = \frac{\omega_1 J_0(A)}{-\frac{2\omega_1^2 J_0(A)}{\omega_r}\left[\sum_{n=2p-1} \frac{J_n(A)}{n}\right]}$), such that the transformed Hamiltonian comprises set of commuting operators as given below.

$$H_{eff} = U_2 \bar{H} U_2^{-1} = \left\{\omega_1 J_0(A)\sin\theta - \frac{2\omega_1^2}{\omega_r} J_0(A)\left[\sum_{n=2p-1}\frac{J_n(A)}{n}\right]\cos\theta\right\}\left[I_Z^{12} - I_Z^{23} + I_X^{13}\right]$$
$$= \omega_e\left[I_Z^{12} - I_Z^{23} + I_X^{13}\right] \tag{2.64}$$

Following the standard procedure, both the operators (initial density operator $\tilde{\rho}(0) = 2I_Z^{13}$ and detection operator $D = I_+^{13}$) are transformed by the same set of unitary transformations given below.

$$\tilde{\rho}(0) = U_2 U_1 \rho(0) U_1^{-1} U_2^{-1}$$
$$= \left\{2\cos\left(\frac{\theta}{2}\right)\right\}\left[I_Z^{13}\right] + \left\{-\sqrt{2}\sin\left(\frac{\theta}{2}\right)\right\}\left[I_X^{12} - I_X^{23}\right] \tag{2.65}$$

$$\widetilde{D} = U_2 U_1 D U_1^{-1} U_2^{-1}$$
$$= \cos\left(\frac{\theta}{2}\right)\left[I_+^{13}\right] - \frac{1}{\sqrt{2}}\sin\left(\frac{\theta}{2}\right)\left[I_+^{12} + I_+^{23}\right] + \frac{(\cos\theta - 1)}{4}\left[I_Z^{12} - I_Z^{23}\right]$$
$$+ 3\left\{\cos\left(\frac{\theta}{2}\right) - 1\right\}\left[I_X^{13}\right] + \frac{3}{\sqrt{2}}\sin\left(\frac{\theta}{2}\right)\left[I_X^{12} + I_X^{23}\right] \tag{2.66}$$

Subsequently, the density operator during the excitation pulse is evaluated at stroboscopic time-intervals using the time-propagator derived from the AHT framework.

$$\tilde{\rho}(t = n\tau_r) = U(n\tau_r, 0)\,\tilde{\rho}(0) U^{-1}(n\tau_r, 0) = e^{-iH_{eff}n\tau_r}\tilde{\rho}(0)e^{iH_{eff}n\tau_r}$$
$$= 2\cos\left(\frac{\theta}{2}\right)\cos(\omega_e t)\left[I_Z^{13}\right] - 2\cos\left(\frac{\theta}{2}\right)\sin(\omega_e t)\left[I_Y^{13}\right]$$
$$- \frac{1}{\sqrt{2}}\sin\left(\frac{\theta}{2}\right)\left\{\left[I_+^{12}\right]e^{-i\omega_e t} + \left[I_-^{21}\right]e^{i\omega_e t} - \left[I_+^{23}\right]e^{i\omega_e t} - \left[I_-^{32}\right]e^{-i\omega_e t}\right\} \tag{2.67}$$

Employing the transformed detection operator, the final signal (corresponding to the excitation of DQ transition) is derived by evaluating the expectation value of the DQ operator, I_+^{13} as given below,

$$\left\langle I_+^{13}(t = n\tau_r)\right\rangle = Tr\left[\tilde{\rho}(t = n\tau_r).\widetilde{D}\right] = -i\cos(\theta)\sin(\omega_e t) \tag{2.68}$$

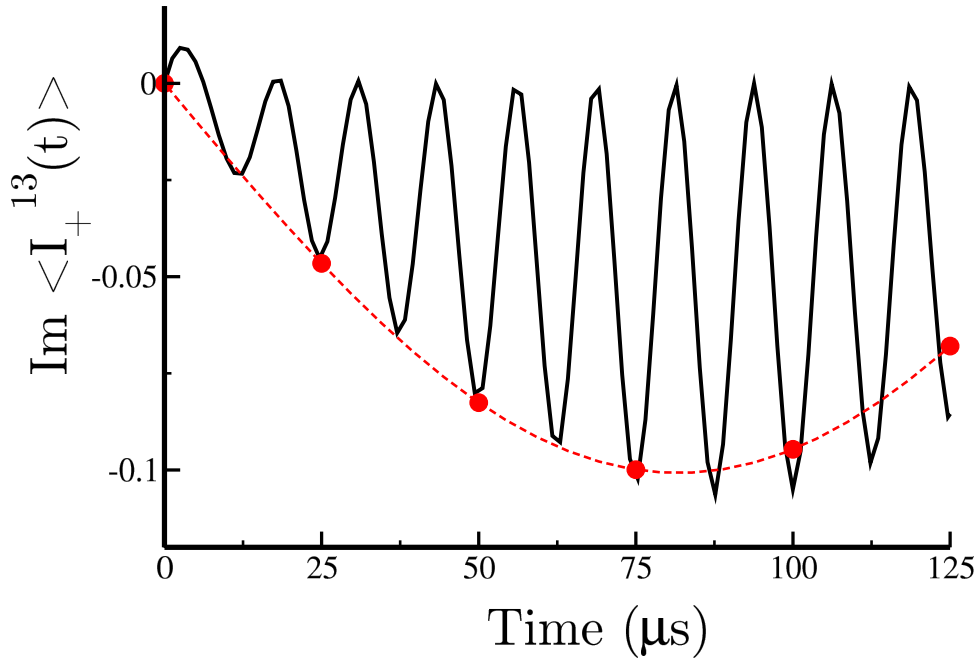

Figure 2.12: In the MAS simulations depicted, excitation of DQ transition in spin I=1 system is presented. The validity of AHT framework (indicated by red dots (based on Eq. 2.68) at stroboscopic time intervals, $\tau_r = 25$ μs) is compared with numerical simulations based on SPINEVOLUTION [7] (solid black line). The following parameters were employed in the simulations: $C_Q = 1$ MHz, η=1.0, $\nu_r = 40$ kHz and RF amplitude, $\nu_1 = 10$ kHz.

To verify the exactness of the above results, simulations emerging from the above expression are compared with exact numerical simulations based on SPINEVOLUTION [7]. As depicted in Figure 2.12, the analytic simulations from AHT (indicated in red) are in excellent agreement with numerical solutions (indicated through black solid lines) at stroboscopic time-intervals. Nevertheless, the loss of signal intensity at integral multiples of $n * \frac{\tau_r}{4}$ (where n=1,3,5,..) remains unexplained in the AHT framework. From an experimental perspective, the finer oscillations (within the rotor period) at non-stroboscopic time-intervals do play an important role (when the time-domain signal is Fourier transformed) and could be derived using methods based on Floquet theory. In what follows, we employ two formulations of Floquet theory for describing the excitation in spin-1 system. In the first formulation, the time-evolution is described in the extended Hilbert space (or Floquet space) through time-propagators based on effective Floquet Hamiltonians. In the second approach, the

time-propagators are defined in the standard Hilbert space through product of exponential operators. Although,the application of these methods in studying spin-1/2 systems is well-known, the suitability of these methods in studying quadrupolar spins remains less explored in rotating solids.

2.3.2.2 Time evolution based on Effective Floquet Hamiltonian

In the effective Floquet Hamiltonian framework, the time-dependent Hamiltonian in the quadrupolar interaction frame (Eq. 2.60) is transformed into a time-independent Floquet Hamiltonian via Fourier series expansion. Employing operator based perturbation methods, an effective Floquet Hamiltonian (valid at all time-intervals) is derived to describe the time-evolution at non-stroboscopic time-intervals and is well documented in the literature [49–51,53,54,67].

$$\begin{aligned} H_F &= \omega_r I_F + \sqrt{2}\omega_1 J_0(A)\left[I_X^{12} + I_X^{23}\right]_0 \\ &+ \sqrt{2}\omega_1 \left\{ \sum_{k=\pm 4,\pm 8,..} J_{k/2}(A)\left[I_X^{12} + I_X^{23}\right]_k + i \sum_{m=\pm 2,\pm 6,..} J_{m/2}(A)\left[I_Y^{12} - I_Y^{23}\right]_m \right\} \end{aligned} \tag{2.69}$$

To facilitate descriptions based on operator based perturbation methods (such as contact transformation [41,42] or van vleck transformation [43]), the Hamiltonian is split and expressed as a sum comprising zero order (H_0) and perturbing Hamiltonian (H_1).

$$H_0 = \omega_r I_F \tag{2.70}$$

The perturbing Hamiltonian is further split into a diagonal (denoted by $H_{1,d}$) and an off-diagonal part ($H_{1,od}$).

$$H_1 = H_{1,d} + H_{1,od} \tag{2.71}$$

$$H_{1,d} = \sqrt{2}\omega_1 J_0(A)\left[I_X^{12} + I_X^{23}\right]_0 \tag{2.72}$$

$$\begin{aligned} H_{1,od} &= \sum_{p=\pm 4n} \underbrace{\sqrt{2}\omega_1 J_{p/2}}_{G_X^{(p)}}\left[I_X^{12} + I_X^{23}\right]_p + i \sum_{p=\pm(4n-2)} \underbrace{\sqrt{2}\omega_1 J_{p/2}}_{G_Y^{(p)}}\left[I_Y^{12} - I_Y^{23}\right]_p \\ &= \sum_{p=\pm 4n} G_X^{(p)}\left[I_X^{12} + I_X^{23}\right]_p + i \sum_{p=\pm(4n-2)} G_Y^{(p)}\left[I_Y^{12} - I_Y^{23}\right]_p \end{aligned} \tag{2.73}$$

where $n \in \mathbb{N}$ (natural numbers, e.g. 1,2,3,....).

Employing the transformation function, $S_1 = i\left(\sum_p C_X^{(p)}[I_X^{12}+I_X^{23}]_p + i\sum_p C_Y^{(p)}[I_Y^{12}-I_Y^{23}]_p\right)$, the off-diagonal contributions due to $H_{1,od}$ are folded to give an effective Hamiltonian as given below.

$$H_F^{eff} = \omega_r I_F + \widetilde{H}_{1,d} + \frac{i}{2}[S_1, H_{1,od}] \quad ; \quad \widetilde{H}_{1,d} = e^{i\lambda S_1} H_{1,d} e^{-i\lambda S_1} \tag{2.74}$$

To second order, the effective Hamiltonian is represented by the following equation.

$$\begin{aligned} H_F^{eff} = H_0 + H_2^{(1)} = \omega_r I_F + \sqrt{2}\omega_1 J_0(A)\left\{\left[I_X^{12}+I_X^{23}\right]_0 - \sum_p C_Y^{(p)}\left[I_Z^{12}-I_Z^{23}+I_X^{13}\right]_p\right\} \\ + \frac{1}{2}\sum_p\sum_m\left\{C_X^{(p)}G_Y^{(m)} - C_Y^{(p)}G_X^{(m)}\right\}\left[I_Z^{12}-I_Z^{23}+I_X^{13}\right]_{p+m} \end{aligned} \tag{2.75}$$

To maintain consistency, both the initial density operator $\rho(0) = 2I_Z^{13}$ and detection operator $D = I_+^{13}$ is transformed by S_1.

$$\widetilde{\rho}(0) = e^{i\lambda S_1}U_1\rho(0)U_1^{-1}e^{-i\lambda S_1} = \sum_p C_\alpha^{ij(p)}\left[I_\alpha^{ij}\right]_p \quad ; \quad \rho(0) = \left[2I_Z^{13}\right]_0 \tag{2.76}$$

$$\widetilde{D_F} = e^{i\lambda S_1}U_1 D_F U_1^{-1}e^{-i\lambda S_1} = \sum_p D_\alpha^{ij(p)}\left[I_\alpha^{ij}\right]_p \quad ; \quad D_F = \left[I_+^{13}\right]_0 \tag{2.77}$$

Employing the effective Hamiltonian (Eq. 2.75), the density operator during the pulse in the Floquet framework is evaluated using the standard equation given below.

$$\widetilde{\rho}(t) = e^{-iH_F^{eff}t}\widetilde{\rho}(0)e^{iH_F^{eff}t} = \sum_p R_\alpha^{ij(p)}(t)\left[I_\alpha^{ij}\right]_p \tag{2.78}$$

Subsequently, utilizing the properties of the Floquet operators, the final signal (corresponding to DQ excitation) is evaluated. Based on the operators involved in the density operator and detection operator (refer to Table 2.3), the final signal expression reduces to zero.

$$S(t) = Tr\left[\widetilde{\rho}(t)\widetilde{D}\right] = \sum_p R_\alpha^{ij(p)}(t)D_\beta^{ji(-p)} = 0 \tag{2.79}$$

From an operational perspective, the above result is bit intriguing considering the fact that the calculations in the quadrupolar interaction frame (in static samples) do give results in excellent agreement with numerical simulations in both the strong and weak coupling regimes [29]. To explicate the discrepancies observed between the methods, we examine the higher order corrections from AHT to those obtained from the effective Hamiltonians. As illustrated, the first-order correction ($H_{1,d}$) in the effective Floquet Hamiltonian framework, comprises diagonal ($[I_X^{12}]_0$ and $[I_X^{23}]_0$) operators that are identical to those obtained from $\bar{H}^{(1)}$

operators	Initial Density Operator, $C_\alpha^{ij(p)}$	Detection Operator, $D_\alpha^{ij(p)}$	Density Operator, $R_\alpha^{ij(p)}(t)$
$[I_Z^{13}]_0$	$2\left(1+\frac{x}{4}\right)$	0	$2\left(1+\frac{x}{4}\right)\cos(\omega_e t)$
$[I_+^{13}]_0$	0	$1+\frac{x}{4}$	0
$[I_Y^{12}+I_Y^{23}]_0$	0	0	$-\sqrt{2}\left(1+\frac{x}{4}\right)\sin(\omega_1 t J_0(A))$
$[I_+^{12}]_p$	$\frac{1}{2}\left[C_X^{(p)}+C_Y^{(p)}\right]$	$\frac{1}{2}\left[C_X^{(p)}+C_Y^{(p)}\right]$	$\frac{1}{2}\left[C_X^{(p)}+C_Y^{(p)}\right]e^{-ip\omega_r t}\cos(\omega_e t)$
$[I_-^{21}]_p$	$\frac{1}{2}\left[-C_X^{(p)}+C_Y^{(p)}\right]$	0	$\frac{1}{2}\left[-C_X^{(p)}+C_Y^{(p)}\right]e^{-ip\omega_r t}\cos(\omega_e t)$
$[I_+^{23}]_p$	$\frac{1}{2}\left[C_X^{(p)}-C_Y^{(p)}\right]$	$\frac{1}{2}\left[-C_X^{(p)}+C_Y^{(p)}\right]$	$\frac{1}{2}\left[C_X^{(p)}-C_Y^{(p)}\right]e^{-ip\omega_r t}\cos(\omega_e t)$
$[I_-^{32}]_p$	$-\frac{1}{2}\left[C_X^{(p)}+C_Y^{(p)}\right]$	0	$-\frac{1}{2}\left[C_X^{(p)}+C_Y^{(p)}\right]e^{-ip\omega_r t}\cos(\omega_e t)$
$[I_Z^{13}]_p$	0	0	$i\sqrt{2}C_X^{(p)}e^{-ip\omega_r t}\sin(\omega_1 t J_0(A))$
$[I_Y^{13}]_p$	0	0	$-\sqrt{2}C_Y^{(p)}e^{-ip\omega_r t}\sin(\omega_1 t J_0(A))$
	$x=\sum_p\left[C_X^{(p)}C_X^{(-p)}-C_Y^{(p)}C_Y^{(-p)}\right]$		$\omega_e=\omega_1 J_0(A)\sqrt{1+2\sum_p C_Y^{(p)}C_Y^{(-p)}}$
	$C_X^{(p)}=-\frac{G_X^{(p)}}{p\omega_r}$		$C_Y^{(p)}=-\frac{G_Y^{(p)}}{p\omega_r}$

Table 2.3: The definition of constants employed in the description of the density operator and detection operator (refer to Eqns. (2.76-2.78)) based on the Effective Floquet Hamiltonians (MAS case)

in the AHT framework. In a similar vein, the second-order contributions in the AHT framework (associated with $\bar{H}^{(2)}$) could be related to the term $[S_1, H_{1,d}]$ in the effective Floquet Hamiltonian framework. While the form of the second-order coefficients remain identical in both the methods, the spin operators in the Floquet framework are off-diagonal in the Fourier dimension. Consequently, the derivation of an "effective rotation operator" in the Floquet framework is hindered by the simultaneous presence of both (a) non-commuting (b) and off-diagonal operators (off-diagonal with respect to both spin and Fourier space). By contrast, the unitary transformation, U_2 (refer to Eq. 2.64) employed in the standard Hilbert space facilitates in the derivation of an effective rotation operator (Eq. 2.64) comprising commuting set of operators. Such an approach facilitates in obtaining a closed form solution during the excitation pulse. Hence, the discrepancy observed in the effective Floquet Hamiltonian framework could be solely attributed to the presence of off-diagonal operators in the Fourier space (resulting from $[S_1, H_{1,d}]$). In the following subsection, an alternate Floquet method, Floquet Magnus expansion (FME) scheme is explored to describe the spin dynamics.

2.3.2.3 Time evolution based on Floquet Magnus Expansion (FME)

In the Floquet-Magnus expansion scheme [68–70], the evolution operator is expressed as a product of operators based on the Floquet theorem. In its most general formulation, the evolution operator is expressed by the following equation.

$$U(t,0) = e^{-i\Lambda(t)} e^{-i\bar{H}t} e^{i\Lambda(0)} \tag{2.80}$$

The operators $\bar{H}$ and $\Lambda(t)$ are derived in terms of a perturbation expansion as given below.

$$\bar{H} = \sum_n \lambda^n \bar{H}^{(n)} \;\; ; \;\; \Lambda(t) = \sum_n \lambda^n \Lambda_n(t) \tag{2.81}$$

Depending upon the boundary condition (whether $\Lambda(0) = 0$ or $\Lambda(0) \neq 0$), the form of the expansion terms in $\bar{H}$ and $\Lambda(t)$ differ and would be discussed below. The spin dynamics using the normal boundary condition ($\Lambda(0) = 0$) is described in Appendix-E.

1. Alternate Boundary Condition ($\Lambda(0) \neq 0$)

In the alternate boundary condition, the time-propagator is expressed as a product of three exponential operators and has the following form,

$$U(t,0) = e^{-i\Lambda(t)} e^{-i\bar{H}t} e^{i\Lambda(0)} \tag{2.82}$$

General Expression	Coefficients and Operators
$\bar{H}^{(1)} = H_0$	$\bar{H}^{(1)} = \sqrt{2}\omega_1 J_0(A)\left[I_X^{12} + I_X^{23}\right]$
$\bar{H}^{(2)} = \sum_{k\neq 0}\left\{\frac{[H_k, H_{-k}]}{2k\omega}\right\}$	$\bar{H}^{(2)} = 0$
$\Lambda_1(t) = \sum_{k\neq 0}\frac{e^{ik\omega t}}{ik\omega}H_k$	$\Lambda_1(t) = a(t)\left[I_Y^{12} - I_Y^{23}\right] + b(t)\left[I_X^{12} + I_X^{23}\right]$
$\Lambda_1(0) = \sum_{k\neq 0}\frac{1}{ik\omega}H_k$	$\Lambda_1(0) = a(0)\left[I_Y^{12} - I_Y^{23}\right]$
$a(t) = \frac{\sqrt{2}\omega_1}{\omega_r}\left[\sum_{n=2p-1}\frac{J_n(A)}{n}\left[\cos(2n\omega_r t)\right]\right]$	$b(t) = \frac{\sqrt{2}\omega_1}{\omega_r}\sum_{n=2p}\frac{J_n(A)}{n}\sin(2n\omega_r t)$

Table 2.4: Generalized expressions for $\bar{H}$ and $\Lambda(t)$ in the FME scheme (MAS case) corresponding to alternate boundary condition ($\Lambda(0) \neq 0$)

Based on the expressions given in Table 2.4, the expansion terms in $\bar{H}$ and $\Lambda(t)$ are evaluated. In contrast to the normal boundary condition (refer to Appendix-E), the second-order term ($\bar{H}^{(2)}$) is zero in the alternate boundary condition.

$$\bar{H} = \bar{H}^{(1)} + \bar{H}^{(2)} = \sqrt{2}\omega_1 J_0(A)\left[I_X^{12} + I_X^{23}\right] \tag{2.83}$$

For the sake of simplicity, the correction terms in $\Lambda(t)$ are confined to first order only.

$$\Lambda_1(t) = \sum_{k\neq 0}\frac{e^{ik\omega_r t}}{ik\omega_r}H_k = a(t)\left[I_Y^{12} - I_Y^{23}\right] + b(t)\left[I_X^{12} + I_X^{23}\right] \tag{2.84}$$

At time t=0, the above expression reduces to a simpler form given below.

$$\Lambda_1(0) = \sum_{k\neq 0}\frac{1}{ik\omega_r}H_k = \frac{\sqrt{2}\omega_1}{\omega_r}\left[\sum_{n=2p-1}\frac{J_n(A)}{n}\right]\left[I_Y^{12} - I_Y^{23}\right] \tag{2.85}$$

where, $p \in \mathbb{N}$ (natural numbers, e.g. 1,2,3,....).

Employing the transformed operators and the time-propagator given in Eq. (2.82), the DQ signal during the excitation pulse is evaluated through the equations given below.

$$S(t) = Tr\left[\underbrace{e^{-i\bar{H}t}e^{i\Lambda(0)}U_1\rho(0)U_1^{-1}e^{-i\Lambda(0)}e^{i\bar{H}t}}_{\widetilde{\rho}(t)}.\overbrace{e^{i\Lambda(t)}U_1DU_1^{-1}e^{-i\Lambda(t)}}^{\widetilde{D}(t)}\right] = Tr\left[\widetilde{\rho}(t)\widetilde{D}(t)\right] \quad (2.86)$$

$$\begin{aligned}\widetilde{\rho}(0) &= e^{i\Lambda(0)}U_1\rho(0)U_1^{-1}e^{-i\Lambda(0)} = \sum C_\alpha^{ij}I_\alpha^{ij} \\ &= \left\{2\cos\left(\frac{a(0)}{\sqrt{2}}\right)\right\}\left[I_Z^{13}\right] + \left\{-\sqrt{2}\sin\left(\frac{a(0)}{\sqrt{2}}\right)\right\}\left[I_X^{12} - I_X^{23}\right]\end{aligned} \quad (2.87)$$

$$\widetilde{D}(t) = e^{i\Lambda(t)}U_1DU_1^{-1}e^{-i\Lambda(t)} = \sum D_\alpha^{ij}(t)I_\alpha^{ij} \quad (2.88)$$

$$\begin{aligned}\widetilde{\rho}(t) &= e^{-i\bar{H}t}\widetilde{\rho}(0)e^{i\bar{H}t} = \sum R_\alpha^{ij}(t)I_\alpha^{ij} \\ &= \left\{2\cos\left(\frac{a(0)}{\sqrt{2}}\right)\cos\left(\omega_e t\right)\right\}\left[I_Z^{13}\right] + \left\{-\sqrt{2}\cos\left(\frac{a(0)}{\sqrt{2}}\right)\sin\left(\omega_e t\right)\right\}\left[I_Y^{12} + I_Y^{23}\right] \\ &+ \left\{-\sqrt{2}\sin\left(\frac{a(0)}{\sqrt{2}}\right)\cos\left(\omega_e t\right)\right\}\left[I_X^{12} - I_X^{23}\right] + \left\{2\sin\left(\frac{a(0)}{\sqrt{2}}\right)\sin\left(\omega_e t\right)\right\}\left[I_Y^{13}\right]\end{aligned} \quad (2.89)$$

The final form of the signal during the excitation is represented by the following equation.

$$\begin{aligned}S(t) = \sum R_\alpha^{ij}(t)D_\beta^{ji}(t) &= \frac{i}{2}\sin\left(\frac{a(0)}{\sqrt{2}}\right)\sin\left(\omega_e t\right)\left(1 - \frac{a^2(t)+b^2(t)}{4}\right) \\ &+ \frac{i}{2\sqrt{2}}\left(a(t)\cos\left(\frac{a(0)}{\sqrt{2}}\right)\sin\left(\omega_e t\right) + b(t)\sin\left(\frac{a(0)}{\sqrt{2}}\right)\cos\left(\omega_e t\right)\right) \\ &= F_0e^{\pm i\omega_e t} + \sum_{p\in\mathbb{N}} F_p e^{\pm i(\omega_e \pm 2p\omega_r)t}\end{aligned} \quad (2.90)$$

where $\omega_e = \omega_1 J_0(A)$. The terms F_0 $\left(\propto \sin\left(\frac{a(0)}{\sqrt{2}}\right)\right)$ and F_p, represent the amplitudes of centerband and p^{th} sideband, respectively. A detailed description of the coefficients employed in the calculations is listed in Table 2.5. As depicted in Figure 2.13, the analytic simulations from the FME scheme are in excellent agreement to those obtained from exact numerical methods.

To explain the observed loss of the signal at (odd) integral multiples of $n * \frac{\tau_r}{4}$ (n=1,3,5..), the signal expression given in Eq. (2.90) is re-expressed in the following form.

$$S(t) = iA(t)\sin\left(\omega_e t\right) + iB(t)\cos\left(\omega_e t\right) \quad (2.91)$$

operators	Initial Density Operator, C_α^{ij}	Detection Operator, $D_\alpha^{ij}(t)$	Density Operator, $R_\alpha^{ij}(t)$
I_Z^{13}	$2\cos\left(\frac{a(0)}{\sqrt{2}}\right)$	0	$2\cos\left(\frac{a(0)}{\sqrt{2}}\right)\cos(\omega_e t)$
I_+^{12}	$-\frac{1}{\sqrt{2}}\sin\left(\frac{a(0)}{\sqrt{2}}\right)$	$-\frac{a(t)+ib(t)}{2}$	$\frac{i}{\sqrt{2}}\cos\left(\frac{a(0)}{\sqrt{2}}\right)\sin(\omega_e t)-\frac{1}{\sqrt{2}}\sin\left(\frac{a(0)}{\sqrt{2}}\right)\cos(\omega_e t)$
I_-^{21}	$-\frac{1}{\sqrt{2}}\sin\left(\frac{a(0)}{\sqrt{2}}\right)$	0	$-\frac{i}{\sqrt{2}}\cos\left(\frac{a(0)}{\sqrt{2}}\right)\sin(\omega_e t)-\frac{1}{\sqrt{2}}\sin\left(\frac{a(0)}{\sqrt{2}}\right)\cos(\omega_e t)$
I_+^{23}	$\frac{1}{\sqrt{2}}\sin\left(\frac{a(0)}{\sqrt{2}}\right)$	$-\frac{a(t)-ib(t)}{2}$	$\frac{i}{\sqrt{2}}\cos\left(\frac{a(0)}{\sqrt{2}}\right)\sin(\omega_e t)+\frac{1}{\sqrt{2}}\sin\left(\frac{a(0)}{\sqrt{2}}\right)\cos(\omega_e t)$
I_-^{32}	$\frac{1}{\sqrt{2}}\sin\left(\frac{a(0)}{\sqrt{2}}\right)$	0	$-\frac{i}{\sqrt{2}}\cos\left(\frac{a(0)}{\sqrt{2}}\right)\sin(\omega_e t)+\frac{1}{\sqrt{2}}\sin\left(\frac{a(0)}{\sqrt{2}}\right)\cos(\omega_e t)$
I_+^{13}	0	$1-\frac{1}{4}\left[a^2(t)+b^2(t)\right]$	$-i\sin\left(\frac{a(0)}{\sqrt{2}}\right)\sin(\omega_e t)$
I_-^{31}	0	0	$i\sin\left(\frac{a(0)}{\sqrt{2}}\right)\sin(\omega_e t)$
		$\omega_e = \omega_1 J_0(A)$	

Table 2.5: Definition of constants employed in the description of the density operator and detection operator (Eq. 2.87-2.89) based on the FME (MAS case) corresponding to alternate boundary condition ($\Lambda(0) \neq 0$)

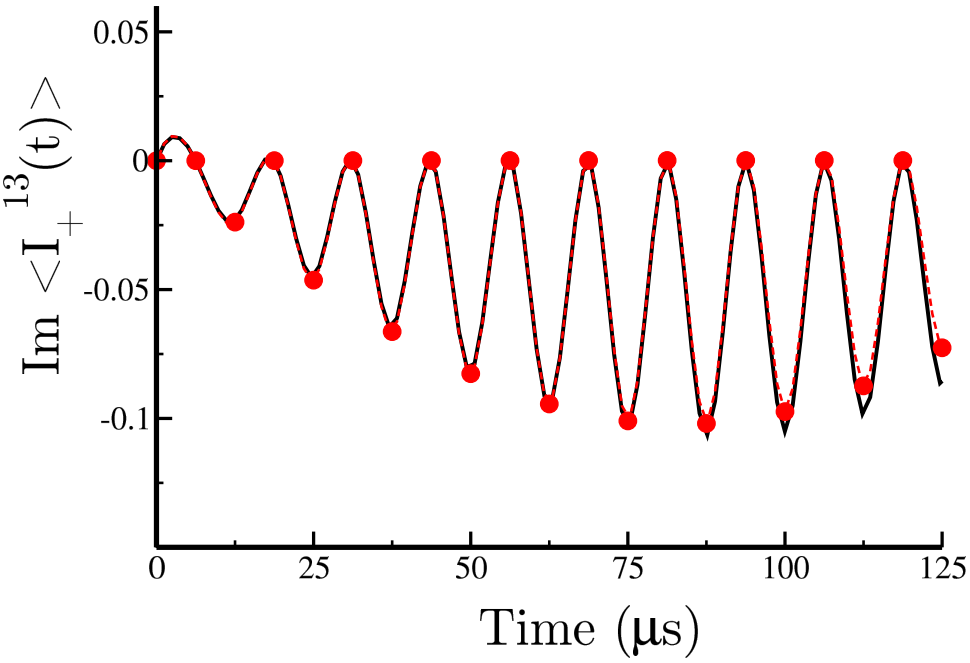

Figure 2.13: In the MAS simulations depicted, excitation of DQ transitions in spin I=1 system is presented. The validity of the FME scheme ($\Lambda(0) \neq 0$, indicated by red dots based on Eq. 2.90) is compared with numerical simulations based on SPINEVOLUTION [7] (solid black line). The following parameters were employed in the simualtions: $C_Q = 1$ MHz, η=1.0, $\nu_r = 40$ kHz and RF amplitude, $\nu_1 = 10$ kHz.

where,

$$A(t) = \frac{1}{2}\sin\left(\frac{a(0)}{\sqrt{2}}\right)\left(1 - \frac{a^2(t)+b^2(t)}{4}\right) + \frac{1}{2\sqrt{2}}a(t)\cos\left(\frac{a(0)}{\sqrt{2}}\right) \tag{2.92}$$

$$B(t) = \frac{1}{2\sqrt{2}}b(t)\sin\left(\frac{a(0)}{\sqrt{2}}\right) \tag{2.93}$$

As depicted in Figure 2.14, both the coefficients A(t) (first row) and B(t) (second row) tend to zero at (odd) integral multiples of $n * \frac{\tau_r}{4}$ (n=1,3,5..) and are directly responsible for the signal loss in the excitation profile observed in the simulations. Subsequently, the signal expression at integral multiples of $\frac{\tau_r}{4}$ reduces to the form given below.

$$S(t) = \frac{i}{2}\sin(\omega_e t)\left\{\sin\left(\frac{a(0)}{\sqrt{2}}\right)\left(1 - \frac{a^2(t)+b^2(t)}{4}\right) + \frac{1}{\sqrt{2}}a(t)\cos\left(\frac{a(0)}{\sqrt{2}}\right)\right\} \tag{2.94}$$

From an operational perspective, the analytic calculations/expressions (refer to Table 2.4

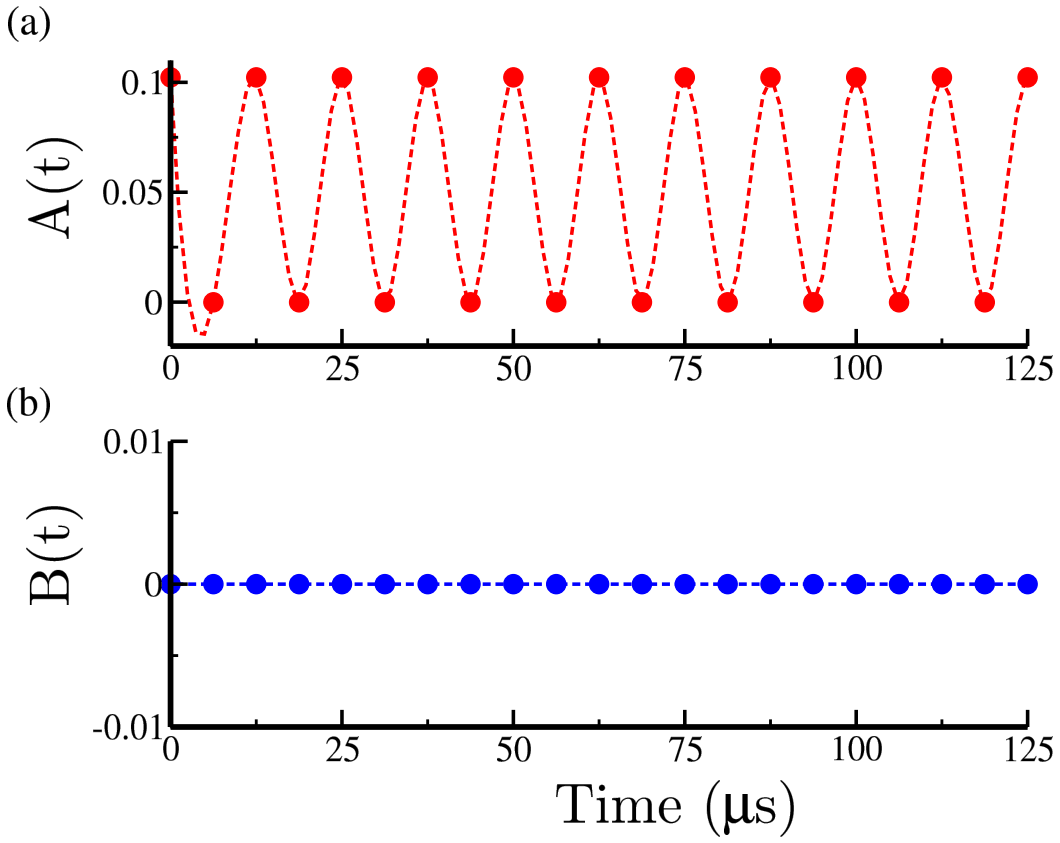

Figure 2.14: In the MAS simulations depicted, (a) the coefficient A(t) (refer to Eq. 2.92) (b) the coefficient B(t) (refer to Eq. 2.93) is plotted. The following parameters were employed in the simualtions: $C_Q = 1$ MHz, $\eta = 1.0$, $\nu_r = 40$ kHz and RF amplitude, $\nu_1 = 10$ kHz.

and 2.5) based on the alternate boundary condition are more insightful and less cumbersome to evaluate when compared to those obtained from the normal boundary condition (refer to Appendix-E). In the following subsections, the role of the RF amplitude and the spinning frequency on the DQ excitation efficiency is discussed along with the convergence criterion in the analytic simulations.

(a) The role of RF amplitude and spinning frequency

To explicate the role of the RF amplitude and spinning frequency on the DQ excitation efficiency, additional simulations were performed. In the simulations depicted in Figure 2.15, the DQ excitation efficiency is monitored as a function of spinning frequency at constant RF amplitude and quadrupolar coupling constant. In a similar vein, in the simulations depicted in Figure 2.16, the DQ excitation efficiency is monitored as a function of the RF amplitude

at a given spinning frequency and quadrupolar coupling constant.

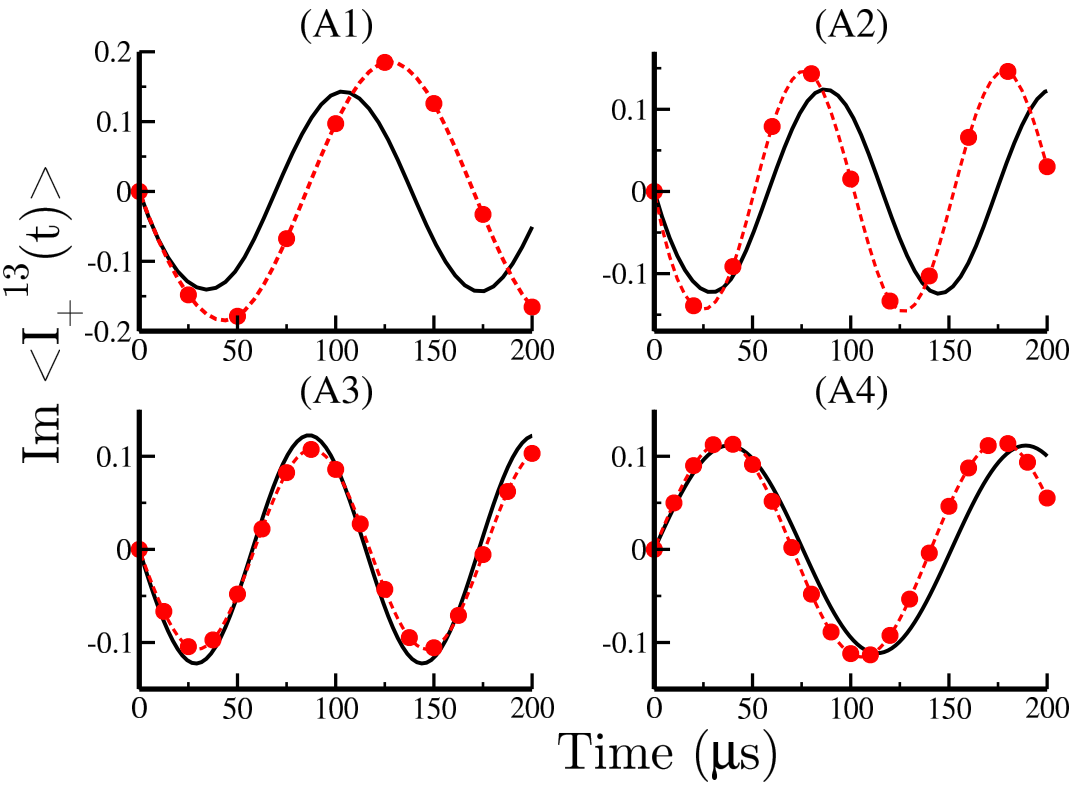

Figure 2.15: In the simulations depicted, the validity of the FME Scheme (alternate boundary condition) is checked by varying the spinning frequency, ν_r while keeping $\nu_1 = 40$ kHz and $C_Q = 2$ MHz constant ($\eta = 1.0$). The analytic simulations based on the calculations (dotted red line) are compared with those obtained from exact numerical methods based on SPINEVOLUTION [7] (solid black line). The spinning frequency, ν_r is varied as - (A1) 20 kHz (A2) 25 kHz (A3) 40 kHz (A4) 50 kHz.

As depicted in the simulations, the DQ excitation efficiency decreases with increase in spinning frequency (refer to Figure 2.15) and increases with increase in the RF amplitude (refer to Figure 2.16). While these observations are in accord with known experimental results [71], a formal explanation of the above trend has remained unexplained. Below, we present an explanation based on the density operator formalism proposed in the previous subsection.

In the FME approach based on the alternate boundary condition ($\Lambda(0) \neq 0$), the optimal conditions for DQ excitation could be inferred from the coefficients associated with the transverse operators (I_X^{12} and I_X^{23}) present in the initial density operator, $\widetilde{\rho}(0)$. As illustrated in Eq. (2.87), the coefficients associated with the transverse operators are proportional to

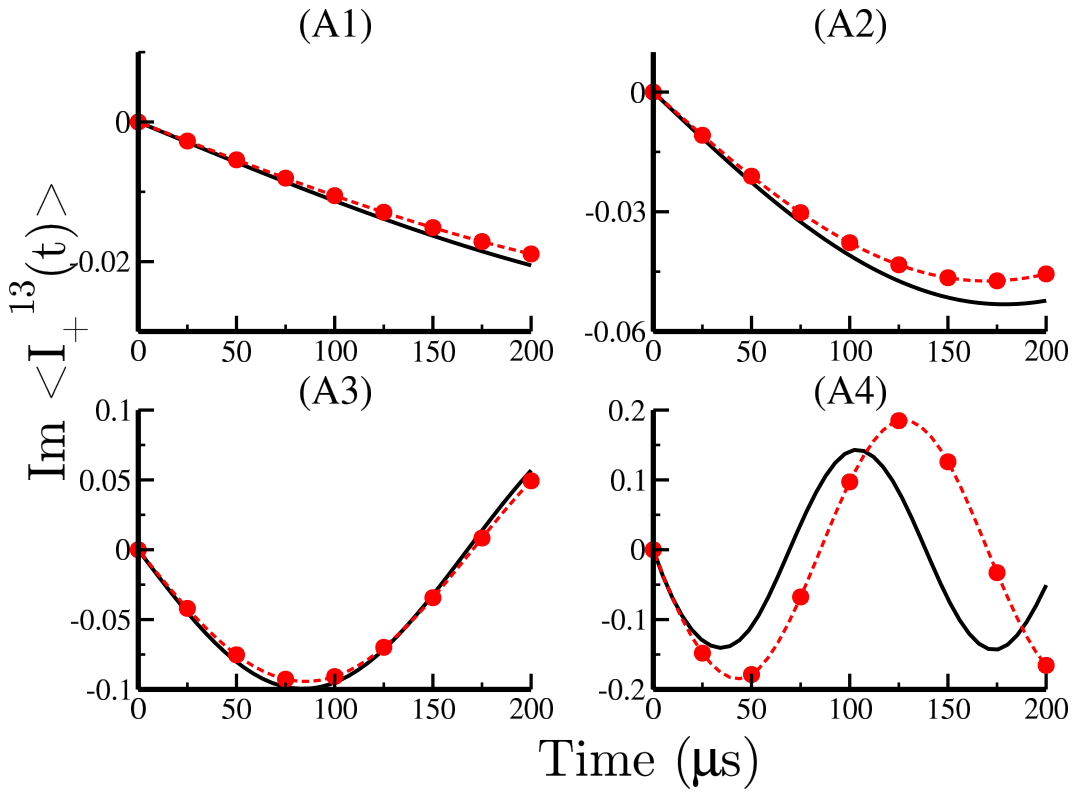

Figure 2.16: In the simulations depicted (MAS case), the validity of the FME Scheme (alternate boundary condition) is checked by varying the RF amplitude, ν_1 while keeping $\nu_r = 20$ kHz and $C_Q = 2$ MHz constant ($\eta = 1.0$). The analytic simulations based on the calculations (dotted red line) are compared with those obtained from exact numerical methods based on SPINEVOLUTION [7] (solid black line). The RF amplitude, ν_1 is varied as - (A1) 5 kHz (A2) 10 kHz (A3) 20 kHz (A4) 40 kHz.

$\sin\left(\frac{a(0)}{\sqrt{2}}\right)$ (where, $a(0) \propto \frac{\omega_1}{\omega_r}$). During the excitation pulse, the transverse operators in $\widetilde{\rho}(0)$ are transformed into double-quantum operators/coherence through the single quantum operators (I_X^{12} and I_X^{23}) present in the evolution operator, $e^{-i\bar{H}t}$. Consequently, the DQ coherence present in $\widetilde{\rho}(t)$ is proportional to the factor, $\sin\left(\frac{a(0)}{\sqrt{2}}\right)$ (refer to coefficients associated with I_Y^{13} operator in Eq. 2.89). Hence, the DQ excitation efficiency maximizes at higher RF amplitudes and decreases with increasing spinning frequencies.

In contrast to the description based on the normal boundary condition (refer to Appendix-E), the description employing time-propagators derived from the alternate boundary condition presents an attractive framework for explicating the nuances of excitation in multi-level systems. To further verify the exactness of the FME approach, the DQ excitation at rotary

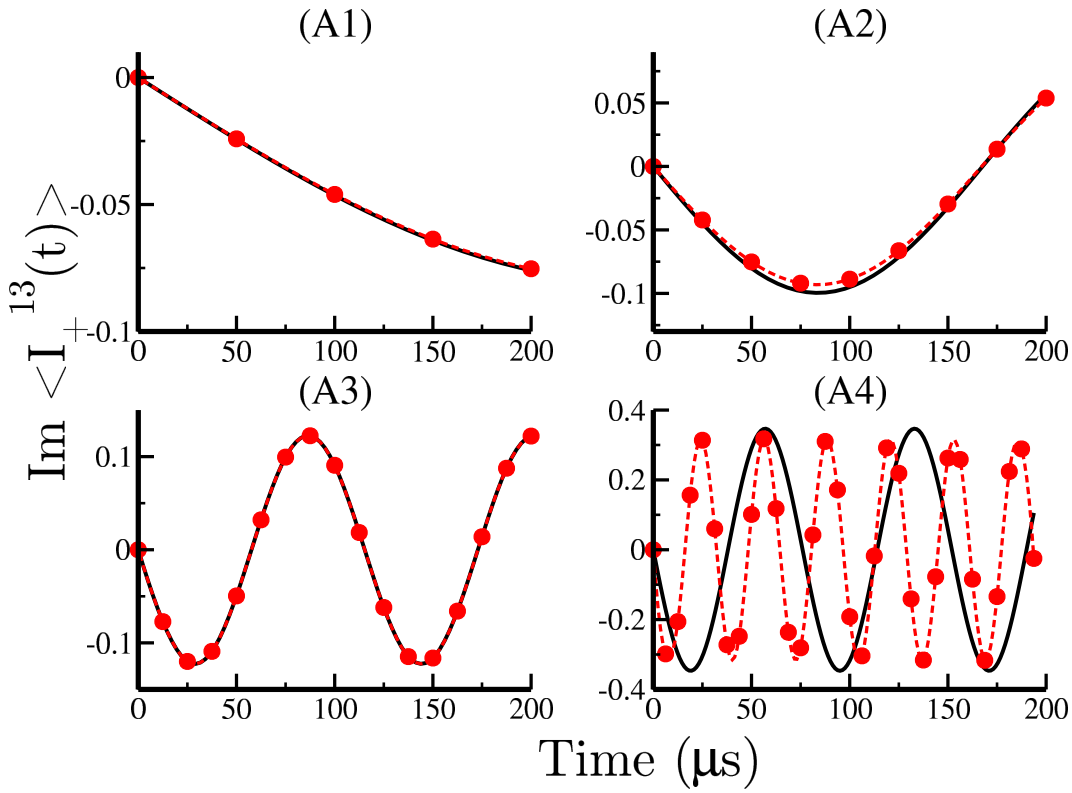

Figure 2.17: In the simulations depicted, the validity of the FME Scheme is checked for rotary resonance conditions ($\nu_1 = \nu_r$), keeping $C_Q = 2$ MHz constant ($\eta = 1.0$). The analytic simulations based on the calculations (dotted red line) are compared with those obtained from exact numerical methods based on SPINEVOLUTION [7] (solid black line). The RF amplitude in the simulations is varied as- (A1) 10 kHz (A2) 20 kHz (A3) 40 kHz (A4) 80 kHz.

resonance conditions ($\omega_1 = \omega_r$) was also explored. As depicted in Figure 2.17, the analytic simulations are in good agreement with the numerical simulations at lower RF amplitudes. The deviations observed at higher RF amplitudes could be explained based on the relative magnitudes of the RF amplitude, sample spinning frequency and effective quadrupolar frequency and is addressed in the following subsection.

(b) Convergence criterion in analytic simulations.

To account for the deviations observed in the analytic simulations (refer to Figures 2.15-2.17), additional set of simulations at and far from rotary resonance conditions were studied. In cases where the simulation parameters are far from rotary resonance conditions (refer to Figures 2.15-2.16), the convergence criterion is solely based on the ratio of the RF amplitude to the spinning frequency, irrespective of the magnitude of the quadrupolar coupling constant.

When the ratio $\left(\frac{\omega_1}{\omega_r}\right)$ exceeds 1, significant deviations are observed in the analytic simulations (refer to Figure 2.15). The observed deviations in the analytic simulations (refer to Figure 2.18, panels B1, B2 and B3) could be attributed to the divergence of the expansion terms involved in $\Lambda(t)$.

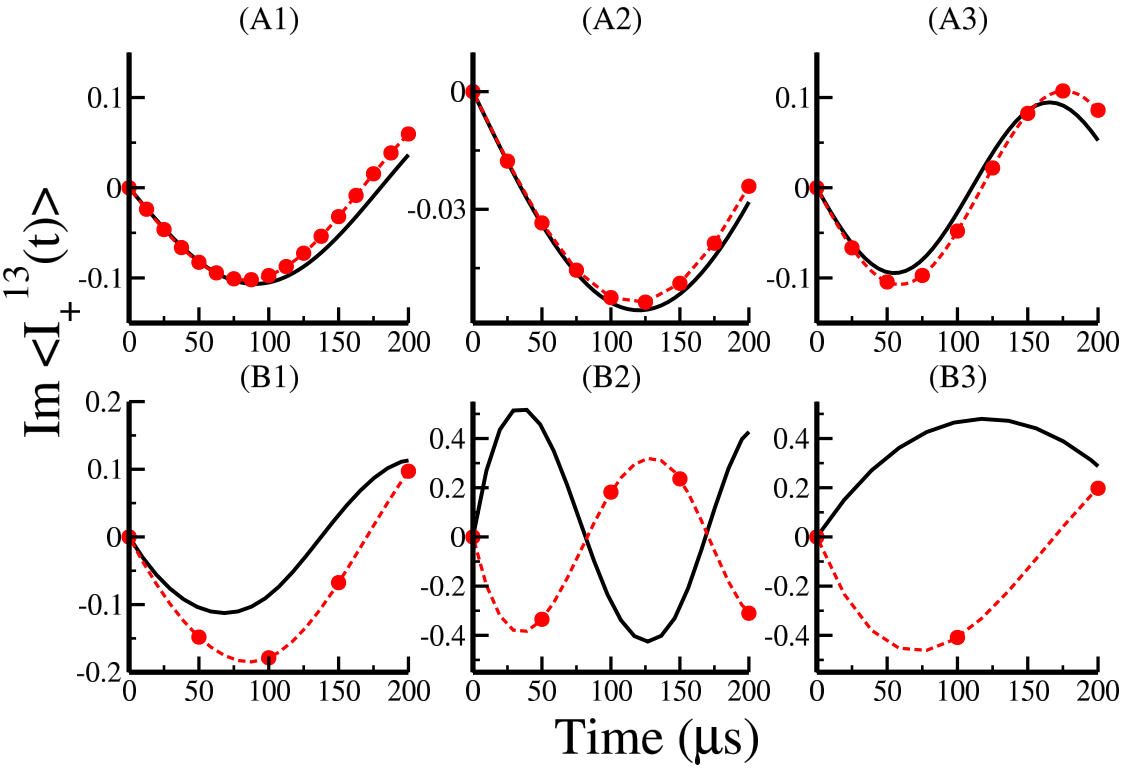

Figure 2.18: In the simulations depicted, the validity of the FME Scheme (alternate boundary condition) is checked by varying the RF amplitude, ν_1 and spinning frequency, ν_r while keeping C_Q = 1 MHz ($\nu_{Q,2}^{(2)0}$ = 250 kHz) constant. The analytic simulations based on the calculations (dotted red line) are compared with those obtained from exact numerical methods based on SPINEVOLUTION [7] (solid black line). The ratio $\frac{\nu_1}{\nu_r}$ is varied as (A1) 0.25 (A2) 0.5 (A3) 1.0 (B1) 2.0 (B2) 4.0 (B3) 6.0 .

As illustrated in Table 2.4, the expansion coefficients (a(t) and b(t)) in $\Lambda(t)$ are proportional to $\frac{\omega_1}{\omega_r}$ and diverge with increasing RF amplitudes leading to deviations in the analytic simulations. This aspect is further substantiated in the simulations depicted in Figure 2.19, wherein, the convergence criterion is examined at different quadrupolar coupling constants. As depicted, the convergence criterion (governed by the ratio of $\frac{\omega_1}{\omega_r}$) in the analytic simulations is independent of the quadrupolar coupling constant.

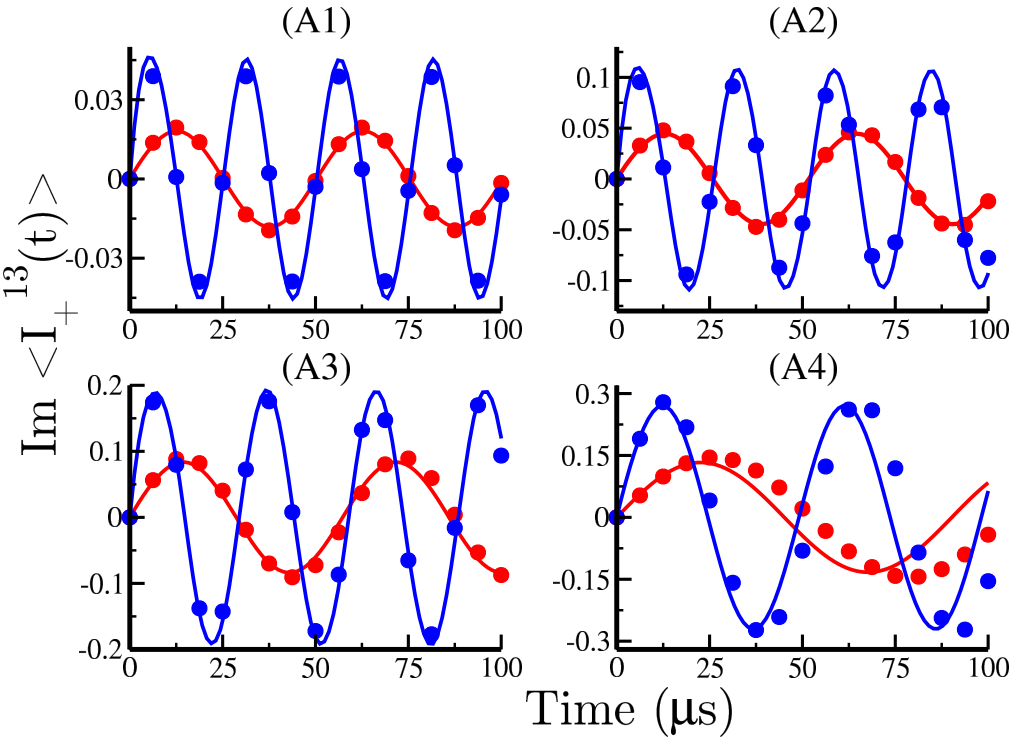

Figure 2.19: In the simulations depicted, the validity of the FME scheme (alternate boundary condition) is checked by varying quadrupolar coupling constant, C_Q. The analytic simulations (dots) are compared with those obtained from exact numerical methods based on SPINEVOLUTION [7] (solid line). Here, the ratio $\frac{\nu_1}{\nu_r}$ is 0.25 (red dots and lines) and is 0.5 (blue dots and lines) while C_Q is varied as- (A1) 100 kHz (A2) 250 kHz (A3) 500 kHz (A4) 1 MHz.

Interestingly, the above criterion is not adhered to in the analytic simulations at rotary resonance conditions. As depicted in Figure 2.17 (refer to panel A4), significant deviations are observed in the analytic simulations at higher RF amplitudes. To explain the deviations, additional simulations at different RF amplitudes were performed (at rotary resonance conditions) by varying the quadrupolar coupling constants.

As depicted in Figure 2.20, the convergence criterion seems to depend on the ratio of the effective quadrupolar frequency to the RF amplitude. The exact factor could be deduced from the ratio of the coefficients associated with the quadrupolar interaction (corresponding to I_Z^{12} and I_Z^{23} operators) and RF amplitude (operators I_X^{12} and I_X^{23} in the rotating frame Hamiltonian (refer to Eq. 2.57). Similar conditions and criterion were also deduced [55,56] for describing the effects of finite pulse effects in two-level systems. When the ratio $\left(\frac{\sqrt{2}\omega_{Q,2}^{(2)0}}{3\omega_1}\right)$ exceeds 4, the analytic simulations (refer to Figure 2.20) are in excellent agreement with

numerical simulations. From a theoretical perspective, this observation could be explained based on the additional transformations employed in the rotating frame. When the ratio $\left(\frac{\sqrt{2}\omega_{Q,2}^{(2)0}}{3\omega_1}\right)$ exceeds 4, the transformation into the quadrupolar interaction frame seems justifiable and the FME approach presents an attractive framework for describing the excitation near rotary resonance condition. On the contrary, when the ratio is lower than 4, the transformation into the RF interaction frame seems a natural choice (refer to Appendix-F). As discussed in Appendix-F, the transformation into the RF interaction frame still yields results in disagreement to those obtained from exact numerical methods. The exact reasons behind the deviations remain under investigation and are certainly beyond the scope of this thesis.

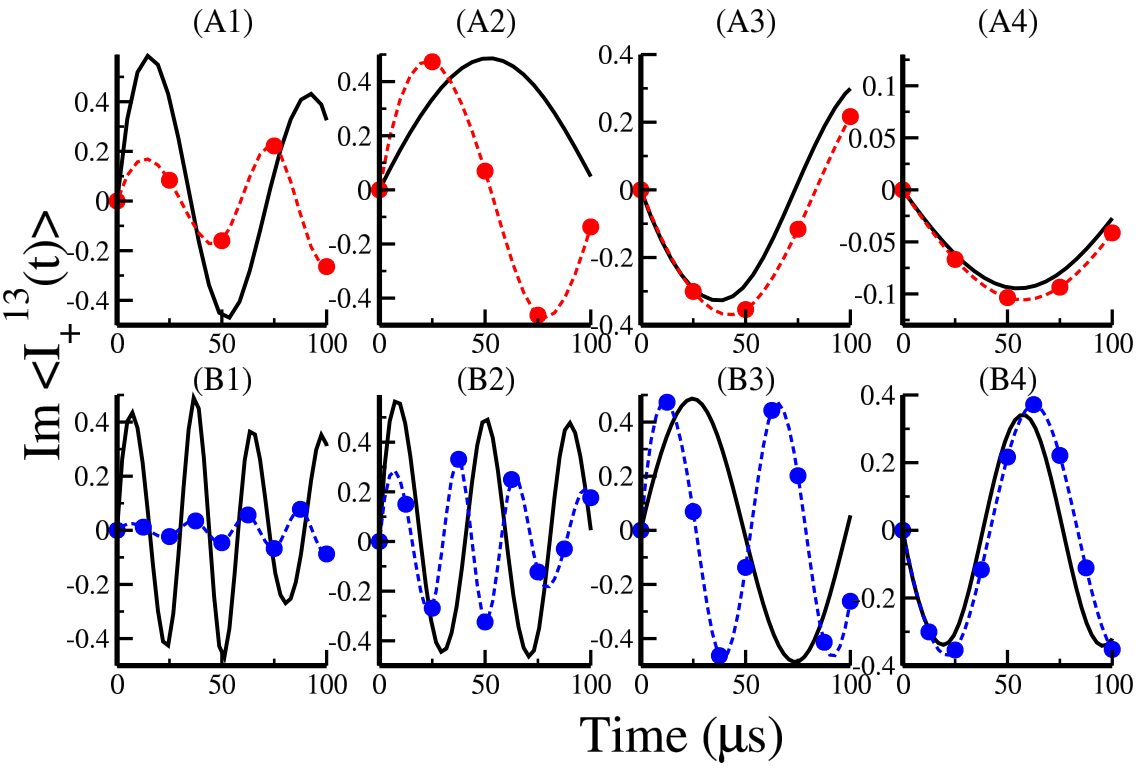

Figure 2.20: In the simulations depicted, the validity of the FME scheme (alternate boundary condition) is checked by varying quadrupolar coupling constant, C_Q for rotary resonance condition ($\nu_1 = \nu_r$). The analytic simulations (dotted line) are compared with those obtained from exact numerical methods based on SPINEVOLUTION [7] (solid line). The RF amplitude in the upper row (panels A1-A4) is 20 kHz and in the bottom row (panels B1-B4) is 40 kHz, while C_Q ($\nu_{Q,2}^{(2)0}$) is varied as- (A1, B1) 100 kHz (25 kHz) (A2, B2) 250 kHz (62.5 kHz) (A3, B3) 500 kHz (125 kHz) (A4, B4) 1 MHz (250 kHz).

2.4 Summary

In summary, the present chapter highlights the strengths and limitations of the existing analytic methods employed for studying finite pulse effects in spin I=1/2 and quadrupolar spin-1 system under MAS. In Section 2.3.1, a detailed description of finite pulse effects in spin I=1/2 system under static and MAS conditions is presented. While the approach based on the concept of "effective fields" presents comprehensive description of the excitation in static samples across all conditions, the validity of the analytical methods in spinning samples depends on the choice of internal (magnitude of CSA interaction) and external parameters (amplitude of the pulse and spinning frequency). Depending on the relative magnitudes of internal and external parameters, two regimes (weak coupling regime and strong coupling regime) are identified. The analytic expressions for both the regimes are derived and substantiated through comparison with numerical simulations.

In Section 2.3.2, Time-propagators for Double-quantum excitation in spin I=1 system is derived using various analytic methods (such as AHT, Effective Floquet Hamiltonian, FME scheme). While the AHT approach offers a simpler framework for deriving the time-propagators, the detection at stroboscopic time-intervals limits its utility in providing a comprehensive description of the spin dynamics. Although, Floquet descriptions based on effective Floquet Hamiltonians have extensively been employed for describing the dynamics in spin-1/2 systems, the present thesis highlights the serious limitations of the effective Floquet Hamiltonian approach in the description of excitation in quadrupolar spins in rotating solids. By contrast, the FME scheme (especially FME with alternate boundary condition) offers an attractive framework for describing the spin dynamics in MQMAS experiments at non-stroboscopic time intervals and offers better insights into the excitation process in comparison to other analytic methods based on Floquet theory.

Appendix D

BCH relations for I=1 system

The operators for spin I=1 system in terms of fictitious spin-operators can be written as-

$$I_x^{ij} = \frac{1}{2}\left[|i\rangle\langle j| + |j\rangle\langle i|\right]$$

$$I_y^{ij} = \frac{1}{2i}\left[|i\rangle\langle j| - |j\rangle\langle i|\right]$$

$$I_z^{ij} = \frac{1}{2}\left[|i\rangle\langle i| - |j\rangle\langle j|\right]$$

The various useful BCH relations [52] among these operators are derived using the following relation and summarized in the following tables.

$$e^{i\theta\hat{A}}\hat{B}e^{-i\theta\hat{A}} = \hat{B} + i\theta[\hat{A},\hat{B}] + \frac{(i\theta)^2}{2!}[\hat{A},[\hat{A},\hat{B}]] + \frac{(i\theta)^3}{3!}[\hat{A},[\hat{A},[\hat{A},\hat{B}]]] + \cdots \tag{D.1}$$

Operators ($\hat{A}$)	$I_x^{12} - I_x^{23}$ ($\hat{B}$)
$I_x^{12} + I_x^{23}$	$cos\left(\frac{\theta}{\sqrt{2}}\right)[I_x^{12} - I_x^{23}] + \sqrt{2}sin\left(\frac{\theta}{\sqrt{2}}\right)[I_y^{13}]$
$I_y^{12} - I_y^{23}$	$cos\left(\frac{\theta}{\sqrt{2}}\right)[I_x^{12} - I_x^{23}] + \sqrt{2}sin\left(\frac{\theta}{\sqrt{2}}\right)[I_z^{13}]$
$I_y^{12} + I_y^{23}$	$cos(\sqrt{2}\theta)[I_x^{12} - I_x^{23}] + \frac{1}{\sqrt{2}}sin(\sqrt{2}\theta)[I_z^{12} - I_z^{23} - I_x^{13}]$
$I_z^{12} - I_z^{23}$	$cos\left(\frac{3\theta}{2}\right)[I_x^{12} - I_x^{23}] - sin\left(\frac{3\theta}{2}\right)[I_y^{12} + I_y^{23}]$
$I_z^{12} + I_z^{23}$	$cos\left(\frac{\theta}{2}\right)[I_x^{12} - I_x^{23}] - sin\left(\frac{\theta}{2}\right)[I_y^{12} - I_y^{23}]$
I_x^{13}	$cos\left(\frac{\theta}{2}\right)[I_x^{12} - I_x^{23}] + sin\left(\frac{\theta}{2}\right)[I_y^{12} + I_y^{23}]$
I_y^{13}	$cos\left(\frac{\theta}{2}\right)[I_x^{12} - I_x^{23}] - sin\left(\frac{\theta}{2}\right)[I_x^{12} + I_x^{23}]$
$I_z^{12} - I_z^{23} + I_x^{13}$	$cos(\theta)[I_x^{12} - I_x^{23}] - sin(\theta)[I_y^{12} + I_y^{23}]$

Operator ($\hat{A}$)	$I_x^{12} + I_x^{23}$ ($\hat{B}$)
$I_x^{12} - I_x^{23}$	$cos\left(\frac{\theta}{\sqrt{2}}\right)[I_x^{12} + I_x^{23}] - \sqrt{2}sin\left(\frac{\theta}{\sqrt{2}}\right)[I_y^{13}]$
$I_y^{12} - I_y^{23}$	$cos(\sqrt{2}\theta)[I_x^{12} + I_x^{23}] + \frac{1}{\sqrt{2}}sin(\sqrt{2}\theta)[I_z^{12} - I_z^{23} + I_x^{13}]$
$I_y^{12} + I_y^{23}$	$cos\left(\frac{\theta}{\sqrt{2}}\right)[I_x^{12} + I_x^{23}] + \sqrt{2}sin\left(\frac{\theta}{\sqrt{2}}\right)[I_z^{13}]$
$I_z^{12} - I_z^{23}$	$cos\left(\frac{3\theta}{2}\right)[I_x^{12} + I_x^{23}] - sin\left(\frac{3\theta}{2}\right)[I_y^{12} - I_y^{23}]$
$I_z^{12} + I_z^{23}$	$cos\left(\frac{\theta}{2}\right)[I_x^{12} + I_x^{23}] - sin\left(\frac{\theta}{2}\right)[I_y^{12} + I_y^{23}]$
I_x^{13}	$cos\left(\frac{\theta}{2}\right)[I_x^{12} + I_x^{23}] - sin\left(\frac{\theta}{2}\right)[I_y^{12} - I_y^{23}]$
I_y^{13}	$cos\left(\frac{\theta}{2}\right)[I_x^{12} + I_x^{23}] + sin\left(\frac{\theta}{2}\right)[I_x^{12} - I_x^{23}]$
$I_z^{12} - I_z^{23} + I_x^{13}$	$cos(2\theta)[I_x^{12} + I_x^{23}] - sin(2\theta)[I_y^{12} - I_y^{23}]$

Operator $(\hat{A})$	$I_y^{12} - I_y^{23}$ $(\hat{B})$
$I_x^{12} - I_x^{23}$	$cos\left(\frac{\theta}{\sqrt{2}}\right)[I_y^{12} - I_y^{23}] - \sqrt{2}sin\left(\frac{\theta}{\sqrt{2}}\right)[I_z^{13}]$
$I_x^{12} + I_x^{23}$	$cos(\sqrt{2}\theta)[I_y^{12} - I_y^{23}] - \frac{1}{\sqrt{2}}sin(\sqrt{2}\theta)[I_z^{12} - I_z^{23} + I_x^{13}]$
$I_y^{12} + I_y^{23}$	$cos\left(\frac{\theta}{\sqrt{2}}\right)[I_y^{12} - I_y^{23}] - \sqrt{2}sin\left(\frac{\theta}{\sqrt{2}}\right)[I_y^{13}]$
$I_z^{12} - I_z^{23}$	$cos\left(\frac{3\theta}{2}\right)[I_y^{12} - I_y^{23}] + sin\left(\frac{3\theta}{2}\right)[I_x^{12} + I_x^{23}]$
$I_z^{12} + I_z^{23}$	$cos\left(\frac{\theta}{2}\right)[I_y^{12} - I_y^{23}] + sin\left(\frac{\theta}{2}\right)[I_x^{12} - I_x^{23}]$
I_x^{13}	$cos\left(\frac{\theta}{2}\right)[I_y^{12} - I_y^{23}] + sin\left(\frac{\theta}{2}\right)[I_x^{12} + I_x^{23}]$
I_y^{13}	$cos\left(\frac{\theta}{2}\right)[I_y^{12} - I_y^{23}] + sin\left(\frac{\theta}{2}\right)[I_y^{12} + I_y^{23}]$
$I_z^{12} - I_z^{23} + I_x^{13}$	$cos(2\theta)[I_y^{12} - I_y^{23}] + sin(2\theta)[I_x^{12} + I_x^{23}]$

Operator $(\hat{A})$	$I_y^{12} + I_y^{23}$ $(\hat{B})$
$I_x^{12} - I_x^{23}$	$cos(\sqrt{2}\theta)\,[I_y^{12} + I_y^{23}] - \frac{1}{\sqrt{2}} sin(\sqrt{2}\theta)\,[I_z^{12} - I_z^{23} - I_x^{13}]$
$I_x^{12} + I_x^{23}$	$cos\left(\frac{\theta}{\sqrt{2}}\right)[I_y^{12} + I_y^{23}] - \sqrt{2} sin\left(\frac{\theta}{\sqrt{2}}\right)[I_z^{13}]$
$I_y^{12} - I_y^{23}$	$cos\left(\frac{\theta}{\sqrt{2}}\right)[I_y^{12} + I_y^{23}] + \sqrt{2} sin\left(\frac{\theta}{\sqrt{2}}\right)[I_y^{13}]$
$I_z^{12} - I_z^{23}$	$cos\left(\frac{3\theta}{2}\right)[I_y^{12} + I_y^{23}] + sin\left(\frac{3\theta}{2}\right)[I_x^{12} - I_x^{23}]$
$I_z^{12} + I_z^{23}$	$cos\left(\frac{\theta}{2}\right)[I_y^{12} + I_y^{23}] + sin\left(\frac{\theta}{2}\right)[I_x^{12} + I_x^{23}]$
I_x^{13}	$cos\left(\frac{\theta}{2}\right)[I_y^{12} + I_y^{23}] - sin\left(\frac{\theta}{2}\right)[I_x^{12} - I_x^{23}]$
I_y^{13}	$cos\left(\frac{\theta}{2}\right)[I_y^{12} + I_y^{23}] - sin\left(\frac{\theta}{2}\right)[I_y^{12} - I_y^{23}]$
$I_z^{12} - I_z^{23} + I_x^{13}$	$cos(\theta)\,[I_y^{12} + I_y^{23}] + sin(\theta)\,[I_x^{12} - I_x^{23}]$

Operator $(\hat{A})$	$I_z^{12} - I_z^{23}$ $(\hat{B})$
$I_x^{12} - I_x^{23}$	$\frac{1+3cos(\sqrt{2}\theta)}{4}\left[I_z^{12} - I_z^{23}\right] + \frac{3}{2\sqrt{2}}sin(\sqrt{2}\theta)\left[I_y^{12} + I_y^{23}\right]$ $+\frac{3}{4}(1 - cos(\sqrt{2}\theta))\left[I_x^{13}\right]$
$I_x^{12} + I_x^{23}$	$\frac{1+3cos(\sqrt{2}\theta)}{4}\left[I_z^{12} - I_z^{23}\right] + \frac{3}{2\sqrt{2}}sin(\sqrt{2}\theta)\left[I_y^{12} - I_y^{23}\right]$ $+\frac{3}{4}(cos(\sqrt{2}\theta) - 1)\left[I_x^{13}\right]$
$I_y^{12} - I_y^{23}$	$\frac{1+3cos(\sqrt{2}\theta)}{4}\left[I_z^{12} - I_z^{23}\right] - \frac{3}{2\sqrt{2}}sin(\sqrt{2}\theta)\left[I_x^{12} + I_x^{23}\right]$ $+\frac{3}{4}(cos(\sqrt{2}\theta) - 1)\left[I_x^{13}\right]$
$I_y^{12} + I_y^{23}$	$\frac{1+3cos(\sqrt{2}\theta)}{4}\left[I_z^{12} - I_z^{23}\right] - \frac{3}{2\sqrt{2}}sin(\sqrt{2}\theta)\left[I_x^{12} - I_x^{23}\right]$ $+\frac{3}{4}(1 - cos(\sqrt{2}\theta))\left[I_x^{13}\right]$
I_z^{13}	$\left[I_z^{12} - I_z^{23}\right]$
I_x^{13}	$\left[I_z^{12} - I_z^{23}\right]$
I_y^{13}	$\left[I_z^{12} - I_z^{23}\right]$
$I_z^{12} - I_z^{23} + I_x^{13}$	$\left[I_z^{12} - I_z^{23}\right]$

Operator ($\hat{A}$)	I_z^{13} ($\hat{B}$)
$I_x^{12} - I_x^{23}$	$cos\left(\frac{\theta}{\sqrt{2}}\right)[I_z^{13}] + \frac{1}{\sqrt{2}} sin\left(\frac{\theta}{\sqrt{2}}\right)[I_y^{12} - I_y^{23}]$
$I_x^{12} + I_x^{23}$	$cos\left(\frac{\theta}{\sqrt{2}}\right)[I_z^{13}] + \frac{1}{\sqrt{2}} sin\left(\frac{\theta}{\sqrt{2}}\right)[I_y^{12} + I_y^{23}]$
$I_y^{12} - I_y^{23}$	$cos\left(\frac{\theta}{\sqrt{2}}\right)[I_z^{13}] - \frac{1}{\sqrt{2}} sin\left(\frac{\theta}{\sqrt{2}}\right)[I_x^{12} - I_x^{23}]$
$I_y^{12} + I_y^{23}$	$cos\left(\frac{\theta}{\sqrt{2}}\right)[I_z^{13}] - \frac{1}{\sqrt{2}} sin\left(\frac{\theta}{\sqrt{2}}\right)[I_x^{12} + I_x^{23}]$
$I_z^{12} - I_z^{23}$	I_z^{13}
I_x^{13}	$cos(\theta)\, I_z^{13} + sin(\theta)\, I_y^{13}$
I_y^{13}	$cos(\theta)\, I_z^{13} - sin(\theta)\, I_x^{13}$
$I_z^{12} - I_z^{23} + I_x^{13}$	$cos(\theta)\, I_z^{13} + sin(\theta)\, I_y^{13}$

Operator ($\hat{A}$)	I_x^{13} ($\hat{B}$)
$I_x^{12} - I_x^{23}$	$\frac{3+cos(\sqrt{2}\theta)}{4}\,[I_x^{13}] - \frac{1}{2\sqrt{2}}sin(\sqrt{2}\theta)\,[I_y^{12} + I_y^{23}]$ $+\frac{1}{4}(1 - cos(\sqrt{2}\theta))\,[I_z^{12} - I_z^{23}]$
$I_x^{12} + I_x^{23}$	$\frac{3+cos(\sqrt{2}\theta)}{4}\,[I_x^{13}] + \frac{1}{2\sqrt{2}}sin(\sqrt{2}\theta)\,[I_y^{12} - I_y^{23}]$ $-\frac{1}{4}(1 - cos(\sqrt{2}\theta))\,[I_z^{12} - I_z^{23}]$
$I_y^{12} - I_y^{23}$	$\frac{3+cos(\sqrt{2}\theta)}{4}\,[I_x^{13}] - \frac{1}{2\sqrt{2}}sin(\sqrt{2}\theta)\,[I_x^{12} + I_x^{23}]$ $-\frac{1}{4}(1 - cos(\sqrt{2}\theta))\,[I_z^{12} - I_z^{23}]$
$I_y^{12} + I_y^{23}$	$\frac{3+cos(\sqrt{2}\theta)}{4}\,[I_x^{13}] + \frac{1}{2\sqrt{2}}sin(\sqrt{2}\theta)\,[I_x^{12} - I_x^{23}]$ $+\frac{1}{4}(1 - cos(\sqrt{2}\theta))\,[I_z^{12} - I_z^{23}]$
$I_z^{12} - I_z^{23}$	I_x^{13}
I_z^{13}	$cos(\theta)\, I_x^{13} - sin(\theta)\, I_y^{13}$
I_y^{13}	$cos(\theta)\, I_x^{13} + sin(\theta)\, I_z^{13}$
$I_z^{12} - I_z^{23} + I_x^{13}$	I_x^{13}

Operator ($\hat{A}$)	I_y^{13} ($\hat{B}$)
$I_x^{12} - I_x^{23}$	$cos\left(\frac{\theta}{\sqrt{2}}\right)[I_y^{13}] + \frac{1}{\sqrt{2}} sin\left(\frac{\theta}{\sqrt{2}}\right)[I_x^{12} + I_x^{23}]$
$I_x^{12} + I_x^{23}$	$cos\left(\frac{\theta}{\sqrt{2}}\right)[I_y^{13}] - \frac{1}{\sqrt{2}} sin\left(\frac{\theta}{\sqrt{2}}\right)[I_x^{12} - I_x^{23}]$
$I_y^{12} - I_y^{23}$	$cos\left(\frac{\theta}{\sqrt{2}}\right)[I_y^{13}] - \frac{1}{\sqrt{2}} sin\left(\frac{\theta}{\sqrt{2}}\right)[I_y^{12} + I_y^{23}]$
$I_y^{12} + I_y^{23}$	$cos\left(\frac{\theta}{\sqrt{2}}\right)[I_y^{13}] + \frac{1}{\sqrt{2}} sin\left(\frac{\theta}{\sqrt{2}}\right)[I_y^{12} - I_y^{23}]$
$I_z^{12} - I_z^{23}$	I_y^{13}
I_z^{13}	$cos(\theta)\, I_y^{13} + sin(\theta)\, I_x^{13}$
I_x^{13}	$cos(\theta)\, I_y^{13} - sin(\theta)\, I_z^{13}$
$I_z^{12} - I_z^{23} + I_x^{13}$	$cos(\theta)\, I_y^{13} - sin(\theta)\, I_z^{13}$

Operator ($\hat{A}$)	$I_z^{12} - I_z^{23} + I_x^{13}$ ($\hat{B}$)
$I_x^{12} - I_x^{23}$	$\frac{1+cos(\sqrt{2}\theta)}{2}\left[I_z^{12} - I_z^{23}\right] + \frac{1}{\sqrt{2}}sin(\sqrt{2}\theta)\left[I_y^{12} + I_y^{23}\right]$ $+\frac{1}{2}(3 - cos(\sqrt{2}\theta))\left[I_x^{13}\right]$
$I_x^{12} + I_x^{23}$	$cos(\sqrt{2}\theta)\left[I_z^{12} - I_z^{23} + I_x^{13}\right] + \sqrt{2}sin(\sqrt{2}\theta)\left[I_y^{12} - I_y^{23}\right]$
$I_y^{12} - I_y^{23}$	$cos(\sqrt{2}\theta)\left[I_z^{12} - I_z^{23} + I_x^{13}\right] - \sqrt{2}sin(\sqrt{2}\theta)\left[I_x^{12} + I_x^{23}\right]$
$I_y^{12} + I_y^{23}$	$\frac{1+cos(\sqrt{2}\theta)}{2}\left[I_z^{12} - I_z^{23}\right] - \frac{1}{\sqrt{2}}sin(\sqrt{2}\theta)\left[I_x^{12} - I_x^{23}\right]$ $+\frac{1}{2}(3 - cos(\sqrt{2}\theta))\left[I_x^{13}\right]$
$I_z^{12} - I_z^{23}$	$I_z^{12} - I_z^{23} + I_x^{13}$
$I_z^{12} + I_z^{23}$	$\left[I_z^{12} - I_z^{23}\right] - sin(\theta)\, I_y^{13} + cos(\theta)\, I_x^{13}$
I_x^{13}	$I_z^{12} - I_z^{23} + I_x^{13}$
I_y^{13}	$\left[I_z^{12} - I_z^{23}\right] + sin(\theta)\, I_z^{13} + cos(\theta)\, I_x^{13}$

Appendix E

Description of Double-quantum (DQ) excitation using FME - Normal Boundary Condition ($\Lambda(0) = 0$)

In the normal boundary condition, $\Lambda(0)$ is set to zero and the time-propagator reduces to a simpler form given below.

$$U(t,0) = e^{-i\Lambda(t)}e^{-i\bar{H}t} \tag{E.1}$$

Accordingly, the expansion terms in $\bar{H}$ and $\Lambda(t)$ are derived (refer to Table E.1). In the present calculations, we confine ourselves to second order in $\bar{H}$.

$$\begin{aligned}\bar{H} &= \bar{H}^{(1)} + \bar{H}^{(2)} \\ &= \sqrt{2}\omega_1 J_0(A)\left[I_X^{12} + I_X^{23}\right] - \frac{2\omega_1^2}{\omega_r} J_0(A)\left[\sum_{n=2p-1}\frac{J_n(A)}{n}\right]\left[I_Z^{12} - I_Z^{23} + I_X^{13}\right]\end{aligned} \tag{E.2}$$

where $p \in \mathbb{N}$ (natural numbers, e.g. 1,2,3,....).

To maintain consistency, both the initial density operator ($\rho(0) = 2I_Z^{13}$) and detection operator ($D = I_+^{13}$) are transformed by U_1.

$$\widetilde{\rho}(0) = U_1\rho(0)U_1^{-1} = 2I_Z^{13} \;\; ; \;\; \widetilde{D} = U_1 D U_1^{-1} = I_+^{13} \tag{E.3}$$

Subsequently, employing the time-propagator ($U(t,0)$), the double-quantum signal is evaluated as given below.

$$S(t) = Tr\left[e^{-i\Lambda(t)}e^{-i\bar{H}t}\widetilde{\rho}(0)e^{i\bar{H}t}e^{i\Lambda(t)}.\widetilde{D}\right] = Tr\left[e^{-i\bar{H}t}\widetilde{\rho}(0)e^{i\bar{H}t}.e^{i\Lambda(t)}\widetilde{D}e^{-i\Lambda(t)}\right] \tag{E.4}$$

General Expression	Coefficients and Operators
$\bar{H}^{(1)} = H_0$	$\sqrt{2}\omega_1 J_0(A)\left[I_X^{12} + I_X^{23}\right]$
$\bar{H}^{(2)} = \sum\limits_{k\neq 0}\left\{\dfrac{[H_k, H_{-k}]}{2k\omega}\right\} + \sum\limits_{k\neq 0}\left\{\dfrac{[H_0, H_k]}{k\omega}\right\}$	$-\dfrac{2\omega_1^2}{\omega_r}J_0(A)\left[\sum\limits_{n=2p-1}\dfrac{J_n(A)}{n}\right]\left[I_Z^{12} - I_Z^{23} + I_X^{13}\right]$
$\Lambda_1(t) = \sum\limits_{k\neq 0}\dfrac{e^{ik\omega t}-1}{ik\omega}H_k$	$a(t)\left[I_Y^{12} - I_Y^{23}\right] + b(t)\left[I_X^{12} + I_X^{23}\right]$
$a(t) = \dfrac{\sqrt{2}\omega_1}{\omega_r}\left[\sum\limits_{n=2p-1}\dfrac{J_n(A)}{n}\left[\cos(2n\omega_r t) - 1\right]\right]$	$b(t) = \dfrac{\sqrt{2}\omega_1}{\omega_r}\sum\limits_{n=2p}\dfrac{J_n(A)}{n}\sin(2n\omega_r t)$

Table E.1: Generalized expressions for $\bar{H}$ and $\Lambda(t)$ in the FME scheme (MAS case) corresponding to the normal boundary condition ($\Lambda(0) = 0$)

Analogous to the transformation employed in the AHT calculations (refer to Eq. 2.64), the Hamiltonian $\bar{H}$ is transformed (using $U_2 = e^{\frac{i\theta[I_Y^{12} - I_Y^{23}]}{\sqrt{2}}}$, $\tan\theta = \dfrac{\omega_1 J_0(A)}{-\dfrac{2\omega_1^2 J_0(A)}{\omega_r}\left[\sum\limits_{n=2p-1}\dfrac{J_n(A)}{n}\right]}$) such that the Hamiltonian reduces to a simpler form comprising commuting set of operators.

$$\begin{aligned} H_{eff} = U_2\bar{H}U_2^{-1} &= \left\{\omega_1 J_0(A)\sin\theta - \frac{2\omega_1^2}{\omega_r}J_0(A)\left[\sum_{n=2p-1}\frac{J_n(A)}{n}\right]\cos\theta\right\}\left[I_Z^{12} - I_Z^{23} + I_X^{13}\right] \\ &= \omega_e\left[I_Z^{12} - I_Z^{23} + I_X^{13}\right] \end{aligned} \tag{E.5}$$

Accordingly, the final signal expression reduces to the following form.

$$\begin{aligned} S(t) &= Tr\left[\underbrace{U_2 e^{-i\bar{H}t}U_2^{-1}}_{e^{-iH_{eff}t}}\overbrace{U_2\tilde{\rho}(0)U_2^{-1}}^{\widetilde{\rho}_{eff}(0)}\underbrace{U_2 e^{i\bar{H}t}U_2^{-1}}_{e^{iH_{eff}t}}.\overbrace{U_2 e^{i\Lambda(t)}\widetilde{D}e^{-i\Lambda(t)}U_2^{-1}}^{\widetilde{D}_{eff}(t)}\right] \\ &= Tr\left[\underbrace{e^{-iH_{eff}t}\widetilde{\rho}_{eff}(0)e^{iH_{eff}t}}_{\widetilde{\rho}_{eff}(t)}.\widetilde{D}_{eff}(t)\right] = Tr\left[\widetilde{\rho}_{eff}(t)\widetilde{D}_{eff}(t)\right] \end{aligned} \tag{E.6}$$

Employing Baker Campbell Hausdorff (BCH) formula [52], analytic expressions for the

operators $\widetilde{\rho}_{eff}(0)$, $\widetilde{\rho}_{eff}(t)$ and $\widetilde{D}_{eff}(t)$ are derived and described in detail in Table E.2.

$$\widetilde{\rho}_{eff}(0) = U_2\widetilde{\rho}(0)U_2^{-1} = \sum C_\alpha^{ij} I_\alpha^{ij} = \left\{2\cos\left(\frac{\theta}{2}\right)\right\}\left[I_Z^{13}\right] + \left\{-\sqrt{2}\sin\left(\frac{\theta}{2}\right)\right\}\left[I_X^{12} - I_X^{23}\right] \tag{E.7}$$

$$\begin{aligned}\widetilde{\rho}_{eff}(t) &= e^{-iH_{eff}t}\widetilde{\rho}_{eff}(0)e^{iH_{eff}t} = \sum R_\alpha^{ij}(t) I_\alpha^{ij} \\ &= \left\{2\cos\left(\frac{\theta}{2}\right)\cos\left(\omega_e t\right)\right\}\left[I_Z^{13}\right] + \left\{-2\cos\left(\frac{\theta}{2}\right)\sin\left(\omega_e t\right)\right\}\left[I_Y^{13}\right] \\ &+ \left\{-\sqrt{2}\sin\left(\frac{\theta}{2}\right)\cos\left(\omega_e t\right)\right\}\left[I_X^{12} - I_X^{23}\right] + \left\{-\sqrt{2}\sin\left(\frac{\theta}{2}\right)\sin\left(\omega_e t\right)\right\}\left[I_Y^{12} + I_Y^{23}\right]\end{aligned} \tag{E.8}$$

$$\widetilde{D}_{eff}(t) = U_2 e^{i\Lambda(t)}\widetilde{D}e^{-i\Lambda(t)}U_2^{-1} = \sum D_\alpha^{ij}(t) I_\alpha^{ij} \tag{E.9}$$

Subsequently, the final signal (corresponding to DQ excitation) reduces to a form, comprising centre-band and sidebands.

$$S(t) = \sum R_\alpha^{ij}(t) D_\beta^{ji}(t) = F_0 e^{\pm i\omega_e t} + \sum_{p\in\mathbb{N}} F_p e^{\pm i(\omega_e \pm 2p\omega_r)t} \tag{E.10}$$

where F_0 and F_p represent the amplitudes of centreband and p^{th} sideband respectively.

To verify the exactness of the above framework, analytic simulations (based on Eq. E.10) were compared with simulation results emerging from SPINEVOLUTION. As depicted in Figure E.1, the analytic simulations from the FME approach are in excellent agreement to those obtained from numerical methods.

operators	Initial Density Operator, C_α^{ij}	Detection Operator, $D_\alpha^{ij}(t)$	Density Operator, $R_\alpha^{ij}(t)$
I_Z^{13}	$2\cos\left(\frac{\theta}{2}\right)$	$-\frac{i}{\sqrt{2}}b(t)\sin\left(\frac{\theta}{2}\right)$	$2\cos\left(\frac{\theta}{2}\right)\cos\left(\omega_e t\right)$
I_+^{12}	$-\frac{1}{\sqrt{2}}\sin\left(\frac{\theta}{2}\right)$	$\frac{1}{2\sqrt{2}}\sin\left(\frac{\theta}{2}\right)[1-c(t)]+\frac{3}{4\sqrt{2}}c(t)\sin\left(\theta\right)-\frac{1}{2}a(t)\cos\left(\frac{\theta}{2}\right)-\frac{i}{2}b(t)\cos\left(\frac{\theta}{2\sqrt{2}}\right)$	$-\frac{1}{\sqrt{2}}\sin\left(\frac{\theta}{2}\right)e^{-i\omega_e t}$
I_-^{21}	$-\frac{1}{\sqrt{2}}\sin\left(\frac{\theta}{2}\right)$	$\frac{3}{2\sqrt{2}}\sin\left(\frac{\theta}{2}\right)[1-c(t)]+\frac{3}{4\sqrt{2}}c(t)\sin\left(\theta\right)-\frac{i}{2}b(t)\left[\cos\left(\frac{\theta}{2\sqrt{2}}\right)-1\right]$	$-\frac{1}{\sqrt{2}}\sin\left(\frac{\theta}{2}\right)e^{i\omega_e t}$
I_+^{23}	$\frac{1}{\sqrt{2}}\sin\left(\frac{\theta}{2}\right)$	$\frac{1}{2\sqrt{2}}\sin\left(\frac{\theta}{2}\right)[1-c(t)]+\frac{3}{4\sqrt{2}}c(t)\sin\left(\theta\right)-\frac{1}{2}a(t)\cos\left(\frac{\theta}{2}\right)+\frac{i}{2}b(t)\cos\left(\frac{\theta}{2\sqrt{2}}\right)$	$\frac{1}{\sqrt{2}}\sin\left(\frac{\theta}{2}\right)e^{i\omega_e t}$
I_-^{32}	$\frac{1}{\sqrt{2}}\sin\left(\frac{\theta}{2}\right)$	$\frac{3}{2\sqrt{2}}\sin\left(\frac{\theta}{2}\right)[1-c(t)]+\frac{3}{4\sqrt{2}}c(t)\sin\left(\theta\right)+\frac{i}{2}b(t)\left[\cos\left(\frac{\theta}{2\sqrt{2}}\right)-1\right]$	$\frac{1}{\sqrt{2}}\sin\left(\frac{\theta}{2}\right)e^{-i\omega_e t}$
I_+^{13}	0	$\frac{3}{2}\left[\frac{5}{3}\cos\left(\frac{\theta}{2}\right)-1\right][1-c(t)]-\frac{3}{8}c(t)\left[\cos\left(\theta\right)-1\right]-\frac{1}{\sqrt{2}}a(t)\sin\left(\frac{\theta}{2}\right)$	$i\cos\left(\frac{\theta}{2}\right)\sin\left(\omega_e t\right)$
I_-^{31}	0	$\frac{3}{2}\left[\cos\left(\frac{\theta}{2}\right)-1\right][1-c(t)]-\frac{3}{8}c(t)\left[\cos\left(\theta\right)-1\right]$	$-i\cos\left(\frac{\theta}{2}\right)\sin\left(\omega_e t\right)$
	$c(t)=\frac{1}{4}\left[a^2(t)+b^2(t)\right]$	$\omega_e=\omega_1 J_0\left(A\right)\sin\theta-\frac{2\omega_1^2}{\omega_r}J_0\left(A\right)\left[\sum_{n=2p-1}\frac{J_n\left(A\right)}{n}\right]\cos\theta$	

Table E.2: Definition of constants employed in the description of the density operator and detection operator (Eq. E.7-E.9) based on the FME ($\Lambda(0)=0$)

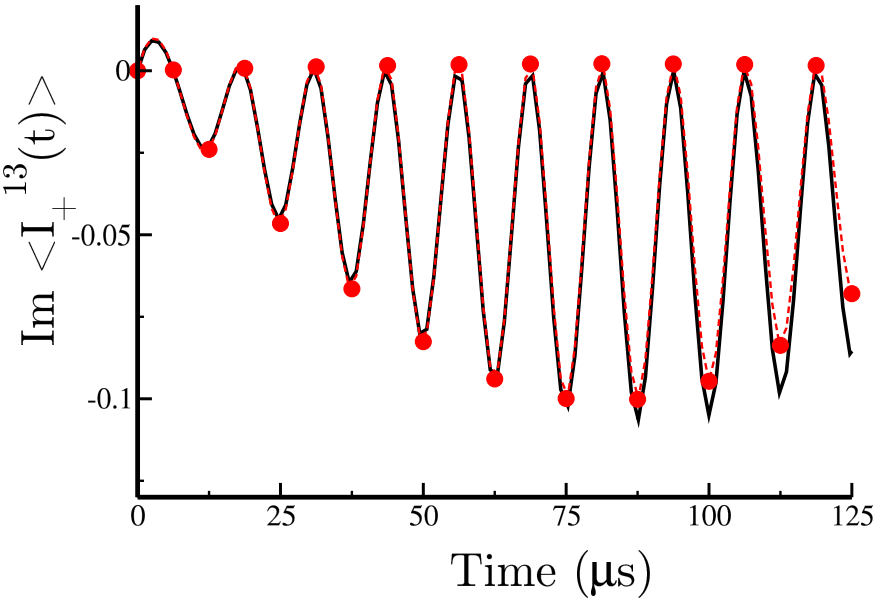

Figure E.1: In the MAS simulations depicted, excitation of DQ transition in spin I=1 system is presented. The validity of FME scheme ($\Lambda(0) = 0$, indicated by red dots) is compared with numerical simulations based on SPINEVOLUTION [7] (solid black line). The following parameters were employed in the simulations: $C_Q = 1$ MHz, $\eta = 1.0$, $\nu_r = 40$ kHz and RF amplitude, $\nu_1 = 10$ kHz.

In the FME approach based on the normal boundary condition, the transformed initial density operator, $\widetilde{\rho}_{eff}(0)$ (refer to Eq. E.7 in Appendix-E) comprises both the longitudinal (I_Z^{13} operator) and transverse operators (I_X^{12}, I_X^{23}). The longitudinal components are proportional to $\cos\left(\frac{\theta}{2}\right)$, while, the transverse components are proportional to $\sin\left(\frac{\theta}{2}\right)$. In contrast to the alternate boundary condition ($\Lambda(0) \neq 0$), the longitudinal component (associated with I_Z^{13} operator) in $\widetilde{\rho}_{eff}(0)$ is transformed into DQ coherence (refer to Eq. E.8 in Appendix-E) through the DQ operator (I_X^{13}) present in the evolution operator, $e^{-i\bar{H}t}$. As illustrated in Eq. E.8, the DQ coherence (I_Y^{13}) is proportional to $\cos\left(\frac{\theta}{2}\right)$ leading to improved excitation efficiency at higher RF amplitudes. While the analytic simulations depicted in Figure E.1 are in good agreement with numerical simulations, the analytic expressions in the proposed framework are less insightful in explaining the loss of signal intensity at odd integral multiples of $\frac{\tau_r}{4}$. Hence, the analytic expressions obtained from FME (alternate boundary condition, $\Lambda \neq 0$) present an attractive option for studying the excitation process in spin-1 system.

Appendix F

Description of spin dynamics in the RF interaction frame

1. Static simulations

Following the description in the chapter, the Hamiltonian of an isolated spin-1 system (static case) in the rotating frame is represented by the following equation.

$$H = \frac{\omega_Q}{3}\left[I_Z^{12} - I_Z^{23}\right] + \sqrt{2}\omega_1\left[I_X^{12} + I_X^{23}\right] \tag{F.1}$$

When the magnitude of the RF field exceeds the quadrupole frequency, the Hamiltonian in the rotating frame is transformed (employing the unitary transformation, $U_1 = e^{i\frac{\pi\sqrt{2}}{2}[I_Y^{12}+I_Y^{23}]}$) such that the RF part is quantized along Z-direction.

$$\widetilde{H} = U_1 H U_1^{-1} = -\frac{\omega_Q}{6}\left[I_Z^{12} - I_Z^{23}\right] + \frac{\omega_Q}{2}I_X^{13} + 2\omega_1 I_Z^{13} \tag{F.2}$$

Subsequently, the Hamiltonian is additionally transformed into the dominant interaction frame (defined by the RF interaction), $U_2 = e^{2i\omega_1 t I_Z^{13}}$. In the RF interaction frame, the Hamiltonian is time-dependent (modulated by RF amplitude, ω_1).

$$\widetilde{\widetilde{H}}(t) = U_2\widetilde{H}U_2^{-1} = -\frac{\omega_Q}{6}\left[I_Z^{12} - I_Z^{23}\right] + \frac{\omega_Q}{4}\left[I_+^{13}e^{2i\omega_1 t} + I_-^{31}e^{-2i\omega_1 t}\right] \tag{F.3}$$

Below, we present a brief description of the derivation of time-propagators based on effective Floquet Hamiltonians and Floquet Magnus expansion.

(i) Derivation of time-propagators based on effective Floquet Hamiltonians

Employing Floquet theory, the time-dependent Hamiltonian in the RF interaction frame is transformed into a time-independent Floquet Hamiltonian.

$$H_F = \omega_1 I_F - \frac{\omega_Q}{6}\left[I_Z^{12} - I_Z^{23}\right]_0 + \frac{\omega_Q}{4}\left\{\left[I_+^{13}\right]_2 + \left[I_-^{31}\right]_{-2}\right\} \tag{F.4}$$

To simplify the description in the extended space, the contact transformation procedure is employed. Accordingly, the Floquet Hamiltonian is split and expressed as a sum of zero-order and perturbing Hamiltonian.

$$H_0 = \omega_1 I_F - \frac{\omega_Q}{6}\left[I_Z^{12} - I_Z^{23}\right]_0 \tag{F.5}$$

$$H_1 = \frac{\omega_Q}{4}\left\{\left[I_+^{13}\right]_2 + \left[I_-^{31}\right]_{-2}\right\} \tag{F.6}$$

Employing the transformation function, S_1, the Floquet Hamiltonian is transformed as given below.

$$H_F^{eff} = e^{i\lambda S_1} H_F e^{-i\lambda S_1} \;\; ; \;\; S_1 = i\left(C_{13}^{(2)}\left[I_+^{13}\right]_2 + C_{31}^{(-2)}\left[I_-^{31}\right]_{-2}\right) \tag{F.7}$$

To second order, the diagonal corrections to the effective Hamiltonian is derived and represented by the following equation.

$$H_F^{eff} = H_0 + H_2^{(1)} = \omega_1 I_F - \frac{\omega_Q}{6}\left[I_Z^{12} - I_Z^{23}\right]_0 + \frac{\omega_Q^2}{16\omega_1}\left[I_Z^{13}\right]_0 \tag{F.8}$$

Following the standard procedure, both the initial density operator and density operators are transformed and the final time-domain signal is summarized by the following equations.

$$\widetilde{\rho}(0) = e^{i\lambda S_1} U_2 U_1 \rho(0) U_1^{-1} U_2^{-1} e^{-i\lambda S_1} = \sum_p C_\alpha^{ij(p)}\left[I_\alpha^{ij}\right]_p \tag{F.9}$$

$$\widetilde{\rho}(t) = e^{-iH_F^{eff}t}\widetilde{\rho}(0)e^{iH_F^{eff}t} = \sum_p R_\alpha^{ij(p)}(t)\left[I_\alpha^{ij}\right]_p \tag{F.10}$$

$$\widetilde{D} = e^{i\lambda S_1} U_2 U_1 D U_1^{-1} U_2^{-1} e^{-i\lambda S_1} = \sum_p D_\alpha^{ij(p)}\left[I_\alpha^{ij}\right]_p \tag{F.11}$$

$$\begin{aligned} S(t) &= Tr\left[\widetilde{\rho}(t)\widetilde{D}\right] = \sum_p R_\alpha^{ij(p)}(t) D_\beta^{ji(-p)} \\ &= C_+^{12(1)} D_-^{21(-1)} e^{-i\omega_1 t} e^{-\frac{i\omega_Q^2 t}{32\omega_1}} e^{\frac{i\omega_Q t}{4}} + C_-^{21(-1)} D_+^{12(1)} e^{i\omega_1 t} e^{\frac{i\omega_Q^2 t}{32\omega_1}} e^{-\frac{i\omega_Q t}{4}} \\ &+ C_+^{23(1)} D_-^{32(-1)} e^{-i\omega_1 t} e^{-\frac{i\omega_Q^2 t}{32\omega_1}} e^{-\frac{i\omega_Q t}{4}} + C_-^{32(-1)} D_+^{23(1)} e^{i\omega_1 t} e^{\frac{i\omega_Q^2 t}{32\omega_1}} e^{\frac{i\omega_Q t}{4}} \end{aligned} \tag{F.12}$$

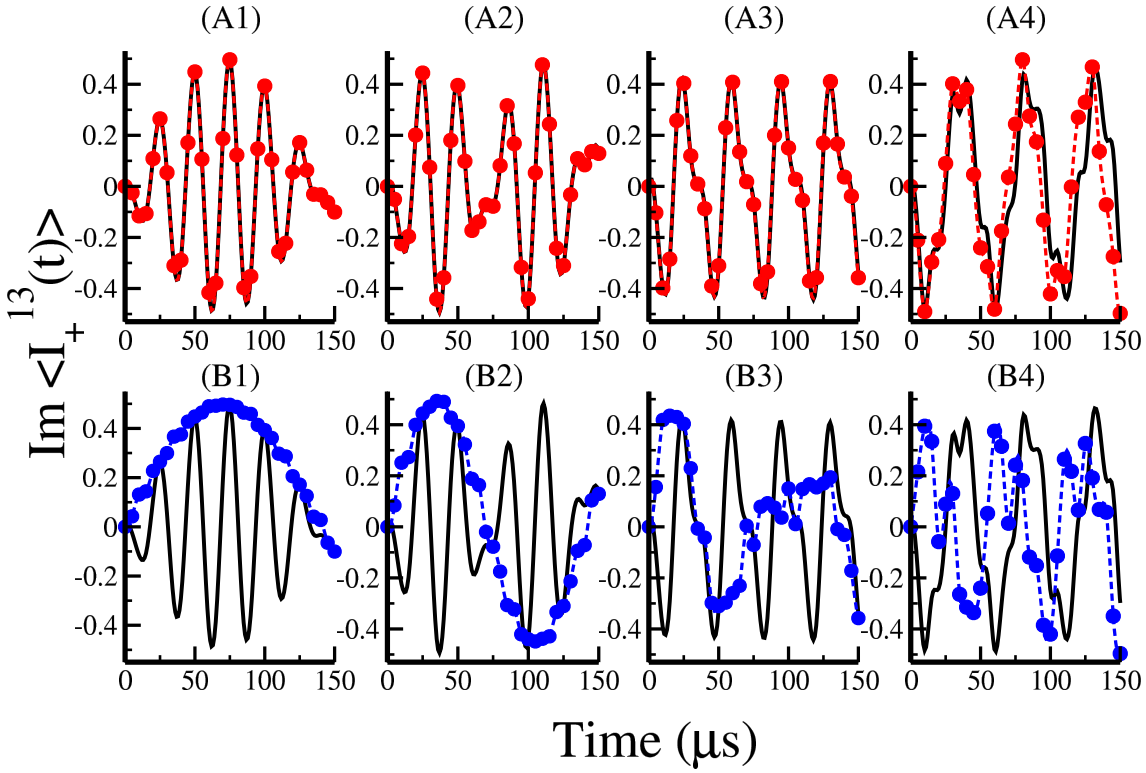

Figure F.1: In the simulations depicted (static case), the validity of the Floquet Contact Scheme and Floquet Magnus expansion scheme is checked by varying the Quadrupolar coupling constant, C_Q. The analytic simulations based on Floquet Contact transformation (dotted red line based on Eq. F.12) and Floquet Magnus expansion scheme (dotted blue line based on Eq. F.17) are compared with those obtained from exact numerical methods based on SPINEVOLUTION [7] (solid black line). The RF amplitude is kept fixed at $\nu_1 = 40$ kHz while the C_Q is varied as- (A1, B1) 25 kHz (A2, B2) 50 kHz (A3, B3) 100 kHz (A4, B4) 200 kHz.

A detailed description of the coefficients employed in the operators is summarised in Table F.1. As depicted in Figure F.1 (first row), the analytic simulations (based on Eq. F.12) are in excellent agreement with those obtained from numerical simulations and justify the framework outlined above.

operators	Initial Density Operator, $C_\alpha^{ij(p)}$	Detection Operator, $D_\alpha^{ij(p)}$	Density Operator, $R_\alpha^{ij(p)}(t)$
$[I_+^{12}]_1$	$-\frac{1}{\sqrt{2}}\left[1-x-\frac{x^2}{2}\right]$	$\frac{5}{2\sqrt{2}}\left[1-\frac{x^2}{2}\right]+\frac{3}{2\sqrt{2}}x$	$-\frac{1}{\sqrt{2}}\left[1-x-\frac{x^2}{2}\right]e^{-i\omega_1 t}e^{-i\omega_e^{(1)}t}e^{i\omega_e^{(2)}t}$
$[I_-^{21}]_{-1}$	$-\frac{1}{\sqrt{2}}\left[1-x-\frac{x^2}{2}\right]$	$\frac{3}{2\sqrt{2}}\left[1-\frac{x^2}{2}\right]+\frac{5}{2\sqrt{2}}x$	$-\frac{1}{\sqrt{2}}\left[1-x-\frac{x^2}{2}\right]e^{i\omega_1 t}e^{i\omega_e^{(1)}t}e^{-i\omega_e^{(2)}t}$
$[I_+^{23}]_1$	$-\frac{1}{\sqrt{2}}\left[1+x-\frac{x^2}{2}\right]$	$-\frac{5}{2\sqrt{2}}\left[1-\frac{x^2}{2}\right]+\frac{3}{2\sqrt{2}}x$	$-\frac{1}{\sqrt{2}}\left[1+x-\frac{x^2}{2}\right]e^{-i\omega_1 t}e^{-i\omega_e^{(1)}t}e^{-i\omega_e^{(2)}t}$
$[I_-^{32}]_{-1}$	$-\frac{1}{\sqrt{2}}\left[1+x-\frac{x^2}{2}\right]$	$-\frac{3}{2\sqrt{2}}\left[1-\frac{x^2}{2}\right]+\frac{5}{2\sqrt{2}}x$	$-\frac{1}{\sqrt{2}}\left[1+x-\frac{x^2}{2}\right]e^{i\omega_1 t}e^{i\omega_e^{(1)}t}e^{i\omega_e^{(2)}t}$
	$C_{13}^{(2)}=-C_{31}^{(-2)}=x=-\frac{\omega_Q}{8\omega_1}$	$\omega_e^{(1)}=\frac{\omega_Q^2}{32\omega_1}$	$\omega_e^{(2)}=\frac{\omega_Q}{4}$

Table F.1: Definition of constants employed in the description of the density operator and detection operator (Eq. F.9-F.11) based on the Floquet Contact Transformation (static case)

(ii) Derivation of time-propagators based on Floquet Magnus Expansion (Alternate boundary condition)

Based on the discussion in the chapter, the time-propagator in the RF interaction frame is derived and described by the following equations.

$$U(t) = e^{-i\Lambda(t)}e^{-i\bar{H}t}e^{i\Lambda(0)} \tag{F.13}$$

Subsequently, based on the general expressions given in Table 2.2 (Chapter-2), the expansion coefficients in $\bar{H}$ and $\Lambda(t)$ are derived and given below.

$$\bar{H} = \bar{H}^{(1)} + \bar{H}^{(2)} = -\frac{\omega_Q}{6}\left[I_Z^{12} - I_Z^{23}\right] + \frac{\omega_Q^2}{16\omega_1}I_Z^{13} \tag{F.14}$$

$$\Lambda_1(t) = \frac{\omega_Q}{4\omega_1}\cos\left(2\omega_1 t\right)I_Y^{13} + \frac{\omega_Q}{4\omega_1}\sin\left(2\omega_1 t\right)I_X^{13} = a(t)I_Y^{13} + b(t)I_X^{13} \tag{F.15}$$

In accord with the description in the chapter, the final signal expression is derived and represented by the following equations.

$$S(t) = Tr\left[e^{-i\Lambda(t)}e^{-i\bar{H}t}e^{i\Lambda(0)}\rho(0)e^{-i\Lambda(0)}e^{i\bar{H}t}e^{i\Lambda(t)}.D\right] = Tr\left[e^{-i\bar{H}t}e^{i\Lambda(0)}\rho(0)e^{-i\Lambda(0)}e^{i\bar{H}t}.e^{i\Lambda(t)}De^{-i\Lambda(t)}\right] \tag{F.16}$$

$$\begin{aligned} S(t) &= Tr\left[\widetilde{\rho}(t)\widetilde{D}\right] = \sum_p R_\alpha^{ij}(t)D_\alpha^{ji} \\ &= C_+^{12}D_-^{21}e^{-\frac{i\omega_Q^2 t}{32\omega_1}}e^{\frac{i\omega_Q t}{4}} + C_-^{21}D_+^{12}e^{\frac{i\omega_Q^2 t}{32\omega_1}}e^{-\frac{i\omega_Q t}{4}} + C_+^{23}D_-^{32}e^{-\frac{i\omega_Q^2 t}{32\omega_1}}e^{-\frac{i\omega_Q t}{4}} + C_-^{32}D_+^{23}e^{\frac{i\omega_Q^2 t}{32\omega_1}}e^{\frac{i\omega_Q t}{4}} \end{aligned} \tag{F.17}$$

A detailed description of the coefficients is summarised in Table F.2. In Figure F.1 (second row), a comparison of the analytic simulations (based on FME, Eq. F.17) with numerical simulations is illustrated. As depicted, the FME based simulations are in complete disagreement to those obtained from SPINEVOLUTION. This is bit intriguing considering the fact that the analytic simulations based on the effective Floquet Hamiltonians (first row) are in excellent agreement with numerical simulations. Hence, the suitability of any analytic method could only be established through comparisons with exact numerical simulations.

2. MAS simulations

Based on the discussion in the chapter, the Hamiltonian for spin I=1 under MAS conditions is represented by the following equation.

$$H(t) = \frac{2\omega_{Q,2}^{(2)0}}{3}\cos\left(2\omega_r t\right)\left[I_Z^{12} - I_Z^{23}\right] + \sqrt{2}\omega_1\left[I_X^{12} + I_X^{23}\right] \tag{F.18}$$

operators	Initial Density Operator, C_α^{ij}	Detection Operator, $D_\alpha^{ij}(t)$	Density Operator, $R_\alpha^{ij}(t)$
I_+^{12}	$-\frac{1}{\sqrt{2}}\left[\cos(x)\, e^{i\omega_1 t} + \sin(x)\, e^{-i\omega_1 t}\right]$	$\frac{5}{2\sqrt{2}} e^{i\omega_1 t}\left(1 - \frac{a^2(t)+b^2(t)}{8}\right) - \frac{3}{4\sqrt{2}} e^{-i\omega_1 t}\left(a(t) + ib(t)\right)$	$-\frac{1}{\sqrt{2}}\left[\cos(x)\, e^{i\omega_1 t} + \sin(x)\, e^{-i\omega_1 t}\right] e^{-i\omega_e^{(1)} t} e^{i\omega_e^{(2)} t}$
I_-^{21}	$-\frac{1}{\sqrt{2}}\left[\cos(x)\, e^{-i\omega_1 t} + \sin(x)\, e^{i\omega_1 t}\right]$	$\frac{3}{2\sqrt{2}} e^{-i\omega_1 t}\left(1 - \frac{a^2(t)+b^2(t)}{8}\right) - \frac{5}{4\sqrt{2}} e^{i\omega_1 t}\left(a(t) - ib(t)\right)$	$-\frac{1}{\sqrt{2}}\left[\cos(x)\, e^{-i\omega_1 t} + \sin(x)\, e^{i\omega_1 t}\right] e^{i\omega_e^{(1)} t} e^{-i\omega_e^{(2)} t}$
I_+^{23}	$-\frac{1}{\sqrt{2}}\left[\cos(x)\, e^{i\omega_1 t} - \sin(x)\, e^{-i\omega_1 t}\right]$	$-\frac{5}{2\sqrt{2}} e^{i\omega_1 t}\left(1 - \frac{a^2(t)+b^2(t)}{8}\right) - \frac{3}{4\sqrt{2}} e^{-i\omega_1 t}\left(a(t) + ib(t)\right)$	$-\frac{1}{\sqrt{2}}\left[\cos(x)\, e^{i\omega_1 t} - \sin(x)\, e^{-i\omega_1 t}\right] e^{-i\omega_e^{(1)} t} e^{-i\omega_e^{(2)} t}$
I_-^{32}	$-\frac{1}{\sqrt{2}}\left[\cos(x)\, e^{-i\omega_1 t} - \sin(x)\, e^{i\omega_1 t}\right]$	$-\frac{3}{2\sqrt{2}} e^{-i\omega_1 t}\left(1 - \frac{a^2(t)+b^2(t)}{8}\right) - \frac{5}{4\sqrt{2}} e^{i\omega_1 t}\left(a(t) - ib(t)\right)$	$-\frac{1}{\sqrt{2}}\left[\cos(x)\, e^{-i\omega_1 t} - \sin(x)\, e^{i\omega_1 t}\right] e^{i\omega_e^{(1)} t} e^{i\omega_e^{(2)} t}$
	$x = \frac{\omega_Q}{8\omega_1}$	$\omega_e^{(1)} = \frac{\omega_Q^2}{32\omega_1}$	$\omega_e^{(2)} = \frac{\omega_Q}{4}$

Table F.2: Definition of constants employed in the description of the density operator and detection operator for FME - alternate boundary condition (static case)

The Hamiltonian in the rotating frame is transformed using the transformations given below.

$$\begin{aligned}\widetilde{\widetilde{H}}(t) &= U_2U_1H(t)U_1^{-1}U_2^{-1} \;\; ; \; U_1 = e^{i\frac{\pi\sqrt{2}}{2}\left[I_Y^{12}+I_Y^{23}\right]} \, , \; U_2 = e^{2i\omega_1 t I_Z^{13}} \\ &= -\frac{\omega_{Q,2}^{(2)0}}{3}\cos\left(2\omega_r t\right)\left[I_Z^{12}-I_Z^{23}\right] + \frac{\omega_{Q,2}^{(2)0}}{2}\cos\left(2\omega_r t\right)\left[I_+^{13}e^{2i\omega_1 t}+I_-^{31}e^{-2i\omega_1 t}\right] \end{aligned} \tag{F.19}$$

Subsequently, the Hamiltonian is further transformed by $U_3 = e^{i\Phi(t)[I_Z^{12}-I_Z^{23}]}$.

$$\begin{aligned}\widetilde{\widetilde{\widetilde{H}}}(t) &= U_3\widetilde{\widetilde{H}}(t)U_3^{-1} \\ &= \frac{\omega_{Q,2}^{(2)0}}{4}\left[I_+^{13}e^{2i(\omega_1+\omega_r)t}+I_+^{13}e^{2i(\omega_1-\omega_r)t}+I_-^{31}e^{-2i(\omega_1-\omega_r)t}+I_-^{31}e^{-2i(\omega_1+\omega_r)t}\right] \end{aligned} \tag{F.20}$$

Under rotary resonance condition i.e. $\omega_1 = \omega_r$, the above Hamiltonian has contributions from both time-independent and time-dependent terms.

$$\widetilde{\widetilde{\widetilde{H}}}(t) = \frac{\omega_{Q,2}^{(2)0}}{2}I_X^{13} + \frac{\omega_{Q,2}^{(2)0}}{4}\left[I_+^{13}e^{4i\omega_1 t}+I_-^{31}e^{-4i\omega_1 t}\right] \tag{F.21}$$

Following the procedure outlined in the chapter, the corrections to $\bar{H}$ and $\Lambda(t)$ (in alternate boundary condition ($\Lambda \neq 0$)) are evaluated.

$$\bar{H}^{(1)} = H_0 = \frac{\omega_{Q,2}^{(2)0}}{2}I_X^{13} \;\; ; \;\; \bar{H}^{(2)} = \sum_{k\neq 0}\left\{\frac{[H_k, H_{-k}]}{2k\omega}\right\} = \frac{2}{\omega_1}\left(\frac{\omega_{Q,2}^{(2)0}}{8}\right)^2 I_Z^{13} \tag{F.22}$$

$$\Lambda_1(t) = \frac{\omega_{Q,2}^{(2)0}}{8\omega_1}\cos\left(4\omega_1 t\right)I_Y^{13} + \frac{\omega_{Q,2}^{(2)0}}{8\omega_1}\sin\left(4\omega_1 t\right)I_X^{13} = a(t)I_Y^{13} + b(t)I_X^{13} \tag{F.23}$$

$$\Lambda_1(0) = \frac{\omega_{Q,2}^{(2)0}}{8\omega_1}I_Y^{13} = a(0)I_Y^{13} \tag{F.24}$$

When the RF amplitudes are higher than the quadrupolar frequency $\left(\frac{\sqrt{2}\omega_{Q,2}^{(2)0}}{3\omega_1} < 4\right)$, the second-order corrections ($\bar{H}^{(2)}$) are of lesser significance. To maintain consistency, both the initial density operator ($\rho(0) = 2I_Z^{13}$) and detection operator ($D = I_+^{13}$) are transformed by these unitary transformations.

$$\begin{aligned}\rho'(0) &= e^{i\Lambda(0)}U_2U_3U_1\rho(0)U_1^{-1}U_2^{-1}U_3^{-1}e^{-i\Lambda(0)} \\ &= -\frac{1}{\sqrt{2}}e^{3i\Phi(t)}\left\{e^{i\omega_1 t}\cos\left(\frac{a(0)}{2}\right)+e^{-i\omega_1 t}\sin\left(\frac{a(0)}{2}\right)\right\}I_+^{12} \\ &- \frac{1}{\sqrt{2}}e^{-3i\Phi(t)}\left\{e^{-i\omega_1 t}\cos\left(\frac{a(0)}{2}\right)+e^{i\omega_1 t}\sin\left(\frac{a(0)}{2}\right)\right\}I_-^{21} \\ &- \frac{1}{\sqrt{2}}e^{-3i\Phi(t)}\left\{e^{i\omega_1 t}\cos\left(\frac{a(0)}{2}\right)-e^{-i\omega_1 t}\sin\left(\frac{a(0)}{2}\right)\right\}I_+^{23} \\ &- \frac{1}{\sqrt{2}}e^{3i\Phi(t)}\left\{e^{-i\omega_1 t}\cos\left(\frac{a(0)}{2}\right)-e^{i\omega_1 t}\sin\left(\frac{a(0)}{2}\right)\right\}I_-^{32} \end{aligned} \tag{F.25}$$

$$
\begin{aligned}
D'(t) &= e^{i\Lambda(t)}U_2U_3U_1DU_1^{-1}U_2^{-1}U_3^{-1}e^{-i\Lambda(t)} \\
&= e^{3i\Phi(t)}\left\{\frac{5}{2\sqrt{2}}e^{i\omega_1 t}\left(1-\frac{a^2(t)+b^2(t)}{8}\right)-\frac{3}{4\sqrt{2}}e^{-i\omega_1 t}\left(a(t)+ib(t)\right)\right\}I_+^{12} \\
&+ e^{-3i\Phi(t)}\left\{\frac{3}{2\sqrt{2}}e^{-i\omega_1 t}\left(1-\frac{a^2(t)+b^2(t)}{8}\right)-\frac{5}{4\sqrt{2}}e^{i\omega_1 t}\left(a(t)-ib(t)\right)\right\}I_-^{21} \\
&+ e^{-3i\Phi(t)}\left\{-\frac{5}{2\sqrt{2}}e^{i\omega_1 t}\left(1-\frac{a^2(t)+b^2(t)}{8}\right)-\frac{3}{4\sqrt{2}}e^{-i\omega_1 t}\left(a(t)+ib(t)\right)\right\}I_+^{23} \\
&+ e^{3i\Phi(t)}\left\{-\frac{3}{2\sqrt{2}}e^{-i\omega_1 t}\left(1-\frac{a^2(t)+b^2(t)}{8}\right)-\frac{5}{4\sqrt{2}}e^{i\omega_1 t}\left(a(t)-ib(t)\right)\right\}I_-^{32}
\end{aligned}
\tag{F.26}
$$

Subsequently, the final signal expression is calculated using the standard relation.

$$
S(t) = Tr\left[e^{-iHt}\rho'(0)e^{iHt}.D'(t)\right] \quad ; \quad H = H_0 = \frac{\omega_{Q,2}^{(2)0}}{2}I_X^{13} \tag{F.27}
$$

To test the validity of the above analytic framework, comparison of the analytic simulations (based on Eq. F.27) with SPINEVOLUTION is illustrated in Figure F.2. As depicted in Figure F.2, the analytic simulations are in complete disagreement to the simulations from SPINEVOLUTION. The exact reasons behind the discrepancies is unknown and is certainly beyond the scope of the thesis.

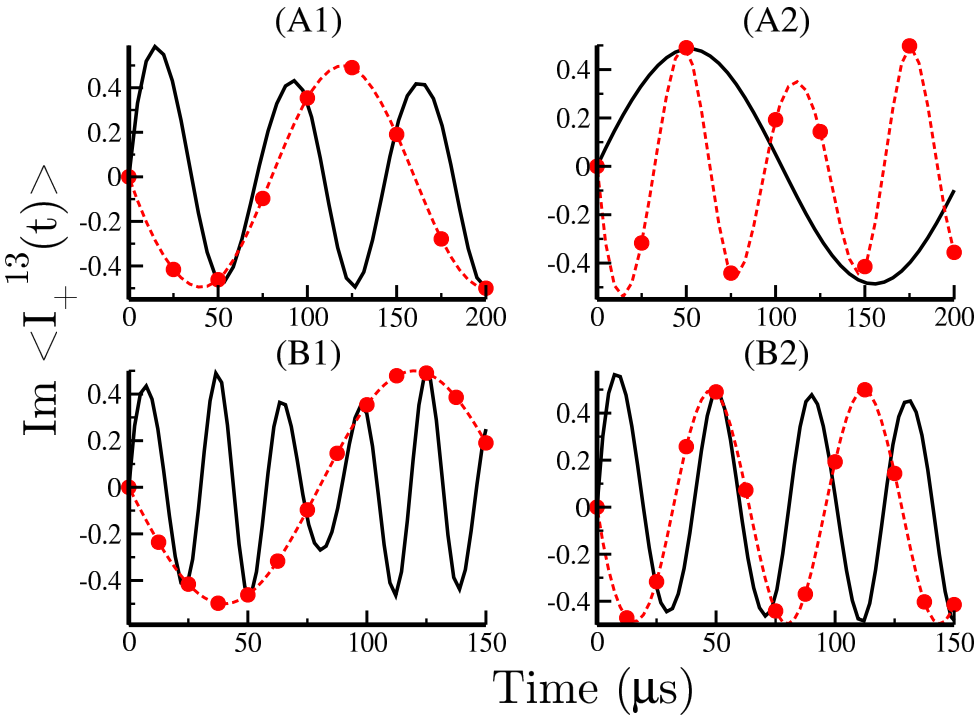

Figure F.2: In the simulations depicted (MAS case), the validity of the rf interaction frame calculations (Eq. F.27) is checked at rotary resonance condition for C_Q variation. The analytic simulations based on the calculations (dotted red line) are compared with those obtained from exact numerical methods based on SPINEVOLUTION [7] (solid black line). The parameters of simulations are- $\nu_1 = \nu_r = 20$ kHz for upper row (panels A1, A2) and $\nu_1 = \nu_r = 40$ kHz for bottom row (panels B1, B2) while C_Q ($\nu_{Q,2}^{(2)0}$) is varied along columns- (A1, B1) 100 kHz (25 kHz) (A2, B2) 250 kHz (62.5 kHz).

References

[1] A. Abragam, *The Principles of Nuclear Magnetism*, Oxford University Press, 1961.

[2] M. Mehring, *Principles of High Resolution NMR in Solids*, Springer-Verlag Berlin Heidelberg, 1983.

[3] C. P. Slichter, *Principles of Magnetic Resonance*, Springer, 1990.

[4] C. Banwell and H. Primas, *Molecular Physics*, 1963, **6**, 225–256.

[5] U. Haeberlen, *High Resolution NMR in Solids: Selective Averaging*, Academic Press, 1976.

[6] M. Bak, J. T. Rasmussen and N. C. Nielsen, *Journal of Magnetic Resonance*, 2000, **147**, 296–330.

[7] M. Veshtort and R. G. Griffin, *Journal of Magnetic Resonance*, 2006, **178**, 248–282.

[8] S. Vega, *The Journal of Chemical Physics*, 1978, **68**, 5518–5527.

[9] B. Sanctuary and T. Halstead, *Advances in Magnetic and Optical Resonance*, 1990, **15**, 79–161.

[10] A. Ramamoorthy, *NMR Spectroscopy of Biological Solids*, CRC Press, 2005.

[11] R. E. Wasylishen, S. E. Ashbrook and S. Wimperis, *NMR of Quadrupolar Nuclei in Solid Materials*, John Wiley & Sons, 2012.

[12] A. E. Bennett, R. G. Griffin and S. Vega, *Solid-State NMR IV Methods and Applications of Solid-State NMR*, Springer, 1994, pp. 1–77.

[13] M. Levitt, *Encyclopedia of Nuclear Magnetic Resonance. Harris, RK.; Wasylishen, RE., editors. Vol. 9*, Chichester: Wiley, 2002.

[14] R. R. Ernst, G. Bodenhausen, A. Wokaun *et al.*, *Principles of Nuclear Magnetic Resonance in One and Two Dimensions*, Clarendon Press Oxford, 1987, vol. 14.

[15] C. M. Rienstra, M. E. Hatcher, L. J. Mueller, B. Sun, S. W. Fesik and R. G. Griffin, *Journal of the American Chemical Society*, 1998, **120**, 10602–10612.

[16] C. M. Rienstra, M. Hohwy, M. Hong and R. G. Griffin, *Journal of the American Chemical Society*, 2000, **122**, 10979–10990.

[17] C. P. Jaroniec, B. A. Tounge, J. Herzfeld and R. G. Griffin, *Journal of the American Chemical Society*, 2001, **123**, 3507–3519.

[18] C. P. Jaroniec, C. Filip and R. G. Griffin, *Journal of the American Chemical Society*, 2002, **124**, 10728–10742.

[19] F. Castellani, B.-J. van Rossum, A. Diehl, K. Rehbein and H. Oschkinat, *Biochemistry*, 2003, **42**, 11476–11483.

[20] S. A. Smith, W. E. Palke and J. Gerig, *Concepts in Magnetic Resonance*, 1992, **4**, 107–144.

[21] S. A. Smith, W. E. Palke and J. Gerig, *Concepts in Magnetic Resonance*, 1992, **4**, 181–204.

[22] E. R. Andrew, A. Bradbury and R. G. Eades, *Nature*, 1958, **182**, 1659–1659.

[23] I. J. Lowe, *Physical Review Letters*, 1959, **2**, 285–287.

[24] P. P. Man, *Encyclopedia of Nuclear Magnetic Resonance*, 2007, **6**, 3838.

[25] S. Vega and Y. Naor, *The Journal of Chemical Physics*, 1981, **75**, 75–86.

[26] R. V. SubbaRao, D. Srivastava and R. Ramachandran, *Physical Chemistry Chemical Physics*, 2013, **15**, 2081–2104.

[27] D. Srivastava and R. Ramachandran, *RSC Advances*, 2013, **3**, 25231–25236.

[28] D. Srivastava, R. V. SubbaRao and R. Ramachandran, *Physical Chemistry Chemical Physics*, 2013, **15**, 6699–6713.

[29] V. Ganapathy and R. Ramachandran, *The Journal of Chemical Physics*, 2017, **147**, 144202.

[30] S. Vega and A. Pines, *The Journal of Chemical Physics*, 1977, **66**, 5624–5644.

[31] A. Wokaun and R. Ernst, *The Journal of Chemical Physics*, 1977, **67**, 1752–1758.

[32] A. Pines, S. Vega and M. Mehring, *Physical Review B*, 1978, **18**, 112.

[33] D. Suwelack, M. Mehring and A. Pines, *Physical Review B*, 1979, **19**, 238.

[34] A. J. Vega, *Journal of Magnetic Resonance (1969)*, 1992, **96**, 50–68.

[35] K. Gopalakrishnan and G. Bodenhausen, *The Journal of Chemical Physics*, 2006, **124**, 194311.

[36] G. Kervern, G. Pintacuda and L. Emsley, *Chemical Physics Letters*, 2007, **435**, 157–162.

[37] A. J. Pell, G. Kervern, L. Emsley, M. Deschamps, D. Massiot, P. J. Grandinetti and G. Pintacuda, *The Journal of Chemical Physics*, 2011, **134**, 024117.

[38] S. Wi, Z. Gan, R. Schurko and L. Frydman, *The Journal of Chemical Physics*, 2015, **142**, 064201.

[39] N. C. Nielsen, H. Bildsøe and H. J. Jakobsen, *Chemical Physics Letters*, 1992, **191**, 205–212.

[40] T. Charpentier, C. Fermon and J. Virlet, *Journal of Magnetic Resonance*, 1998, **132**, 181–190.

[41] M. R. Aliev and V. T. Aleksanyan, *Optica Spectroscopia*, 1968, **24**, 520.

[42] M. R. Aliev and V. T. Aleksanyan, *Optica Spectroscopia*, 1968, **24**, 695.

[43] J. Van Vleck, *Physical Review*, 1929, **33**, 467.

[44] U. Haeberlen and J. S. Waugh, *Physical Review*, 1968, **175**, 453.

[45] G. Floquet, *Annales scientifiques de l'École normale supérieure*, 1883, **12**, 47–89.

[46] J. H. Shirley, *Physical Review*, 1965, **138**, 979–987.

[47] T. Levante, M. Baldus, B. Meier and R. Ernst, *Molecular Physics*, 1995, **86**, 1195–1212.

[48] B. C. Filip, X. Filip, Demco and D. E. Siegfried Hafner, *Molecular Physics*, 1997, **92**, 757–772.

[49] R. Ramesh and M. S. Krishnan, *The Journal of Chemical Physics*, 2001, **114**, 5967.

[50] M. Leskes, P. Madhu and S. Vega, *Progress in Nuclear Magnetic Resonance Spectroscopy*, 2010, **57**, 345 – 380.

[51] I. Scholz, J. D. van Beek and M. Ernst, *Solid State Nuclear Magnetic Resonance*, 2010, **37**, 39 – 59.

[52] J. Campbell, *Proceedings of the London Mathematical Society*, 1896, **1**, 381–390.

[53] R. Garg and R. Ramachandran, *The Journal of Chemical Physics*, 2017, **146**, 184201.

[54] S. Ganguly, R. Garg and R. Ramachandran, *The Journal of Chemical Physics*, 2020, **153**, 094103.

[55] M. Bansal and R. Ramachandran, *Journal of Magnetic Resonance Open*, 2022, **10**, 100042.

[56] M. Bansal and R. Ramachandran, *Physical Chemistry Chemical Physics*, 2022, **24**, 29092.

[57] P. Caravatti, G. Bodenhausen and R. Ernst, *Journal of Magnetic Resonance (1969)*, 1983, **55**, 88–103.

[58] J. P. Carvalho and A. J. Pell, *Journal of Magnetic Resonance*, 2021, **324**, 106911.

[59] G. B. Arfken, H. J. Weber and F. E. Harris, *Mathematical Methods for Physicists, 7th ed*, Academic Press, 2013.

[60] J. Pratt, *Molecular Physics*, 1977, **34**, 539–555.

[61] R. Reddy and P. Narasimhan, *Molecular Physics*, 1991, **72**, 491–507.

[62] R. Reddy and P. Narasimhan, *Molecular Physics*, 1991, **72**, 509–521.

[63] B. Sanctuary, *The Journal of Chemical Physics*, 1976, **64**, 4352–4361.

[64] G. Bowden and W. Hutchison, *Journal of Magnetic Resonance (1969)*, 1986, **67**, 403–414.

[65] G. Bowden, W. Hutchison and J. Khachan, *Journal of Magnetic Resonance (1969)*, 1986, **67**, 415–437.

[66] W. Magnus, *Communications on Pure and Applied Mathematics*, 1954, **7**, 649–673.

[67] R. Garg and R. Ramachandran, *The Journal of Chemical Physics*, 2020, **153**, 034106.

[68] F. Casas, J. Oteo and J. Ros, *Journal of Physics A: Mathematical and General*, 2001, **34**, 3379.

[69] S. Blanes, F. Casas, J.-A. Oteo and J. Ros, *Physics Reports*, 2009, **470**, 151–238.

[70] E. S. Mananga and T. Charpentier, *The Journal of Chemical Physics*, 2011, **135**, 044109.

[71] J. Amoureux, M. Pruski, D. Lang and C. Fernandez, *Journal of Magnetic Resonance*, 1998, **131**, 170–175.

Chapter 3

Description of recoupling effects in MAS experiments involving spin-1/2 system coupled to spin S=1

3.1 Introduction

The availability of sophisticated NMR hardware has immensely enhanced the ability of solid-state NMR (ssNMR) spectroscopy in addressing wide-range of problems of chemical and biology relevance involving quadrupolar spins [1–9]. In particular, the availability of ultra-fast MAS probes has ushered in the development of cost effective methods in the form of proton-based ssNMR experiments for studying biological systems [10–12]. Consequently, studies involving spin I=1/2 nuclei coupled to quadrupolar spins are now routinely possible in the solid-state. While the implementation of these experiments have became easier with the availability of higher magnetic field strengths and ultrafast MAS probes, optimal design of experiments that involve spin I=1/2 nuclei coupled with quadrupolar spin has remained a challenging task. In particular, implementation of experiments on spin-1/2 nuclei have always been impeded by the interference effects arising from RF fields employed on the quadrupolar spin. Since extraction of molecular constraints in NMR experiments involves iterative fitting of the experimental data, analytic models/expressions that are computationally efficient are essential.

Here, in this chapter, we focus on the interference effects that arise in experiments involving spin I=1/2 nuclei coupled to S=1. Specifically, we focus on the interference effects introduced by the RF field on the quadrupolar spin in experiments that involve (i) mea-

surement of CSA tensors on spin¯I=1/2 (ii) polarisation transfer from spin I=1/2 to S=1. A schematic depiction of the pulse sequence employed to study the interference effects is illustrated in Figure 3.1.

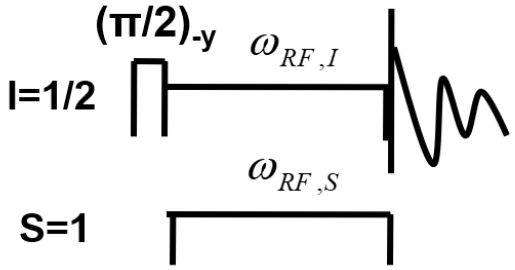

Figure 3.1: Schematic representation of the pulse sequence

3.2 Measurement of CSA interactions in spin I=1/2 nucleus coupled to S=1

In its simplest implementation, the CSA interaction on spin I=1/2 is reintroduced under MAS conditions by employing a constant RF field on the I-channel. When the amplitude of the RF field on the I-channel is adjusted to an integer multiple of the spinning frequency ($\omega_{RF,I} = n\omega_r$, n=1 or 2), a part of the CSA interactions is reintroduced under MAS. However, estimation of chemical shift tensors in such experiments have always remained challenging [13–17], owing to the simultaneous reintroduction of heteronuclear dipolar interactions. Consequently, to minimize the undesirable effects of the heteronuclear dipolar interactions on the line-shape (of spin I=1/2 nucleus), a strong (CW) decoupling field is additionally employed on the quadrupolar spin [18–21]. Although, numerical methods [22,23] have facilitated in the optimisation (through trial and error) of such experiments, a formal understanding entails an analytic approach. To illustrate this point, we begin with numerical simulations illustrated in Figure 3.2.

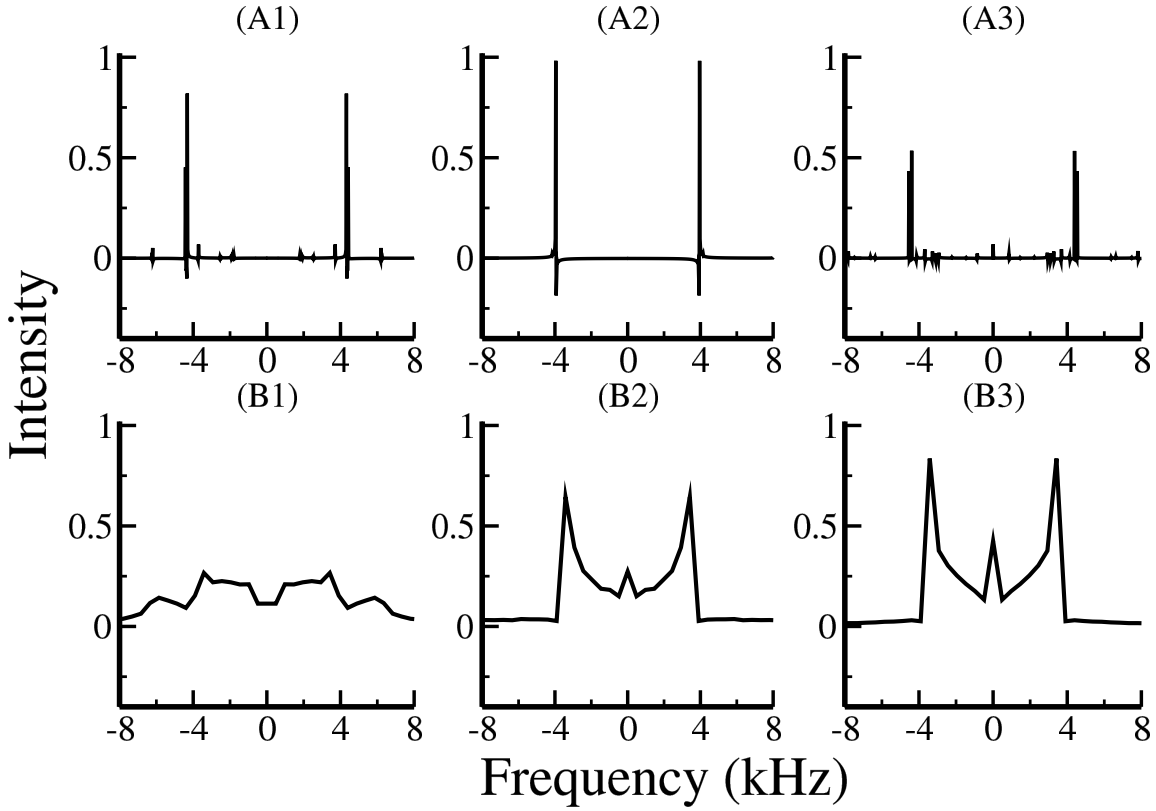

Figure 3.2: In the simulations illustrated, the FT spectrum of spin I=1/2 nucleus coupled to a quadrupolar spin (S=1) is illustrated for different RF field strength employed on the quadrupolar spin. A constant RF field strength of 40 kHz on I=1/2 ($\nu_{RF,I}$ = 40 kHz) and spinning frequency of 40 kHz (ν_r = 40 kHz) was employed in the simulations. The following parameters were employed in the simulations. CSA parameters on spin I=1/2 (δ = 10.0 kHz, η= 1.0, Ω_{PM} = (10°, 30°, 40°)). Quadrupolar parameters (C_Q = 1 MHz, η= 1.0, Ω_{PM} = (30°, 40°, 60°)) and dipolar parameters (ω_{IS} = 8.6 kHz). The amplitude of the RF field strength (decoupling field on quadrupolar spin) is varied along the column, $\nu_{RF,S}$ = 10 kHz (panels A1 and B1), 40 kHz (panels A2 and B2), 100 kHz (panels A3 and B3). The simulations along the first row corresponds to a single crystal, while, the powder simulations are depicted along the second row.

In the simulations depicted, the interference effect due to RF field (on the quadrupolar spin) on the line-shape of spin I=1/2 nucleus (based on pulse scheme depicted in Figure 3.1) in both single crystal (first row) and powder sample (second row) is illustrated. Employing a constant RF field on spin 'I' (I=1/2), the CSA interaction of the spin 'I' nucleus is reintroduced along with the heteronuclear dipolar interactions (I=1/2, S=1) under MAS conditions. To minimize the undesirable effects of the heteronuclear dipolar interactions on the

line-shape of spin 'I=1/2' nucleus, a strong (CW) decoupling field is additionally employed on the quadrupolar spin. As depicted in Figure 3.2, the resolution of the spectrum in the powder sample (second row) improves with increase in the decoupling field strength, while such a trend is unobserved in the case of a single crystal (first row). In particular, the exact reasons behind the loss in resolution depicted in panel A3 (Figure 3.2) remains intriguing and less obvious from numerical simulations. Henceforth, to explicate the observations mentioned above, a formal description of the underlying spin dynamics outlining the interplay between spinning frequency, RF field strength and quadrupolar coupling constant remains essential. Although, several theoretical formulations have emerged [13,14,24–27] for describing the effects of the quadrupolar spin on the NMR spectrum of spin-1/2 nuclei, a formal description of the interference effects in terms of analytic expressions in MAS experiments has always remained elusive.

To this end, we employ an isolated spin pair (I=1/2, S=1) as a model system to describe the interference effects in I=1/2 system coupled to a quadrupolar spin, S=1. The notations employed to describe the spin states, operators and possible transitions of spin I=1/2 ($|1\rangle \rightarrow |4\rangle$, $|2\rangle \rightarrow |5\rangle$ and $|3\rangle \rightarrow |6\rangle$) are summarized through the energy level diagram depicted in Figure 3.3.

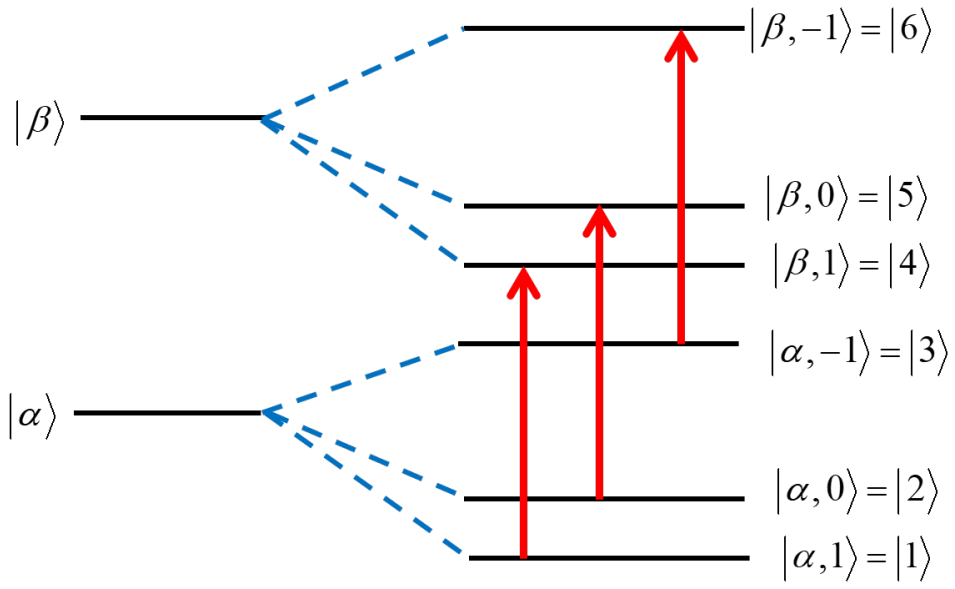

Figure 3.3: Energy level diagram for a spin I=1/2 system coupled to a quadrupolar spin, S=1 (red arrows correspond to transitions of spin I=1/2 system)

Accordingly, the Hamiltonian of an isolated spin pair (spin I=1/2 coupled to spin S=1)

in the rotating frame is represented by the following equation.

$$H(t) = H_{I,CSA}(t) + H_{I,RF}(t) + H_{S,Q}(t) + H_{S,RF}(t) + H_{IS}(t) \tag{3.1}$$

The CSA interactions corresponding to spin 'I' are represented by, $H_{I,CSA}(t)$.

$$H_{I,CSA}(t) = \sum_{m=-2,\neq 0}^{2} \omega_I^{(m)} e^{im\omega_r t} I_Z = \sum_{m=-2,\neq 0}^{2} \omega_I^{(m)} e^{im\omega_r t} \left[I_Z^{14} + I_Z^{25} + I_Z^{36}\right] \tag{3.2}$$

The quadrupolar interactions on spin 'S' is represented by, $H_{S,Q}(t)$.

$$H_{S,Q}(t) = \sum_{m=-2,\neq 0}^{2} \frac{\omega_Q^{(m)}}{6} e^{im\omega_r t} \left[3S_Z^2 - S^2\right] = \sum_{m=-2,\neq 0}^{2} \frac{\omega_Q^{(m)}}{3} e^{im\omega_r t} \left[I_Z^{12} - I_Z^{23} + I_Z^{45} - I_Z^{56}\right] \tag{3.3}$$

The interaction between spins (I and S) is mediated through the heteronuclear dipolar interaction, $H_{IS}(t)$.

$$H_{IS}(t) = \sum_{m=-2,\neq 0}^{2} 2\omega_{IS}^{(m)} e^{im\omega_r t} I_Z S_Z = \sum_{m=-2,\neq 0}^{2} 2\omega_{IS}^{(m)} e^{im\omega_r t} \left[I_Z^{13} - I_Z^{46}\right] \tag{3.4}$$

In MAS experiments, the anisotropic components of the internal interactions (CSA, dipolar and quadrupolar interaction) are represented through the following standard expression.

$$\omega_\lambda^{(m)} = \sum_{m_1=-2}^{2} R_{P,\lambda}^{(2)m_1} \sum_{m_2=-2}^{2} D_{m_1 m_2}\left(\Omega_{PM}\right) D_{m_2 m}\left(\Omega_{MR}\right) d_{m0}\left(\beta_{RL}\right) \tag{3.5}$$

Here, $R_{P,\lambda}^{(2)m_1}$ represents the component of the spatial tensor (λ= CSA, dipolar or quadrupolar interaction) defined in the principal axis system (PAS), while, $D_{m_1 m_2}\left(\Omega_{AB}\right)$ denotes the Wigner Rotation matrix. The detailed description of these coefficients is provided in Chapter-1.

The Hamiltonian depicting the continuous wave field (CW) applied on both the channels is represented by-

$$H_{I,RF}(t) = \omega_{RF,I} I_X = \omega_{RF,I} \left[I_X^{14} + I_X^{25} + I_X^{36}\right] \tag{3.6}$$

$$H_{S,RF}(t) = \omega_{RF,S} S_X = \sqrt{2}\omega_{RF,S} \left[I_X^{12} + I_X^{23} + I_X^{45} + I_X^{56}\right] \tag{3.7}$$

Due to larger magnitude of the quadrupolar interactions, the Hamiltonian (Eq. 3.1) is transformed into the quadrupolar interaction frame [28–34] (defined by $U_1 = e^{i\Phi(t)[I_Z^{12} - I_Z^{23} + I_Z^{45} - I_Z^{56}]}$). In the quadrupolar interaction frame, both the CSA interactions of spin 'I' ($H_{I,CSA}(t)$) and the dipolar interactions ($H_{IS}(t)$) are invariant, while, the RF Hamiltonian (that was constant in the rotating frame) on spin 'S' becomes time-dependent.

$$\widetilde{H}(t) = U_1 H(t) U_1^{-1} = H_{I,CSA}(t) + H_{I,RF}(t) + \widetilde{H}_{S,RF}(t) + H_{IS}(t) \tag{3.8}$$

$$\widetilde{H}_{S,RF}(t) = U_1 H_{S,RF}(t) U_1^{-1} = \sqrt{2}\omega_{RF,S} A \left[I_X^{12} + I_X^{23} + I_X^{45} + I_X^{56}\right] + \sqrt{2}\omega_{RF,S} \sum_n A_{X,n} e^{in\omega_r t} \left[I_X^{12} + I_X^{23} + I_X^{45} + I_X^{56}\right] + \sqrt{2}\omega_{RF,S} \sum_n B_{Y,n} e^{in\omega_r t} \left[I_Y^{12} - I_Y^{23} + I_Y^{45} - I_Y^{56}\right] \quad (3.9)$$

where

$$A = \sum_{n_1} J_{n_1}(A_1) \sum_{n_2} J_{n_2}(A_2) \sum_{n_3} J_{n_3}(A_3) \sum_{n_4} J_{n_4}(A_4) \;\; ; \;\; n_1 + n_2 + n_3 + n_4 = 0$$

The coefficients ($A_{X,p}$ and $B_{Y,p}$) in the time-dependent RF part are expressed in terms of Bessel functions [35] as given below.

$$A_{X,p} \propto \sum_{n_1} J_{n_1}(A_1) \sum_{n_2} J_{n_2}(A_2) \sum_{n_3} J_{n_3}(A_3) \sum_{n_4} J_{n_4}(A_4) \; ; \; n_1 + n_2 + n_3 + n_4 = p \quad (3.10)$$

$$B_{Y,p} \propto \sum_{n_1} J_{n_1}(A_1) \sum_{n_2} J_{n_2}(A_2) \sum_{n_3} J_{n_3}(A_3) \sum_{n_4} J_{n_4}(A_4) \; ; \; n_1 + n_2 + n_3 + n_4 = p \quad (3.11)$$

where

$$A_1 = \frac{\omega_Q^{(1)} - \omega_Q^{(-1)}}{2i\omega_r} \;,\; A_2 = \frac{\omega_Q^{(1)} + \omega_Q^{(-1)}}{2\omega_r} \;,\; A_3 = \frac{\omega_Q^{(2)} - \omega_Q^{(-2)}}{4i\omega_r} \;,\; A_4 = \frac{\omega_Q^{(2)} + \omega_Q^{(-2)}}{4\omega_r}$$

Case-I: Single Crystal with $\Omega_{PM} = (0, 90, 0)$

To describe the spin dynamics, we begin with the special case of a single crystal, wherein all the internal interactions (i.e. CSA on I-spin, Quadrupolar interaction on S-spin and dipolar coupling between I and S spin) have the special orientation, $\Omega_{PM} = (0, 90, 0)$ and η=1.0. Under this condition, only one of the components of the internal interaction is present ($\omega_\lambda^{(\pm 1)=0}$ where λ= CSA, dipolar or quadrupolar interaction). Consequently, the Hamiltonian in the quadrupolar interaction frame (Eq. 3.8) reduces to a simpler form given below.

$$\widetilde{H}(t) = U_1 H(t) U_1^{-1} = 2\omega_I^{(2)} \cos(2\omega_r t) \left[I_Z^{14} + I_Z^{25} + I_Z^{36}\right] + \omega_{RF,I} \left[I_X^{14} + I_X^{25} + I_X^{36}\right] + 4\omega_{IS}^{(2)} \cos(2\omega_r t) \left[I_Z^{13} - I_Z^{46}\right] + \sqrt{2}\omega_{RF,S} J_0(A) \left[I_X^{12} + I_X^{23} + I_X^{45} + I_X^{56}\right] + \sqrt{2}\omega_{RF,S} \sum_{k=\pm 4, \pm 8, ..} J_{k/2}(A) e^{ik\omega_r t} \left[I_X^{12} + I_X^{23} + I_X^{45} + I_X^{56}\right] + i\sqrt{2}\omega_{RF,S} \sum_{m=\pm 2, \pm 6, ..} J_{m/2}(A) e^{im\omega_r t} \left[I_Y^{12} - I_Y^{23} + I_Y^{45} - I_Y^{56}\right] \quad (3.12)$$

where $A = \dfrac{\omega_Q^{(2)}}{2\omega_r}$ represents the argument of the Bessel function [35].
It is important to note that the above choice of parameters have been employed solely for demonstrative purposes and the framework presented in this chapter is equally valid for any arbitrary orientation of the spin interactions.

Employing the Magnus formula [36], corrections to second order are derived for describing the Hamiltonian on the S-channel.

$$\begin{aligned}\bar{H} = \bar{H}^{(1)} + \bar{H}^{(2)} &= \sqrt{2}\omega_{RF,S} J_0(A)\left[I_X^{12} + I_X^{23} + I_X^{45} + I_X^{56}\right] \\ &- \frac{2\omega_{RF,S}^2}{\omega_r} J_0(A)\left\{\sum_{n=2p-1} \frac{J_n(A)}{n}\right\}\left[I_Z^{12} - I_Z^{23} + I_Z^{45} - I_Z^{56} + I_X^{13} + I_X^{46}\right] \end{aligned} \tag{3.13}$$

To facilitate analytic description, the Hamiltonian, $\bar{H}$ is transformed (using unitary transformation, $U_2 = e^{\dfrac{i\theta[I_Y^{12} - I_Y^{23}]}{\sqrt{2}}}$, $\tan\theta = \dfrac{\dfrac{2\omega_{RF,S}^2 J_0(A)}{\omega_r}\left[\sum\limits_{n=2p-1}\dfrac{J_n(A)}{n}\right]}{\omega_{RF,S} J_0(A)}$)) such that the Hamiltonian reduces to a form comprising commuting set of operators.

$$\begin{aligned} H_{eff} &= U_2 \bar{H} U_2^{-1} \\ &= \left\{\frac{\omega_{RF,S} J_0(A)}{\sqrt{2}}\cos\theta + \frac{\sqrt{2}\omega_{RF,S}^2}{\omega_r} J_0(A)\left\{\sum_{n=2p-1}\frac{J_n(A)}{n}\right\}\sin\theta\right\}\left[I_X^{12} + I_X^{23} + I_X^{45} + I_X^{56}\right] \\ &= \sqrt{2}\omega_{RF,eff}\left[I_X^{12} + I_X^{23} + I_X^{45} + I_X^{56}\right] \end{aligned} \tag{3.14}$$

Employing the above form of the effective RF Hamiltonian on S-channel (Eq. 3.14), the total Hamiltonian of the system (Eq. 3.12) reduces to a simpler form given below.

$$\begin{aligned}\widetilde{H}(t) = 2\omega_I^{(2)}\cos(2\omega_r t)\left[I_Z^{14} + I_Z^{25} + I_Z^{36}\right] + \omega_{RF,I}\left[I_X^{14} + I_X^{25} + I_X^{36}\right] \\ + 4\omega_{IS}^{(2)}\cos(2\omega_r t)\left[I_Z^{13} - I_Z^{46}\right] + \sqrt{2}\omega_{RF,eff}\left[I_X^{12} + I_X^{23} + I_X^{45} + I_X^{56}\right] \end{aligned} \tag{3.15}$$

To describe the interference effects, the above Hamiltonian is further transformed using a series of transformations, $U_3 = e^{i\dfrac{\pi}{2}[I_Y^{14} + I_Y^{25} + I_Y^{36}]}$ and $U_4 = e^{2i\omega_r t[I_Z^{14} + I_Z^{25} + I_Z^{36}]}$.

$$\begin{aligned}\widetilde{\bar{H}}(t) = U_4 U_3 \widetilde{H}(t) U_3^{-1} U_4^{-1} &= (\omega_{RF,I} - 2\omega_r)\left[I_Z^{14} + I_Z^{25} + I_Z^{36}\right] + \sqrt{2}\omega_{RF,eff}\left[I_X^{12} + I_X^{23} + I_X^{45} + I_X^{56}\right] \\ &- 2\omega_I^{(2)}\cos(2\omega_r t)\left\{\left[I_X^{14} + I_X^{25} + I_X^{36}\right]\cos(2\omega_r t) - \left[I_Y^{14} + I_Y^{25} + I_Y^{36}\right]\sin(2\omega_r t)\right\} \\ &- 4\omega_{IS}^{(2)}\cos(2\omega_r t)\left\{\left[I_X^{14} - I_X^{36}\right]\cos(2\omega_r t) - \left[I_Y^{14} - I_Y^{36}\right]\sin(2\omega_r t)\right\} \end{aligned} \tag{3.16}$$

To zeroth order, the Hamiltonian (Eq. 3.16) in the interaction frame is approximately described by the time-independent terms (ignoring the time-dependent terms) comprising the reintroduced internal interactions such as CSA and dipolar interactions. For operational

reasons, the effective (recoupled) Hamiltonian is expressed as a sum of two terms as given below.

$$H_{recoupled} = H_A + H_B \tag{3.17}$$

$$H_A = (\omega_{RF,I} - 2\omega_r)\left[I_Z^{14} + I_Z^{25} + I_Z^{36}\right] - k\omega_I^{(2)}\left[I_X^{14} + I_X^{25} + I_X^{36}\right] \tag{3.18}$$

$$H_B = -2k\omega_{IS}^{(2)}\left[I_X^{14} - I_X^{36}\right] + \sqrt{2}\omega_{RF,eff}\left[I_X^{12} + I_X^{23} + I_X^{45} + I_X^{56}\right] \tag{3.19}$$

The constant 'k' denotes the scaling factor that results from the multiple-pulse scheme [18,21,37] employed on spin 'I' to reintroduce the CSA interaction (in the present context, k=1). When the RF amplitude on I-channel is adjusted to the matching condition ($\omega_{RF,I} = 2\omega_r$), the longitudinal component (I_Z^{ij} operator in H_A) becomes zero and the Hamiltonian comprises only the CSA interactions (of spin 'I'). Since evolution under 'H_A' is of relevance in the present study, the recoupled Hamiltonian (Eq. 3.19) is transformed using the transformation function, $U_5 = e^{-i\sqrt{2}\theta_1\left[I_Y^{15} - I_Y^{24} + I_Y^{26} - I_Y^{35}\right]}$, such that the final form of the effective Hamiltonian resembles to the one described by H_A.

$$H_{eff} = U_5 H_{recoupled} U_5^{-1} = -\left(k\omega_I^{(2)} + 2\omega_{eff}\right) I_X^{14} - k\omega_I^{(2)} I_X^{25} - \left(k\omega_I^{(2)} - 2\omega_{eff}\right) I_X^{36} \tag{3.20}$$

$$\tan\theta_1 = \frac{\omega_{RF,eff}}{k\omega_{IS}^{(2)}}\ ,\ \omega_{eff} = k\omega_{IS}^{(2)}\cos\theta_1 + \omega_{RF,eff}\sin\theta_1 \tag{3.21}$$

As illustrated in Eq. (3.20), the operators corresponding to the allowed transitions ($|1\rangle \rightarrow |4\rangle$ and $|3\rangle \rightarrow |6\rangle$) are influenced by the heteronuclear dipolar interactions, while, the transition corresponding to the states, $|2\rangle \rightarrow |5\rangle$ remains unaffected. To maintain consistency, both the operators (initial density operator ($\rho(0) = I_X = I_X^{14} + I_X^{25} + I_X^{36}$) and detection operator ($D = I_+ = I_+^{14} + I_+^{25} + I_+^{36}$)) are transformed by the same set of transformations.

$$\begin{aligned}
\rho'(0) &= U_5U_4U_3U_2U_1\rho(0)U_1^{-1}U_2^{-1}U_3^{-1}U_4^{-1}U_5^{-1} \\
&= \left(\frac{1+\cos(2\theta_1)}{2}\right)\left[I_Z^{14} + I_Z^{36}\right] + \cos(2\theta_1)\left[I_Z^{25}\right] \\
&+ \left(\frac{1-\cos(2\theta_1)}{2}\right)\left[I_X^{13} - I_X^{46}\right] + \frac{1}{\sqrt{2}}\sin(2\theta_1)\left[I_X^{15} - I_X^{24} + I_X^{26} - I_X^{35}\right]
\end{aligned} \tag{3.22}$$

$$
\begin{aligned}
D' &= U_5U_4U_3U_2U_1DU_1^{-1}U_2^{-1}U_3^{-1}U_4^{-1}U_5^{-1} \\
&= \left(\frac{1+\cos(2\theta_1)}{2}\right)\left[I_Z^{14}+I_Z^{36}\right]+\cos(2\theta_1)\left[I_Z^{25}\right] \\
&+ \left(\frac{1-\cos(2\theta_1)}{2}\right)\left[I_X^{13}-I_X^{46}\right]+\frac{1}{\sqrt{2}}\sin(2\theta_1)\left[I_X^{15}-I_X^{24}+I_X^{26}-I_X^{35}\right]
\end{aligned} \tag{3.23}
$$

Subsequently, employing the density operator at time 't', the final form of the normalized signal ($Tr\left[\rho(0)^2=\frac{3}{2}\right]$) is derived and summarised below.

$$
\begin{aligned}
\rho'(t) &= e^{-iH_{eff}t}\rho'(0)e^{iH_{eff}t} \\
&= \left(\frac{1+\cos(2\theta_1)}{2}\right)\cos(2\omega_{eff}t)\cos\left(k\omega_I^{(2)}t\right)\left[I_Z^{14}+I_Z^{36}\right]+\cos(2\theta_1)\cos\left(k\omega_I^{(2)}t\right)\left[I_Z^{25}\right] \\
&+ \frac{1}{\sqrt{2}}\sin(2\theta_1)\cos(\omega_{eff}t)\cos\left(k\omega_I^{(2)}t\right)\left[I_X^{15}-I_X^{24}+I_X^{26}-I_X^{35}\right] \\
&+ \left(\frac{1-\cos(2\theta_1)}{2}\right)\cos\left(k\omega_I^{(2)}t\right)\left[I_X^{13}-I_X^{46}\right]
\end{aligned} \tag{3.24}
$$

$$
\begin{aligned}
S(t) &= \frac{Tr\left[\rho'(t)D'\right]}{Tr\left[\rho(0)^2\right]} \\
&= I_1\cos\left(k\omega_I^{(2)}t\right)+I_2\cos(\omega_{eff}t)\cos\left(k\omega_I^{(2)}t\right)+I_3\cos(2\omega_{eff}t)\cos\left(k\omega_I^{(2)}t\right)
\end{aligned} \tag{3.25}
$$

where

$$
I_1=\frac{1}{3}\cos^2(2\theta_1)+\frac{2}{3}\left(\frac{1-\cos(2\theta_1)}{2}\right)^2, I_2=\frac{2}{3}\sin^2(2\theta_1), I_3=\frac{2}{3}\left(\frac{1+\cos(2\theta_1)}{2}\right)^2
$$

As described above, the time-domain signal (Eq. 3.25) in the present context comprises frequency terms symmetrically distributed around the magnitude of the CSA interactions on spin 'I' ($\omega_I^{(2)}, \omega_I^{(2)}\pm\omega_{eff}, \omega_I^{(2)}\pm 2\omega_{eff}$). Based on the present analytic framework, the final signal expression (Eq. 3.25) could in principle be quantified in terms of the contributions from the transitions present in the coupled system. Accordingly, the frequency term, $\cos\left(k\omega_I^{(2)}t\right)$ in Eq. (3.25) is associated with the contributions from the allowed $|2\rangle\rightarrow|5\rangle$ and forbidden transitions ($|1\rangle\rightarrow|3\rangle$, $|4\rangle\rightarrow|6\rangle$) in the coupled system. The frequency term proportional to $\omega_I^{(2)}\pm\omega_{eff}$ (second term in Eq. 3.25)) result from transitions that involve flipping of both spins (i.e. $|1\rangle\rightarrow|5\rangle$, $|2\rangle\rightarrow|6\rangle$, $|3\rangle\rightarrow|5\rangle$ and $|2\rangle\rightarrow|4\rangle$). In a similar vein, the frequency term proportional to $\omega_I^{(2)}\pm 2\omega_{eff}$ (third term in Eq. 3.25) results from the two allowed transitions associated with spin 'I' (i.e. $|1\rangle\rightarrow|4\rangle$, $|3\rangle\rightarrow|6\rangle$).

To verify the exactness of the above analytic framework, the time-domain signal obtained from Eq. (3.25) is compared with those obtained from exact numerical methods [22]. In the simulations illustrated in Figure 3.4, the time-domain signal (based on Eq. 3.25) is evaluated at different decoupling field strengths (panels A1-A4). As illustrated, the analytic simulations are in excellent agreement in all the panels validating the analytic framework. To further substantiate the proposed analytical framework, we extend the above calculations to a single crystal with arbitrary orientation in the following subsection.

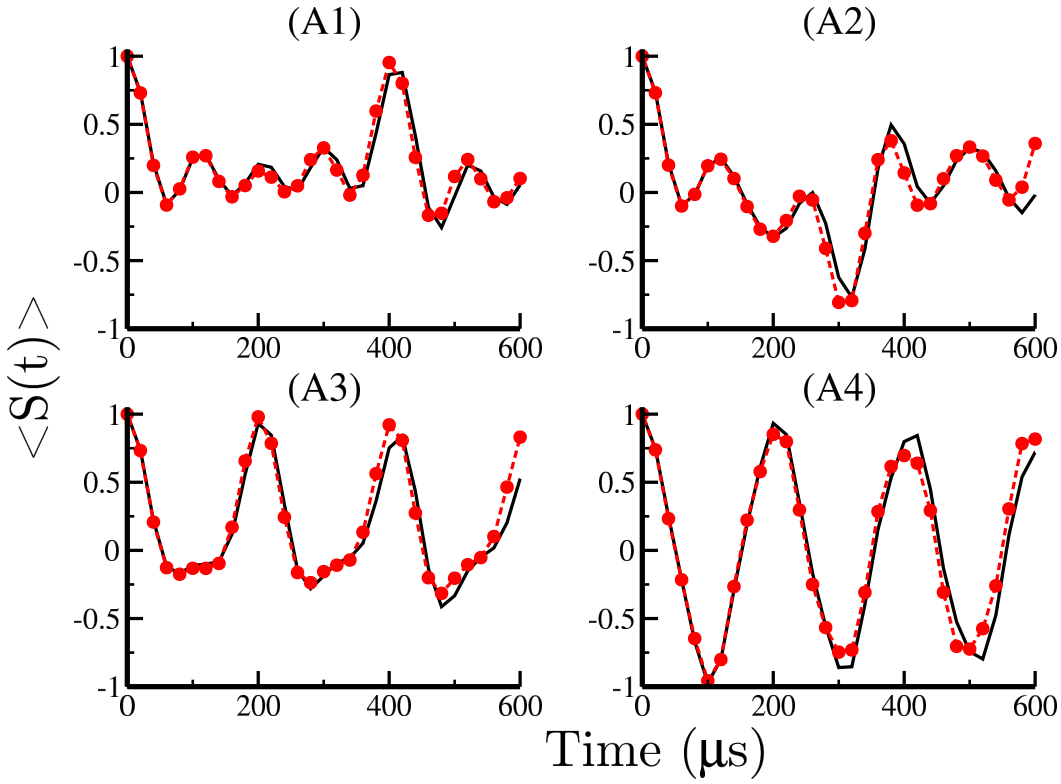

Figure 3.4: In the simulations illustrated, the time domain signal of spin I=1/2 (coupled to spin, S=1) nucleus in a single crystal is depicted for different decoupling field strengths ($\nu_{RF,S}$ = 5 kHz (panel A1), $\nu_{RF,S}$ = 10 kHz (panel A2), $\nu_{RF,S}$ = 20 kHz (panel A3), and $\nu_{RF,S}$ = 40 kHz (panel A4)). The quadrupolar coupling constant (on spin 'S=1') of 2 MHz ($\eta = 1.0$ and $\Omega_{PM} = (0, 90, 0)$), chemical shift parameters on spin 'I', δ = 30.0 kHz (η = 1.0 and $\Omega_{PM} = (0, 90, 0)$, $\omega^{(2)}$ = 5.0 kHz) and dipolar coupling of 8.6 kHz ($\Omega_{PM} = (0, 90, 0)$) are employed. The RF field on spin 'I' ($\nu_{RF,I}$ = 80 kHz) was chosen to be twice of the spinning frequency, ν_r = 40 kHz. The solid lines correspond to numerical simulations [22], while dots (in red) denote analytic simulations based on Eq. (3.25).

Case-II: Single Crystal with general orientation ($\Omega_{PM} = (\alpha, \beta, \gamma)$)

Following the procedure outlined in the previous subsection, the Hamiltonian in the quadrupolar interaction frame is represented by the following equation (analogous to Eq. 3.15).

$$\widetilde{H}(t) = \sum_{m=-2,\neq 0}^{2} \omega_I^{(m)} e^{im\omega_r t}\left[I_Z^{14} + I_Z^{25} + I_Z^{36}\right] + \sum_{m=-2,\neq 0}^{2} 2\omega_{IS}^{(m)} e^{im\omega_r t}\left[I_Z^{13} - I_Z^{46}\right] + \omega_{RF,I}\left[I_X^{14} + I_X^{25} + I_X^{36}\right] + \sqrt{2}\omega_{RF,eff}\left[I_X^{12} + I_X^{23} + I_X^{45} + I_X^{56}\right] \tag{3.26}$$

Accordingly, to facilitate analytic description of the underlying spin dynamics, the above Hamiltonian is transformed using a series of transformations, $U_3 = e^{i\frac{\pi}{2}[I_Y^{14}+I_Y^{25}+I_Y^{36}]}$ and $U_4 = e^{in\omega_r t[I_Z^{14}+I_Z^{25}+I_Z^{36}]}$. Depending upon the choice of the RF amplitude, the CSA and dipolar interaction coefficients corresponding to $m = \pm 1(\omega_{RF,I} = \omega_r)$ or $m = \pm 2(\omega_{RF,I} = 2\omega_r)$ are reintroduced under MAS conditions respectively. Analogous to Case-I, the form of the recoupled Hamiltonian (to zeroth order) is expressed as given below.

$$H_{recoupled} = H_A + H_B \tag{3.27}$$

$$H_A = (\omega_{RF,I} - n\omega_r)\left[I_Z^{14} + I_Z^{25} + I_Z^{36}\right] - k\left|\omega_I^{(n)}\right|\left[I_X^{14} + I_X^{25} + I_X^{36}\right] \tag{3.28}$$

$$H_B = -2k\left|\omega_{IS}^{(n)}\right|\left[I_X^{14} - I_X^{36}\right] + \sqrt{2}\omega_{RF,eff}\left[I_X^{12} + I_X^{23} + I_X^{45} + I_X^{56}\right] \tag{3.29}$$

The term 'k' denotes the scaling factor due to the multiple-pulse sequence [18,21,37] that is employed on 'I' spin for recoupling the CSA interaction.

When the RF amplitude on I-channel is adjusted to one of the matching conditions (n=1 or 2), the longitudinal component in Eq. 3.28 (I_Z^{ij} operator in H_A) becomes zero and the Hamiltonian comprises only the CSA interactions (of spin 'I'). Since evolution under 'H_A' is of relevance in the present study, the recoupled Hamiltonian (Eq. 3.28) is transformed using the transformation function, $U_5 = e^{-i\sqrt{2}\theta_1\left[I_Y^{15}-I_Y^{24}+I_Y^{26}-I_Y^{35}\right]}$, such that the final form of the effective Hamiltonian resembles to the one described by H_A.

$$H_{eff} = U_5 H_{recoupled} U_5^{-1} = -\left(k\left|\omega_I^{(n)}\right| + 2\omega_{eff}\right) I_X^{14} - k\left|\omega_I^{(n)}\right| I_X^{25} - \left(k\left|\omega_I^{(n)}\right| - 2\omega_{eff}\right) I_X^{36} \tag{3.30}$$

$$\tan\theta_1 = \frac{\omega_{RF,eff}}{k\left|\omega_{IS}^{(n)}\right|}\ ,\ \omega_{eff} = k\left|\omega_{IS}^{(n)}\right|\cos\theta_1 + \omega_{RF,eff}\sin\theta_1 \tag{3.31}$$

Following the procedure outlined in the previous subsection, the signal expression at any time 't' is evaluated and given by the following expression.

$$S(t) = \frac{Tr\left[\rho'(t)D'\right]}{Tr\left[\rho(0)^2\right]} = I_1 \cos\left(k\left|\omega_I^{(n)}\right|t\right) + I_2 \cos\left(\omega_{eff}t\right)\cos\left(k\left|\omega_I^{(n)}\right|t\right) + I_3 \cos\left(2\omega_{eff}t\right)\cos\left(k\left|\omega_I^{(n)}\right|t\right) \tag{3.32}$$

where

$$I_1 = \frac{1}{3}\cos^2\left(2\theta_1\right) + \frac{2}{3}\left(\frac{1-\cos\left(2\theta_1\right)}{2}\right)^2, I_2 = \frac{2}{3}\sin^2\left(2\theta\right), I_3 = \frac{2}{3}\left(\frac{1+\cos\left(2\theta_1\right)}{2}\right)^2$$

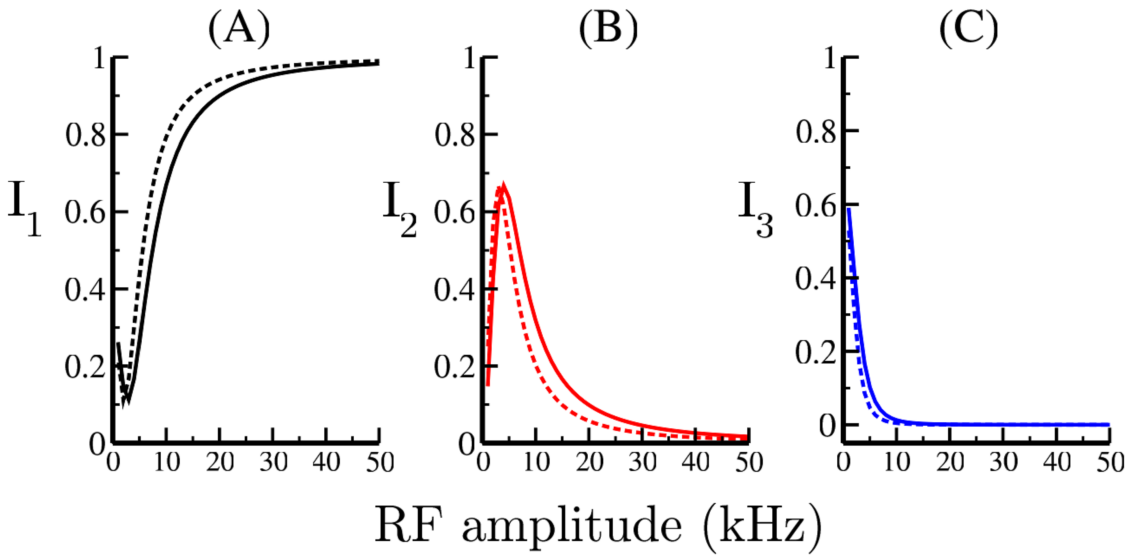

Figure 3.5: In the simulations illustrated, the intensity factors (I_1, I_2 and I_3 in Eq. 3.32) are depicted as a function of the decoupling field strength employed on the quadrupolar spin, S. The other parameters employed in the simulations are given in Table 3.1. The solid lines correspond to plots for spinning frequency, ν_r= 20 kHz while the broken lines correspond to spinning frequency, ν_r= 40 kHz.

The intensity factor, 'I_1' increases at higher RF field strengths with a pronounced decrease in the intensities (I_2 and I_3) associated with the higher frequency terms. This trend is also verified through the analytical expressions and is illustrated pictorially in Figure 3.5. When the dipolar coupling is set to zero (or when perfect decoupling is realized), the signal expression (Eq. 3.32) reduces to the desired form comprising contributions only from CSA interactions.

$$S(t) = Tr\left[\rho'(t)D'\right] = \cos\left(k\left|\omega_I^{(n)}\right|t\right) \tag{3.33}$$

Table 3.1: Description of the parameters employed in the simulations

Parameter	Value
CSA parameters	δ_{CSA}=10 kHz, η=1.0, Ω_{PM}=(10,30,40)
Quadrupolar parameters	C_Q=1 MHz, η=1.0, Ω_{PM}=(30,40,60)
ω_{IS}	8.6 kHz
ω_r	40 kHz

To verify the exactness of the above analytic framework, the time-domain signal from Eq. (3.32) is compared with those obtained from exact numerical methods. In the simulations illustrated in Figure 3.6, the time-domain signal (based on Eq. 3.32) is evaluated at different decoupling field strengths. As illustrated, the analytic simulations are in excellent agreement but for the one depicted in panel A3. This is bit intriguing considering the better agreement (refer to panels A1 and A2) obtained at lower decoupling field strengths.

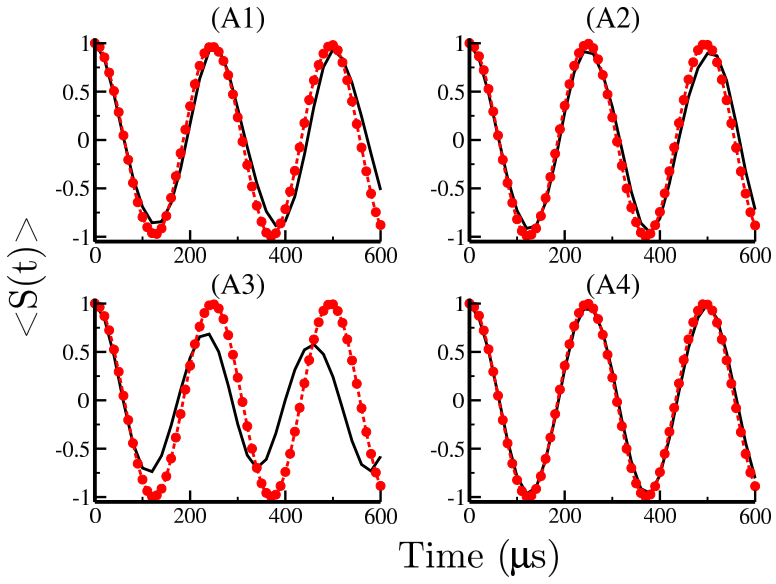

Figure 3.6: In the simulations illustrated, the time domain signal of spin I=1/2 (coupled to spin, S=1) nucleus in a single crystal is depicted for different decoupling field strengths ($\nu_{RF,S}$ = 40 kHz (panel A1), $\nu_{RF,S}$ = 80 kHz (panel A2), $\nu_{RF,S}$ = 100 kHz (panel A3), and $\nu_{RF,S}$ = 150 kHz (panel A4)). The other parameters employed in the simulations are given in Table 3.1. The RF field on spin 'I' ($\nu_{RF,I}$) was chosen to be equal to the spinning frequency, ν_r = 40 kHz. The solid lines correspond to numerical simulations, while dots (in red) denote analytic simulations based on Eq. (3.32).

To explicate this discrepancy observed in the analytic simulations, the form of the Hamiltonians in the quadrupolar interaction frame were examined. In the quadrupolar interaction frame, the magnitude of effective RF field ($\omega_{RF,eff}$) experienced by spin 'S' depends on both the spinning frequency as well as on the amplitude of the decoupling field ($\omega_{RF,S}$). In the simulations depicted in Figure 3.7 (panel A), the dependence of the effective RF field is plotted as a function of the decoupling field strength (employed on the S-channel) at different spinning frequencies (ν_r=20 kHz (black line), ν_r=25 kHz (red line), ν_r=40 kHz (blue line) and ν_r=50 kHz (green line)). As depicted in Figure 3.7 (panel A), the effective RF field experienced by the S-spin in the quadrupolar interaction frame increases with both (i) the RF amplitude and (ii) the spinning frequency. Consequently, the efficiency of decoupling improves resulting in enhanced resolution. In the simulations depicted in Figure 3.7 (panels B1-B4), the time-domain signal at a given RF amplitude is illustrated at different spinning frequencies. As depicted, at a given RF amplitude, the time-domain signal decays slowly (which is desirable in NMR experiments) at faster spinning frequencies and is in accord with simulations presented in panel A. This improvement could be attributed to the scaling factor 'A' ($\omega_{RF,eff} \sim \omega_{RF,S}A$). In the quadrupolar interaction frame, the scaling factor 'A' is proportional to the ratio of the quadrupolar coupling constant to the spinning frequency. At faster spinning frequencies, the Bessel functions represented by $J_0(x)$ tend to approach unity, thereby resulting in improved scaling factors for the decoupling field strength. Consequently, at a given decoupling field strength, the time-domain signal decays slowly at faster spinning frequencies (owing to better scaling factor).

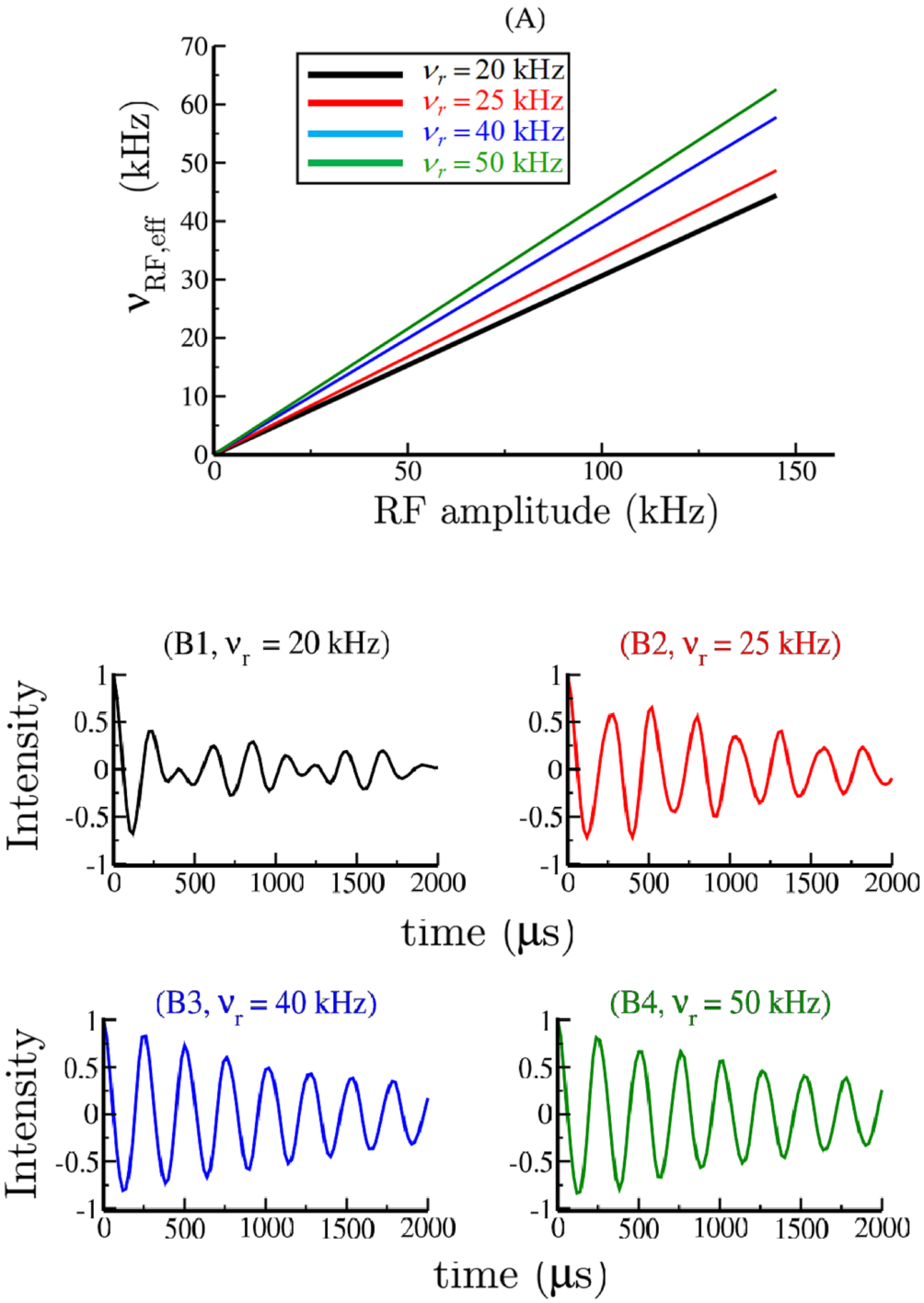

Figure 3.7: In the simulations depicted, the variation of magnitude of effective RF field on quadrupolar channel w.r.t. to RF field is shown in panel A for varying spinning frequencies of 20 kHz (Black line), 25 kHz (red line), 40 kHz (blue line) and 50 kHz (green line). In panel B, Fid spectra corresponding to RF field of 40 kHz is shown at various spinning frequencies of (B1) 20 kHz (B2) 25 kHz (B3) 40 kHz (B4) 50 kHz. The other parameters employed in the simulations are given in Table 3.1. Damping of 500 Hz is used.

In a similar vein, in the simulations depicted in Figure 3.8 (panel A), the dependence of the magnitude of effective RF field is plotted as a function of the spinning frequency at three different decoupling field strengths ($\nu_{RF,S}$=20 kHz (Black line), $\nu_{RF,S}$=40 kHz (red line) and $\nu_{RF,S}$=60 kHz (blue line)). Interestingly, the linear dependence that was observed in Figure 3.7 (panel A) is absent. Due to the oscillatory behaviour of the Bessel functions, at certain spinning frequencies, the effective RF field experienced by the S-spin in the quadrupolar interaction frame tends to zero, despite having a non-zero decoupling field. To verify the exactness of the above analytic insight and explanation, the time-domain signal at four spinning frequencies were calculated. In the simulations depicted in Figure 3.8 (panels B1-B4), time-domain signal at different spinning frequencies (corresponding to the maxima and minima observed in panel A) is illustrated. As depicted, the time-domain signal decays faster at the minima, while it decays slowly at the maxima. Hence, the unitary transformations employed (such as transformation into the quadrupolar interaction frame) in the present analytic framework do have a bearing on the experimental design and optimisation.

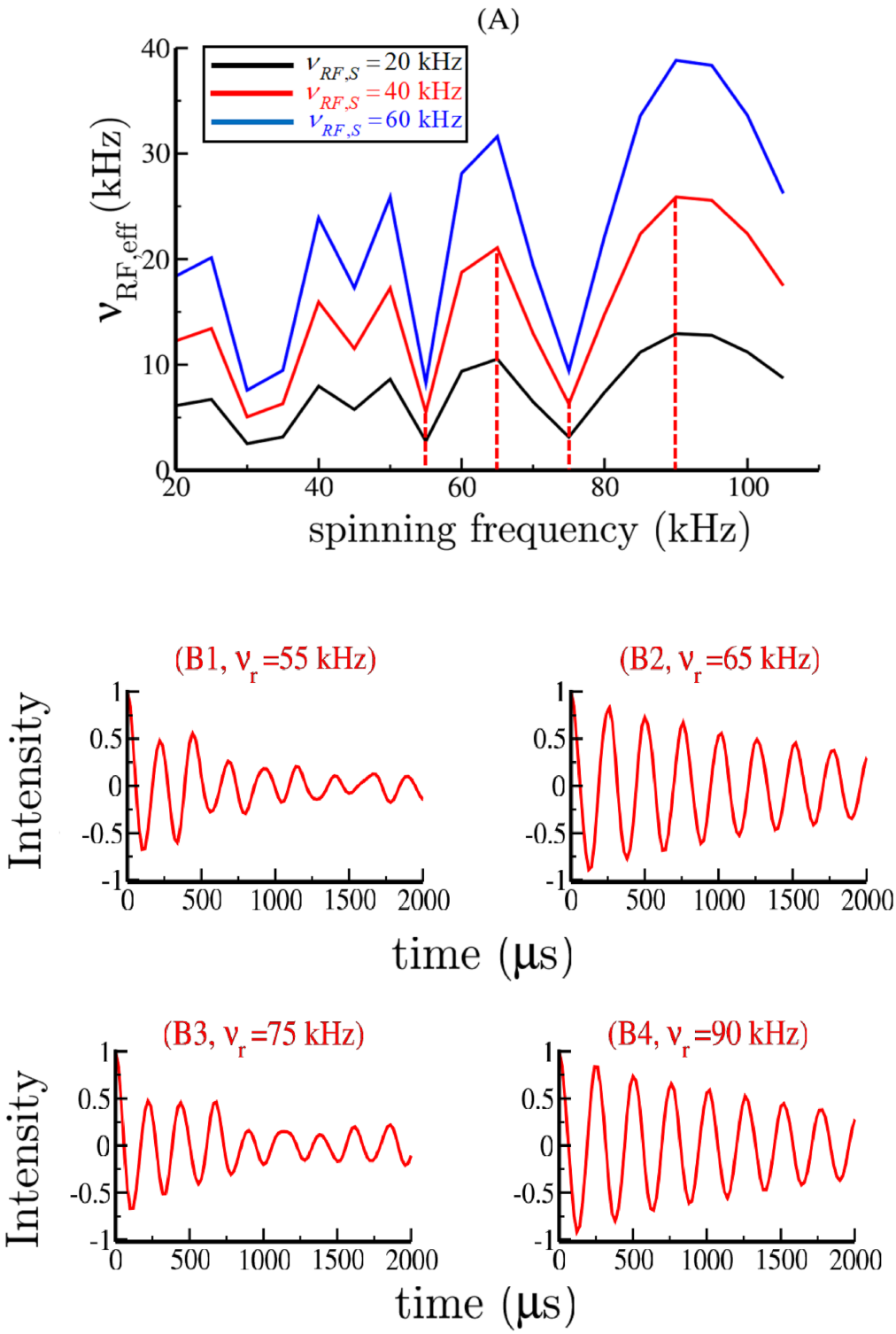

Figure 3.8: In the simulations depicted, the variation of magnitude of effective RF field on quadrupolar channel w.r.t. to spinning frequency is shown in panel A for varying RF fields of 20 kHz (Black line), 40 kHz (red line) and 60 kHz (blue line). In panel B, Fid spectra corresponding to minima and maxima (in panel A) is shown (at constant RF field of 40 kHz) at various spinning frequencies of (B1) 55 kHz (B2) 65 kHz (B3) 75 kHz (B4) 90 kHz. The other parameters employed in the simulations are given in Table 3.1. Damping of 500 Hz is used.

Additional interference effects in single crystal

As depicted in Figure 3.9 (panel A), at higher decoupling field strengths, the magnitude of the effective RF field (in the quadrupolar interaction frame) approaches to that of the spinning frequency (as well as the RF amplitude on spin 'I'). In the present context, when the amplitude of the decoupling field is set to 100 kHz, the effective RF field in the quadrupolar interaction frame (refer panel (A) in Figure 3.9) becomes equal to the spinning frequency, ν_r (ν_r= 40 kHz). Consequently, additional interference effects arise between the decoupling field and spinning frequency. In such cases, to explicate the underlying spin dynamics, the Hamiltonian in the quadrupolar interaction frame is transformed by alternate set of unitary transformations, U_2 $\left(U_2 = e^{i\frac{\pi}{2}[I_Y^{14}+I_Y^{25}+I_Y^{36}]}\right)$, U_3 $\left(U_3 = e^{in\omega_r t[I_Z^{14}+I_Z^{25}+I_Z^{36}]}\right)$ and U_4 ($U_4 = e^{i\omega'_{RF,S}tS_Z}e^{i\frac{\pi}{2}S_y}$). Accordingly, ignoring the high frequency time-dependent terms, the recoupled Hamiltonian is represented by the following equation.

$$H_{eff} = -\left|\omega_I^{(1)}\right| I_X + \left|\omega_{IS}^{(2)}\right| I_X S_X \tag{3.34}$$

It is important to note that in the present context, the $m = \pm 1$ component of CSA interaction is reintroduced, while, only the $m = \pm 2$ component of the heteronuclear dipolar interaction is reintroduced under similar conditions. Accordingly, both the initial density operator ($\rho(0) = I_X = I_X^{14} + I_X^{25} + I_X^{36}$) and detection operator ($D = I_+ = I_+^{14} + I_+^{25} + I_+^{36}$) are transformed and the final signal is evaluated employing the standard procedure summarized below.

$$\rho'(0) = U_4U_3U_2U_1\rho(0)U_1^{-1}U_2^{-1}U_3^{-1}U_4^{-1} = I_Z^{14} + I_Z^{25} + I_Z^{36} \tag{3.35}$$

$$D' = U_4U_3U_2U_1DU_1^{-1}U_2^{-1}U_3^{-1}U_4^{-1} = I_Z^{14} + I_Z^{25} + I_Z^{36} \tag{3.36}$$

$$\rho'(t) = e^{-iH_{eff}t}\rho'(0)e^{iH_{eff}t} = \left[I_Z^{16} + I_Z^{25}\right]\cos\left(\sqrt{\left|\omega_I^{(1)}\right|^2 + 2\left|\omega_{IS}^{(2)}\right|^2}t\right) + I_Z^{34}\cos\left(\left|\omega_I^{(1)}\right|t\right) \tag{3.37}$$

$$S(t) \approx \frac{2}{3}\cos\left(\sqrt{\left|\omega_I^{(1)}\right|^2 + 2\left|\omega_{IS}^{(2)}\right|^2}t\right) + \frac{1}{3}\cos\left(\left|\omega_I^{(1)}\right|t\right) \tag{3.38}$$

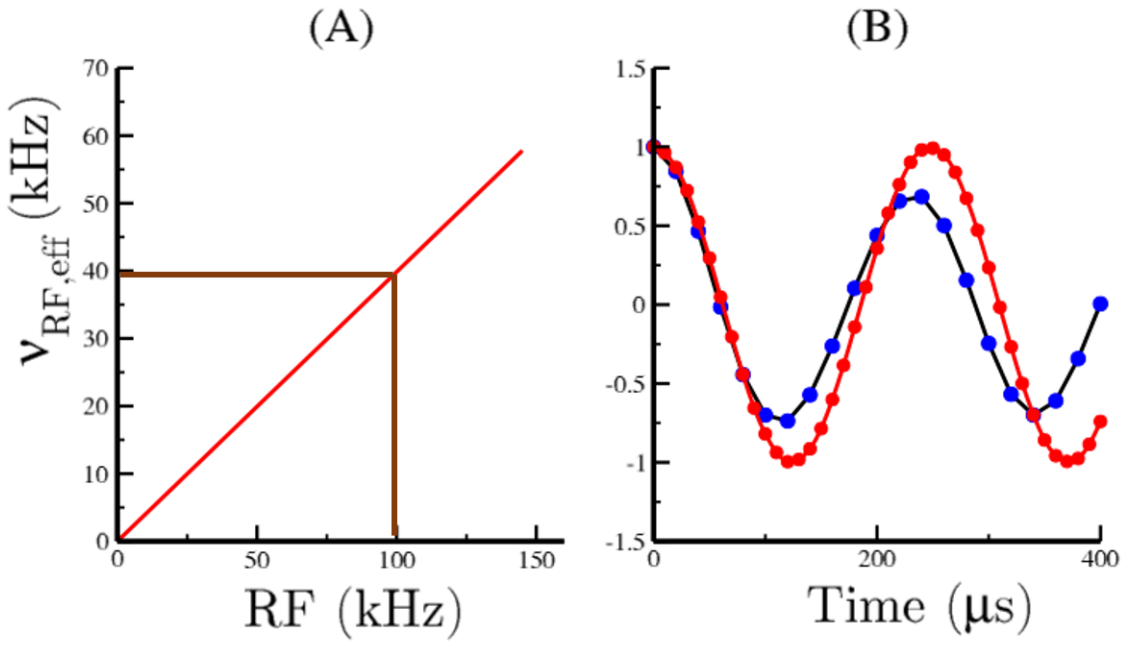

Figure 3.9: In the simulations depicted in panel (A), the effective RF decoupling field on the quadrupolar spin (in the quadrupolar interaction frame) is plotted as a function of the RF field for spinning frequency, $\nu_r = 40$ kHz (red color). In the simulations depicted in panel (B), the time domain signal of spin I=1/2 (coupled to spin, S=1) is depicted for decoupling field strength, $\nu_{RF,S} = 100$ kHz. The analytic simulations indicated in red correspond to Eq. (3.32), while those indicated in blue correspond to Eq. (3.38). The simulations in black correspond to numerical simulations. The other parameters employed in the simulations are given in Table 3.1.

In contrast to the earlier description for single crystal, the allowed transition $|2\rangle \rightarrow |5\rangle$ has significant contributions from the recoupled dipolar interactions and is primarily responsible for compromising the spectral resolution. As depicted in Figure 3.9 (panel B), the analytic simulations (blue dots) based on Eq. (3.38) are in excellent agreement to those obtained from exact numerical methods and justify the proposed analytic description.

Case-III: Powder Sample

In a typical powder sample, due to orientation dependence of the quadrupolar coupling constant, the scaling factor 'A' differs for different crystallite orientations. Accordingly, the scaling factor 'A' gets modified in a powder sample.

$$A(\alpha\beta\gamma) = \sum_{n_1} J_{n_1}(A_1(\alpha\beta\gamma)) \sum_{n_2} J_{n_2}(A_2(\alpha\beta\gamma)) \sum_{n_3} J_{n_3}(A_3(\alpha\beta\gamma)) \sum_{n_4} J_{n_4}(A_4(\alpha\beta\gamma))$$
$$n_1 + n_2 + n_3 + n_4 = 0 \tag{3.39}$$

Consequently, the effective decoupling field strength on the quadrupolar spin 'S' varies and the interference effects mentioned in the previous subsections remain unobserved. Hence, at higher decoupling field strengths, increase in resolution is observed in powder sample (refer to Figure 3.2).

3.3 Polarisation transfer from spin I=1/2 to S=1

To explicate the factors governing the polarisation transfer [38–41] in systems comprising quadrupolar spins (say spin S=1), polarisation transfer from spin I=1/2 to spin S=1 is examined in this section. In the numerical simulations illustrated in Figure 3.10, polarisation transfer from spin I=1/2 to S=1 is monitored as a function of the mixing time in systems with differing quadrupolar coupling constants.

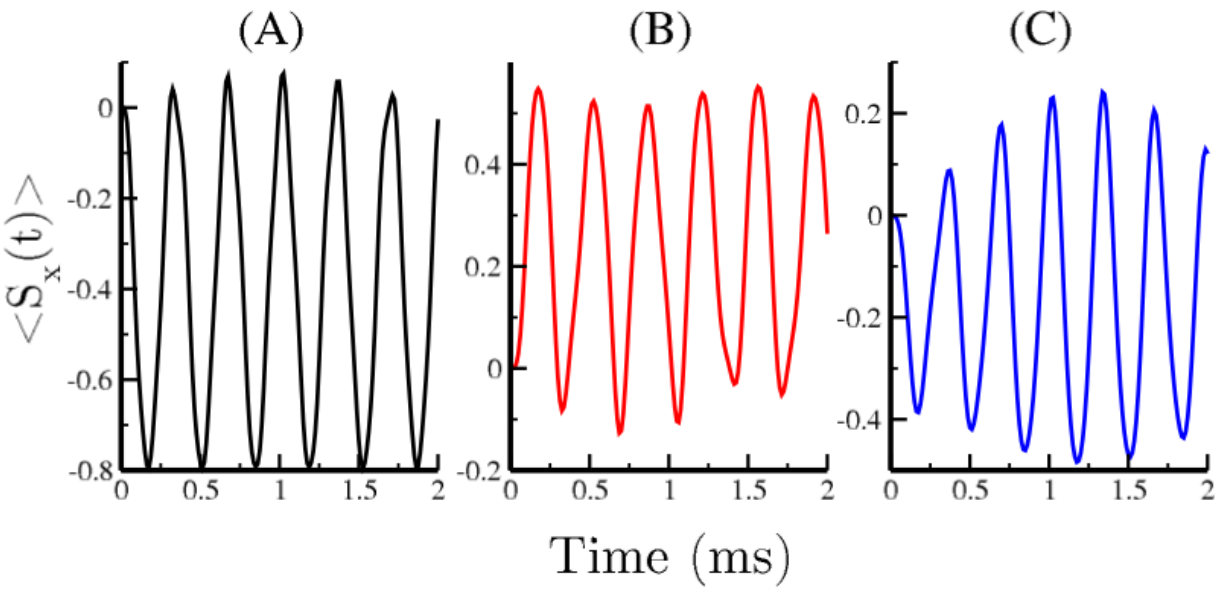

Figure 3.10: In the numerical simulations illustrated, polarisation transfer from spin I=1/2 to spin S=1 is depicted as a function of mixing time for spinning frequency, $\nu_r = 40$ kHz. The RF parameters on spins I and S are carefully adjusted to the DQ matching condition. The dipolar coupling of 8.6 kHz ($\Omega_{PM} = (0, 90, 0)$) is employed while the quadrupolar coupling constant (on spin 'S') is varied as- (A) 500 kHz (B) 1 MHz (C) 2 MHz with $\eta = 1.0$ and $\Omega_{PM} = (0, 90, 0)$.

In the simulations depicted, the spinning frequency is held constant (identical in all panels) and the RF amplitudes employed on the spins (I and S) are carefully adjusted such that the sum of the effective fields on the spins (I and S) is matched to an integer multiple of the spinning frequency (i.e. $\nu_{eff,I} + \nu_{eff,S} = 2\nu_r$). All other parameters (inclusive of the dipolar coupling constant) are identical in the panels. Although, the dipolar coupling constant and matching conditions are identical in the simulations, the exchange trajectories (in particular the sign) are different in the panels. This is bit intriguing considering the fact that the efficiency of polarisation transfer among spin-1/2 nuclei is primarily dependent on the dipolar coupling constant and the matching conditions (either zero-quantum (ZQ) or double-quantum (DQ)) employed in the experiment. Accordingly, in the case of spin-1/2 nuclei, the exchange trajectories corresponding to the DQ matching condition have a negative sign, while, a positive sign is observed for ZQ matching condition. Interestingly, such clear demarcations are absent in the exchange trajectories depicted in Figure 3.10. To explain this interesting observation, we begin with a formal description of the spin dynamics as given below.

For operational purposes, we begin with the Hamiltonian of an isolated spin pair (spin I=1/2 coupled to spin S=1) in the rotating frame (CSA on I-spin is set to zero).

$$H(t) = H_{I,RF}(t) + H_{S,Q}(t) + H_{S,RF}(t) + H_{IS}(t) \tag{3.40}$$

Following the procedure outlined in section 3.2, the above Hamiltonian is transformed into the quadrupolar interaction frame [28–34] (defined by $U_1 = e^{i\Phi(t)[I_Z^{12} - I_Z^{23} + I_Z^{45} - I_Z^{56}]}$) resulting in the following form of the transformed Hamiltonian.

$$\widetilde{H}(t) = U_1 H(t) U_1^{-1} = H_{I,RF}(t) + \widetilde{H}_{S,RF}(t) + H_{IS}(t) \tag{3.41}$$

$$\begin{aligned}\widetilde{H}_{S,RF}(t) = U_1 H_{S,RF}(t) U_1^{-1} &= \sqrt{2}\omega_{RF,S} A \left[I_X^{12} + I_X^{23} + I_X^{45} + I_X^{56}\right] \\ &+ \sqrt{2}\omega_{RF,S} \sum_n A_{X,n} e^{in\omega_r t} \left[I_X^{12} + I_X^{23} + I_X^{45} + I_X^{56}\right] \\ &+ \sqrt{2}\omega_{RF,S} \sum_n B_{Y,n} e^{in\omega_r t} \left[I_Y^{12} - I_Y^{23} + I_Y^{45} - I_Y^{56}\right]\end{aligned} \tag{3.42}$$

where

$$A = \sum_{n_1} J_{n_1}(A_1) \sum_{n_2} J_{n_2}(A_2) \sum_{n_3} J_{n_3}(A_3) \sum_{n_4} J_{n_4}(A_4) \;\; ; \;\; n_1 + n_2 + n_3 + n_4 = 0$$

To describe the spin dynamics, we consider the special case of a single crystal wherein the orientation dependence of all the internal interactions (i.e. Quadrupolar interaction on

S-spin and dipolar coupling between I and S spin) are set to $\Omega_{PM} = (0, 90, 0)$. Under such conditions, only one of the components of the internal interactions is present ($\omega_{\lambda}^{(\pm 1)=0}$ where λ= dipolar or quadrupolar interaction). Subsequently, the Hamiltonian in the quadrupolar interaction frame (Eq. 3.41) reduces down to a simpler form given below.

$$\begin{aligned}\widetilde{H}(t) = U_1 H(t) U_1^{-1} &= \omega_{RF,I}\left[I_X^{14} + I_X^{25} + I_X^{36}\right] \\ &+ 4\omega_{IS}^{(2)}\cos(2\omega_r t)\left[I_Z^{13} - I_Z^{46}\right] + \sqrt{2}\omega_{RF,S}J_0(A)\left[I_X^{12} + I_X^{23} + I_X^{45} + I_X^{56}\right] \\ &+ \sqrt{2}\omega_{RF,S}\sum_{k=\pm 4,\pm 8,..} J_{k/2}(A)\, e^{ik\omega_r t}\left[I_X^{12} + I_X^{23} + I_X^{45} + I_X^{56}\right] \\ &+ i\sqrt{2}\omega_{RF,S}\sum_{m=\pm 2,\pm 6,..} J_{m/2}(A)\, e^{im\omega_r t}\left[I_Y^{12} - I_Y^{23} + I_Y^{45} - I_Y^{56}\right] \end{aligned} \tag{3.43}$$

where $A = \dfrac{\omega_Q^{(2)}}{2\omega_r}$ represents the argument of the Bessel function [35].

Employing the Magnus formula [36], time-dependent contributions to the Hamiltonian on the S-channel is derived and summarized by the following equation.

$$\begin{aligned}\bar{H} = \bar{H}^{(1)} + \bar{H}^{(2)} &= \sqrt{2}\omega_{RF,S}J_0(A)\left[I_X^{12} + I_X^{23} + I_X^{45} + I_X^{56}\right] \\ &- \frac{2\omega_{RF,S}^2}{\omega_r}J_0(A)\left\{\sum_{n=2p-1}\frac{J_n(A)}{n}\right\}\left[I_Z^{12} - I_Z^{23} + I_Z^{45} - I_Z^{56} + I_X^{13} + I_X^{46}\right]\end{aligned} \tag{3.44}$$

Analogous to the description in the previous section, the Hamiltonian, $\bar{H}$ is transformed (using unitary transformation, $U_2 = e^{\frac{i\theta[I_Y^{12} - I_Y^{23}]}{\sqrt{2}}}$, $\tan\theta = \dfrac{\frac{2\omega_{RF,S}^2 J_0(A)}{\omega_r}\left[\sum_{n=2p-1}\frac{J_n(A)}{n}\right]}{\omega_{RF,S}J_0(A)}$)) such that the Hamiltonian reduces to a form comprising commuting set of operators.

$$\begin{aligned}H_{eff} &= U_2\bar{H}U_2^{-1} \\ &= \left\{\frac{\omega_{RF,S}J_0(A)}{\sqrt{2}}\cos\theta + \frac{\sqrt{2}\omega_{RF,S}^2}{\omega_r}J_0(A)\left\{\sum_{n=2p-1}\frac{J_n(A)}{n}\right\}\sin\theta\right\}\left[I_X^{12} + I_X^{23} + I_X^{45} + I_X^{56}\right] \\ &= \sqrt{2}\omega_{RF,eff}\left[I_X^{12} + I_X^{23} + I_X^{45} + I_X^{56}\right]\end{aligned} \tag{3.45}$$

Employing the above form of effective RF Hamiltonian on S-channel (Eq. 3.45), the total Hamiltonian of the system (Eq. 3.43) reduces to a simpler form given below.

$$\begin{aligned}\widetilde{H}(t) &= \omega_{RF,I}\left[I_X^{14} + I_X^{25} + I_X^{36}\right] \\ &+ 4\omega_{IS}^{(2)}\cos(2\omega_r t)\left[I_Z^{13} - I_Z^{46}\right] + \sqrt{2}\omega_{RF,eff}\left[I_X^{12} + I_X^{23} + I_X^{45} + I_X^{56}\right]\end{aligned} \tag{3.46}$$

To quantize the RF fields (employed on both channels) along the Z-direction, the above Hamiltonian (Eq. 3.46) is further transformed by the unitary transformation, $U_3 =$

$e^{i\frac{\pi}{2}[I_Y^{14}+I_Y^{25}+I_Y^{36}]} e^{i\sqrt{2}\frac{\pi}{2}[I_Y^{12}+I_Y^{23}+I_Y^{45}+I_Y^{56}]}$.

$$\widetilde{H}(t) = \omega_{RF,I}\left[I_Z^{14}+I_Z^{25}+I_Z^{36}\right]+\omega_{RF,eff}\left[I_Z^{13}+I_Z^{46}\right]+2\sqrt{2}\omega_{IS}^{(2)}\cos\left(2\omega_r t\right)\left[I_X^{15}+I_X^{24}+I_X^{26}+I_X^{35}\right] \tag{3.47}$$

To deduce the matching conditions in polarisation transfer experiments, the above Hamiltonian is further transformed by the unitary transformation, $U_4 = e^{it\omega_{RF,I}[I_Z^{14}+I_Z^{25}+I_Z^{36}]}e^{it\omega_{RF,eff}[I_Z^{13}+I_Z^{46}]}$.

$$\widetilde{\widetilde{H}}(t) = \sqrt{2}\omega_{IS}^{(2)}\cos\left(2\omega_r t\right)\left[\begin{array}{l}\left\{I_+^{15}+I_+^{26}\right\}e^{i\omega_{RF,I}t}e^{i\omega_{RF,eff}t}+\left\{I_-^{51}+I_-^{62}\right\}e^{-i\omega_{RF,I}t}e^{-i\omega_{RF,eff}t}\\ +\left\{I_+^{24}+I_+^{35}\right\}e^{i\omega_{RF,I}t}e^{-i\omega_{RF,eff}t}+\left\{I_-^{42}+I_-^{53}\right\}e^{-i\omega_{RF,I}t}e^{i\omega_{RF,eff}t}\end{array}\right] \tag{3.48}$$

As depicted above, depending on the matching conditions [42,43] (between the RF field on I-channel, effective RF field on S-channel and spinning frequency), a part of the dipolar Hamiltonian becomes time-independent and gets reintroduced under MAS conditions, resulting in polarisation transfer. It is important to note that the effective RF field on the quadrupolar spin ($\omega_{RF,eff}$) depends on the ratio of the quadrupolar coupling constant to spinning frequency of the system via the argument of the Bessel function i.e. $A = \frac{\omega_Q^{(2)}}{2\omega_r}$. Depending on the matching conditions, the form of the recoupled Hamiltonian differs and is derived accordingly as given below.

(i) DQ matching condition- When the sum of the effective fields on the two channels (I and S) is matched to twice the spinning frequency (i.e. $\omega_{RF,I}+\omega_{RF,eff} = 2\omega_r$), the Hamiltonian reduces to a simple form given below.

$$H_{eff} = \sqrt{2}\omega_{IS}^{(2)}\left[I_X^{15}+I_X^{26}\right] \tag{3.49}$$

(ii) ZQ matching condition- When the difference of the effective fields on the two channels (I and S) is matched to twice the spinning frequency (i.e. $\omega_{RF,I}-\omega_{RF,eff} = 2\omega_r$), the Hamiltonian reduces to a simple form given below.

$$H_{eff} = \sqrt{2}\omega_{IS}^{(2)}\left[I_X^{24}+I_X^{35}\right] \tag{3.50}$$

To maintain consistency, both the initial density operator ($\rho(0) = I_X = I_X^{14}+I_X^{25}+I_X^{36}$) and detection operator, $D = I_+ = I_+^{14}+I_+^{25}+I_+^{36}$ (for I-spin) and $D = S_X = \sqrt{2}I_X^{12}+I_X^{23}+I_X^{45}+I_X^{56}$ (for S-spin) are transformed by the same set of transformations.

$$\rho'(0) = U_4U_3U_2U_1\rho(0)U_1^{-1}U_2^{-1}U_3^{-1}U_4^{-1} = I_Z^{14}+I_Z^{25}+I_Z^{36} \tag{3.51}$$

For I-spin,

$$D' = U_4U_3U_2U_1DU_1^{-1}U_2^{-1}U_3^{-1}U_4^{-1} = I_Z^{14}+I_Z^{25}+I_Z^{36} \tag{3.52}$$

For S-spin,

$$D' = U_4U_3U_2U_1DU_1^{-1}U_2^{-1}U_3^{-1}U_4^{-1} = 2J_0\left(A\right)\left[I_Z^{13} + I_Z^{46}\right] \tag{3.53}$$

Accordingly, depending on the matching conditions, the form of the density operator at time 't' is evaluated employing the appropriate effective Hamiltonians.

(a) DQ matching conditions

$$\rho'(t) = e^{-iH_{eff}t}\rho'(0)e^{iH_{eff}t} = I_Z^{34} + \cos\left(\sqrt{2}\omega_{IS}^{(2)}t\right)\left[I_Z^{15} + I_Z^{26}\right] - \sin\left(\sqrt{2}\omega_{IS}^{(2)}t\right)\left[I_Y^{15} + I_Y^{26}\right] \tag{3.54}$$

(b) ZQ matching conditions

$$\rho'(t) = e^{-iH_{eff}t}\rho'(0)e^{iH_{eff}t} = I_Z^{16} + \cos\left(\sqrt{2}\omega_{IS}^{(2)}t\right)\left[I_Z^{24} + I_Z^{35}\right] - \sin\left(\sqrt{2}\omega_{IS}^{(2)}t\right)\left[I_Y^{24} + I_Y^{35}\right] \tag{3.55}$$

Subsequently, employing the density operator at time 't', the final form of the normalized signal ($Tr\left[\rho(0)^2 = \frac{3}{2}\right]$) is derived and summarised below. The final form of the signal expression (for 'I' spin) remains identical for both the matching conditions.

$$S(t) = \langle I_+\left(t\right)\rangle = \frac{Tr\left[\rho'(t)D'\right]}{Tr\left[\rho(0)^2\right]} = \frac{1}{3} + \frac{2}{3}\cos\left(\sqrt{2}\omega_{IS}^{(2)}t\right) \tag{3.56}$$

However, the final form of the signal expression for 'S-spin' varies and is summarised by the following equations.

For DQ matching condition,

$$S(t) = \langle S_X\left(t\right)\rangle = \frac{Tr\left[\rho'(t)D'\right]}{Tr\left[\rho(0)^2\right]} = -\frac{2}{3}J_0\left(A\right)\left\{1 - \cos\left(\sqrt{2}\omega_{IS}^{(2)}t\right)\right\} \tag{3.57}$$

For ZQ matching condition,

$$S(t) = \langle S_X\left(t\right)\rangle = \frac{Tr\left[\rho'(t)D'\right]}{Tr\left[\rho(0)^2\right]} = \frac{2}{3}J_0\left(A\right)\left\{1 - \cos\left(\sqrt{2}\omega_{IS}^{(2)}t\right)\right\} \tag{3.58}$$

As depicted above, the signal expression (for the S spin) in the case of DQ matching condition has a negative sign in comparison to the one obtained from the ZQ matching condition. This trend is very similar to those obtained in heteronuclear cross-polarisation (CP) experiments involving spin-1/2 nuclei (I=S=1/2) [44].

To verify the exactness of the above analytic framework, the time-domain signal obtained from Eq. (3.56-3.58) is compared with those obtained from exact numerical methods [22]. As illustrated, the analytic simulations are in excellent agreement for DQ matching condition (Fig 3.11) and for ZQ matching condition (Fig 3.12) validating the proposed analytic framework.

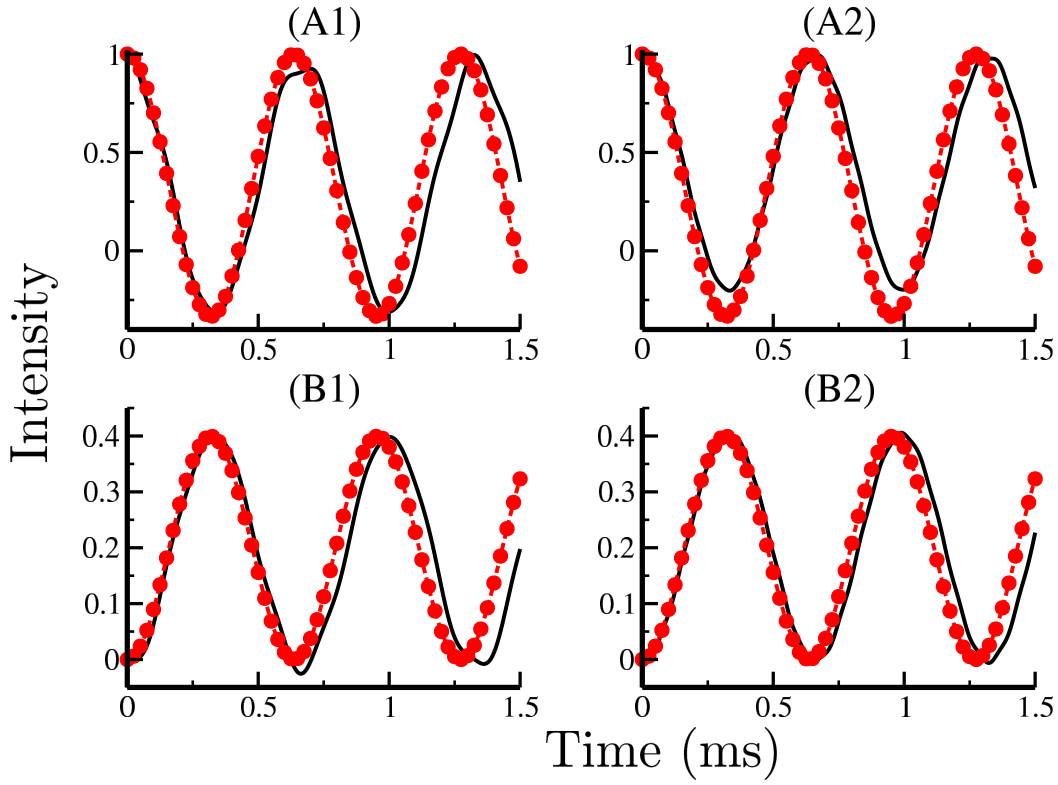

Figure 3.11: In the simulations illustrated, the time domain signal of spin I=1/2 (coupled to spin, S=1) nucleus in a single crystal is depicted for varying RF field strengths for DQ matching condition. The quadrupolar coupling constant (on spin 'S') of 1 MHz ($\eta = 1.0$ and $\Omega_{PM} = (0, 90, 0)$), dipolar coupling of 4.4 kHz ($\Omega_{PM} = (0, 90, 0)$) and spinning frequency, $\nu_r = 40$ kHz are employed. The upper row (panels A1 and A2) correspond to I-spin detection, while the bottom row (panels B1 and B2) correspond to S-spin detection. The parameters are- (A1, B1) $\nu_{RF,I} = 83$ kHz, $\nu_{RF,S} = 10$ kHz,(A2, B2) $\nu_{RF,I} = 86.5$ kHz, $\nu_{RF,S} = 20$ kHz. The solid lines correspond to numerical simulations [22], while dots (in red) denote analytic simulations (based on Eq. 3.56 for upper row and Eq. 3.57 for bottom row).

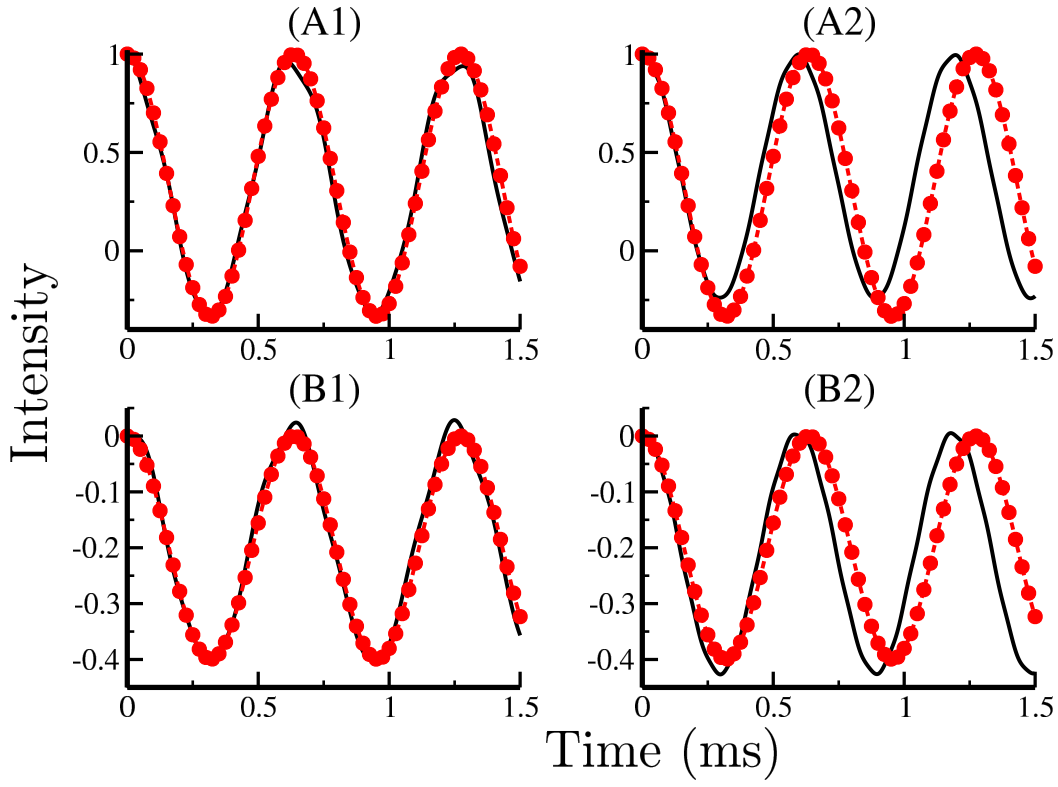

Figure 3.12: In the simulations illustrated, the time domain signal of spin I=1/2 (coupled to spin, S=1) nucleus in a single crystal is depicted for varying RF field strengths for ZQ matching condition. The quadrupolar coupling constant (on spin 'S') of 1 MHz ($\eta = 1.0$ and $\Omega_{PM} = (0, 90, 0)$), dipolar coupling of 4.4 kHz ($\Omega_{PM} = (0, 90, 0)$) and spinning frequency, $\nu_r = 40$ kHz are employed. The upper row (panels A1 and A2) correspond to I-spin detection, while the bottom row (panels B1 and B2) correspond to S-spin detection. The parameters are- (A1, B1) $\nu_{RF,I} = 77$ kHz, $\nu_{RF,S} = 10$ kHz,(A2, B2) $\nu_{RF,I} = 73.5$ kHz, $\nu_{RF,S} = 20$ kHz. The solid lines correspond to numerical simulations [22], while dots (in red) denote analytic simulations (based on Eq. 3.56 for upper row and Eq. 3.58 for bottom row).

Depending on the sign of the $J_0(A)$ coefficient, the overall sign of the effective field on the quadrupolar spin varies resulting in different trajectories. This is illustrated below in Figure 3.13, wherein, the $J_0(A)$ coefficient for a given quadrupolar coupling constant is plotted as a function of the spinning frequency. As depicted in Figure 3.13, depending on the spinning frequency, the sign of the $J_0(A)$ coefficient alternates between +ve and -ve signs for a given quadrupolar coupling constant. Accordingly, depending on the sign of the $J_0(A)$ coefficient (It is +ve for Cq=500 kHz (panel A), Cq=2 MHz (panel C) and -ve for Cq=1 MHz (panel B)), the sign of the exchange trajectories depicted in Figure 3.10 vary.

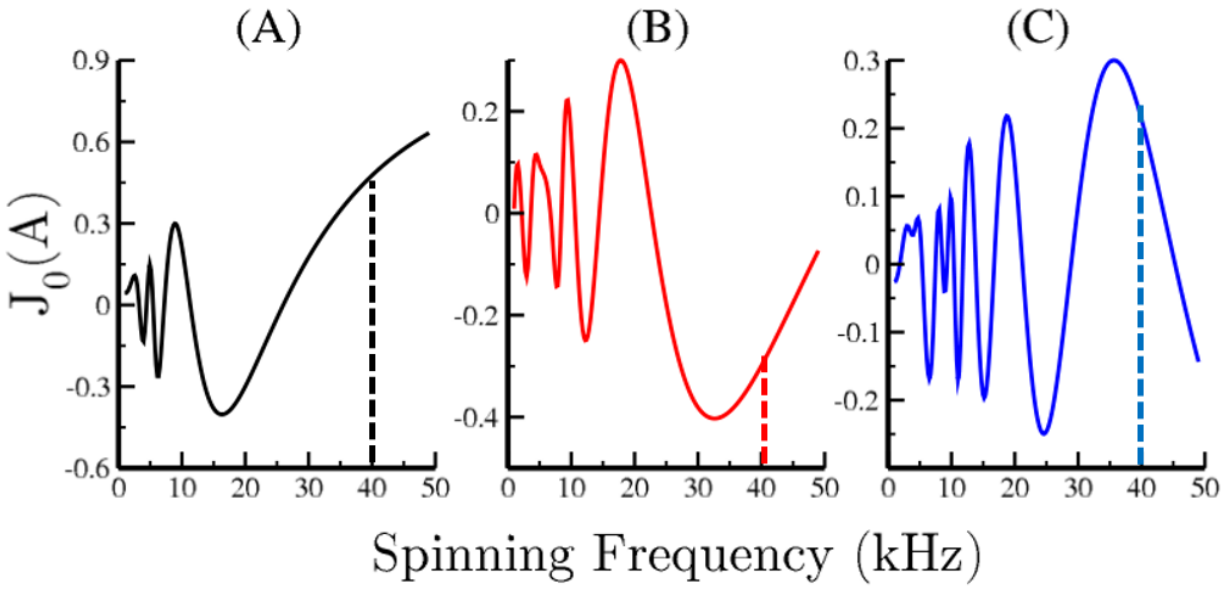

Figure 3.13: In the simulations illustrated, the $J_0(A)$ coefficient is depicted as a function of the spinning frequency for different quadrupolar coupling constants of (A) 500 kHz (B) 1 MHz (C) 2 MHz with $\eta = 1.0$ and $\Omega_{PM} = (0, 90, 0)$ employed on S=1 spin.

Hence, in contrast to polarisation transfer among spin-1/2 nuclei, polarisation transfer from spin I=1/2 nucleus to spin S=1 has an explicit dependence on the sign of bessel function ($J_0(A)$) which further depends on the quadrupolar coupling constant and spinning frequency.

3.4 Summary

In summary, the present chapter highlights the relevance of the transformations employed in analytic methods for studying MAS experiments involving quadrupolar spins. Although, the transformation into the quadrupolar interaction frame seems only a mathematical procedure/necessity in theoretical descriptions, its role in explicating the experimental observations seems interesting as well as puzzling. In addition to the dependence on the internal parameters (such as quadrupolar coupling constant and dipolar coupling constant) and the external parameters (such as RF amplitude, spinning frequency etc.), the properties of the Bessel functions (inclusive of sign) employed in the analytic treatments do play an important role in explicating the results observed in the simulations.

References

[1] S. E. Ashbrook and M. J. Duer, *Concepts in Magnetic Resonance Part A: An Educational Journal*, 2006, **28**, 183–248.

[2] R. E. Wasylishen, S. E. Ashbrook and S. Wimperis, *NMR of Quadrupolar Nuclei in Solid Materials*, John Wiley & Sons, 2012.

[3] Y. Nishiyama, G. Hou, V. Agarwal, Y. Su and A. Ramamoorthy, *Chemical Reviews*, 2023, **123**, 918–988.

[4] B. Reif, S. E. Ashbrook, L. Emsley and M. Hong, *Nature Reviews Methods Primers*, 2021, **1**, 4.

[5] R. Zhang, K. H. Mroue and A. Ramamoorthy, *Accounts of Chemical Research*, 2017, **50**, 1105–1113.

[6] A. Samoson, T. Tuherm and Z. Gan, *Solid State Nuclear Magnetic Resonance*, 2001, **20**, 130–136.

[7] Y. Nishiyama, *Solid State Nuclear Magnetic Resonance*, 2016, **78**, 24–36.

[8] J. R. Lewandowski, M. E. Halse, M. Blackledge and L. Emsley, *Science*, 2015, **348**, 578–581.

[9] G. Comellas and C. M. Rienstra, *Annual Review of Biophysics*, 2013, **42**, 515–536.

[10] A. Ramamoorthy, *NMR Spectroscopy of Biological Solids*, CRC Press, 2005.

[11] C. P. Jaroniec, *Solid State Nuclear Magnetic Resonance*, 2012, **43**, 1–13.

[12] C. P. Jaroniec, *Journal of Magnetic Resonance*, 2019, **306**, 42–47.

[13] M. Stoll, R. Vaughan, R. Saillant and T. Cole, *The Journal of Chemical Physics*, 1974, **61**, 2896–2899.

[14] M. Alla, E. Kundla and E. Lippmaa, *Soviet Journal of Experimental and Theoretical Physics Letters*, 1978, **27**, 194.

[15] A. Naito, S. Ganapathy and C. A. McDowell, *The Journal of Chemical Physics*, 1981, **74**, 5393–5397.

[16] A. Naito, S. Ganapathy, K. Akasaka and C. A. McDowell, *The Journal of Chemical Physics*, 1981, **74**, 3190–3197.

[17] J. G. Hexem, M. H. Frey and S. J. Opella, *The Journal of Chemical Physics*, 1982, **77**, 3847–3856.

[18] D. H. Brouwer and J. A. Ripmeester, *Journal of Magnetic Resonance*, 2007, **185**, 173–178.

[19] R. M. Orr and M. J. Duer, *Solid State Nuclear Magnetic Resonance*, 2006, **30**, 130–134.

[20] R. S. Stein, B. Elena and L. Emsley, *Chemical Physics Letters*, 2008, **458**, 391–395.

[21] M. K. Pandey and Y. Nishiyama, *Journal of Magnetic Resonance*, 2015, **261**, 133–140.

[22] M. Bak, J. T. Rasmussen and N. C. Nielsen, *Journal of Magnetic Resonance*, 2000, **147**, 296–330.

[23] M. Veshtort and R. G. Griffin, *Journal of Magnetic Resonance*, 2006, **178**, 248–282.

[24] D. L. VanderHart, H. S. Gutowsky and T. C. Farrar, *Journal of the American Chemical Society*, 1967, **89**, 5056–5057.

[25] N. Zumbulyadis, P. M. Henrichs and R. H. Young, *The Journal of Chemical Physics*, 1981, **75**, 1603–1611.

[26] S. Ding and C. A. McDowell, *The Journal of Chemical Physics*, 1997, **107**, 7762–7772.

[27] C. Grey and W. Veeman, *Chemical Physics Letters*, 1992, **192**, 379–385.

[28] J. Pratt, *Molecular Physics*, 1977, **34**, 539–555.

[29] P. Caravatti, G. Bodenhausen and R. Ernst, *Journal of Magnetic Resonance (1969)*, 1983, **55**, 88–103.

[30] R. Reddy and P. Narasimhan, *Molecular Physics*, 1991, **72**, 491–507.

[31] R. Reddy and P. Narasimhan, *Molecular Physics*, 1991, **72**, 509–521.

[32] M. Bansal and R. Ramachandran, *Journal of Magnetic Resonance Open*, 2022, **10**, 100042.

[33] M. Bansal and R. Ramachandran, *Physical Chemistry Chemical Physics*, 2022, **24**, 29092.

[34] N. Bamola, M. Bansal and R. Ramachandran, *Physical Chemistry Chemical Physics*, 2023, **25**, 17877–17900.

[35] G. B. Arfken, H. J. Weber and F. E. Harris, *Mathematical Methods for Physicists, 7th ed*, Academic Press, 2013.

[36] W. Magnus, *Communications on Pure and Applied Mathematics*, 1954, **7**, 649–673.

[37] M. H. Levitt, D. M. Grant and R. K. Harris, *Solid State NMR Studies of Biopolymers; McDermott, AE; Polenova, T., Eds*, 2007, 229.

[38] M. Pruski, D. Lang, C. Fernandez and J. Amoureux, *Solid State Nuclear Magnetic Resonance*, 1997, **7**, 327–331.

[39] C. Fernandez, L. Delevoye, J.-P. Amoureux, D. Lang and M. Pruski, *Journal of the American Chemical Society*, 1997, **119**, 6858–6862.

[40] S. E. Ashbrook, S. P. Brown and S. Wimperis, *Chemical Physics Letters*, 1998, **288**, 509–517.

[41] S. E. Ashbrook and S. Wimperis, *Journal of Magnetic Resonance*, 2000, **147**, 238–249.

[42] A. J. Vega, *Journal of Magnetic Resonance (1969)*, 1992, **96**, 50–68.

[43] A. J. Vega, *Solid State Nuclear Magnetic Resonance*, 1992, **1**, 17–32.

[44] M. K. Pandey, Z. Qadri and R. Ramachandran, *The Journal of Chemical Physics*, 2013, **138**, 114108–114118.

Chapter 4

Conclusions and Perspectives

With the development of high field magnets and ultrafast MAS probes, significant advancements have emerged on the experimental front using the state of the art instrumentation. Nevertheless, quantifying experimental data through reliable analytic models has remained challenging owing to the presence of non-commuting time-dependent Hamiltonians of differing magnitudes. While analytic description of finite pulse effects in spin-1/2 systems in rotating solids is possible in majority of cases, such descriptions in the case of quadrupolar spins (I>1/2) are less prevalent. Although, development of analytic methods in static samples involving quadrupolar spins have enhanced our understanding of the experiments, straightforward extension of these methods in rotating samples is less trivial. In the present thesis, an attempt has been made to address this issue.

To present a pedagogical approach, a detailed description of the finite pulse effects in isolated spins under MAS is outlined in Chapter-2. Employing the tenets of perturbation theory, the role of interaction frames in the overall convergence of the corrections (to the effective Hamiltonians) was derived initially in spin-1/2 systems and discussed within the frameworks of Average Hamiltonian theory (AHT) and Floquet theory. Based on the insights derived from the study of spin-1/2 systems, the utility of analytic methods in the description of excitation in quadrupolar spins was explored. While AHT offers a simpler framework for deriving the time-propagators, the detection at stroboscopic time-intervals limits its utility in providing a comprehensive description of the spin dynamics during the excitation process. To this end, alternate methods based on Floquet theory were also explored. In particular, the exactness of time-evolution studies based on Floquet time-propagators derived from effective Floquet Hamiltonians and Floquet Magnus Expansion (FME) were examined. Although, Floquet descriptions based on effective Floquet Hamiltonians have been extensively employed

for describing the dynamics in spin-1/2 systems, the present thesis highlights the serious limitations of the effective Floquet Hamiltonian approach in the description of quadrupolar spins in rotating solids. A detailed explanation for this observations is presented in Chapter-2. By contrast, the time-propagators derived from the Floquet Magnus Expansion (FME) scheme present an attractive framework for describing the excitation process in quadrupolar spins at non-stroboscopic time-intervals. Specifically, the time-propagators based on the alternate boundary condition facilitate in the derivation of analytic expressions for describing the excitation process. Employing this approach, excitation of double-quantum transitions under MAS conditions is discussed clearly outlining the role of the sample spinning frequency and the RF amplitude employed during the excitation process. Along with the quadrupolar coupling constant, the interplay between the spinning frequency and the RF amplitude on the convergence of the perturbation corrections employed in the time-propagators is also discussed.

Based on the insights obtained from the results discussed in Chapter-2, analytic models have been proposed in Chapter-3 to describe MAS experiments involving spin I=1/2 nuclei coupled to quadrupolar spin, S=1. Specifically, implementation of experiments on spin-1/2 nuclei impeded by the interference effects due to RF fields employed on the quadrupolar spin is discussed. The interference effects introduced by the RF field on the quadrupolar spin in experiments that involve (i) measurement of CSA tensors on spin I=1/2 (ii) polarisation transfer from spin I=1/2 to S=1 is discussed through analytic expressions. Additionally, the relevance of interaction frames and the important role of Bessel functions in the optimal implementation of experiments is explicated and verified through rigorous comparisons with simulations emerging from exact numerical methods.

Although, the methodology presented in this thesis has been demonstrated to describe finite pulse effects in isolated and coupled spins involving spin-1 nucleus, we believe that the analytic framework could well be extended to study half-integral quadrupolar spins (say I=3/2, 5/2) and their effects on spin-1/2 nuclei. From an operational perspective, although, the fictitious spin-operator formalism affords a simpler description in terms of transition operators in two-level systems, the over completeness of the basis might become a concern, while dealing with higher quadrupolar spins (such as I=3/2, 5/2 etc.). In such cases, descriptions based on spherical tensor operator formalism could be handy and deserves to be explored further.